Simulation of Lime Calcination in Normal Shaft and Parallel Flow Regenerative Kilns

Dissertation

zur Erlangung des Akademischen Grades

**Doktoringenieur
(Dr.-Ing.)**

von: M.Sc. Duc Hai Do
geb. am: 15.03.1979
in: Vinh Phuc / Viet Nam

genehmigt durch die Fakultät für Verfahrens- und Systemtechnik
der Otto-von-Guericke-Universität Magdeburg

Gutachter: Prof. Dr.-Ing. Eckehard Specht
                   Prof. Dr.-Ing. Roman Weber
                   Dr.-Ing. Georg Kehse

Promotionskolloquium am: 25.04.2012

Schriftliche Erklärung

Ich erkläre hiermit, dass ich die vorliegende Arbeit ohne unzulässige Hilfe Dritter und ohne Benutzung anderer als der angegebenen Hilfsmittel angefertigt habe. Die aus fremden Quellen direkt oder indirekt übernommenen Gedanken sind als solche kenntlich gemacht.

Insbesondere habe ich nicht die Hilfe einer kommerziellen Promotionsberatung in Anspruch genommen. Dritte haben von mir weder unmittelbar noch mittelbar geldwerte Leistungen für Arbeiten erhalten, die im Zusammenhang mit dem Inhalt der vorgelegten Dissertation stehen.

Die Arbeit wurde bisher weder im Inland noch im Ausland in gleicher oder ähnlicher Form als Dissertation eingereicht und ist als Ganzes auch noch nicht veröffentlicht.

Magdeburg, den 25.04.2012

Duc Hai Do

Acknowledgements

First and foremost, i would like to express my deep and sincere gratitude to my supervisor Prof. Dr.-Ing. Eckehard Specht, for his constant advice, encouragement and financial support. His strong motivation, creativity and rich knowledge and experience enriched my confidence level to solve many complex problems in effective ways. Furthermore, his friendly personality and patience have benefited me immensely.

I am deeply grateful to Prof. Dr.-Ing . Roman Weber from the Technische Universität Clausthal for his in-depth review of my dissertation and constructive comments.

I am deeply grateful to Dr. Georg Kehse from IWP Ingenieurbüro für Wärme und Prozesstechnik GmbH, who has been also working with me since the beginning of my Ph.D time, for his friendly guidance with rich industrial experiences.

Additional thanks are also grateful sent to Dr. Ferri, Mr. Christiansen and Mr. Bresciani from Cimprogetti S.p.A, Dalmine / Italy, for their kind / friendly helps during my work.

I whole heartedly thank my colleagues Nadine, Magda, Fabian, Ping, Dr. Ashok, Dr. Woche, Dr. Al-Karawi, Gourisankar, Hassan, Hassanein, Khalid, Alfakheri, Pavan, Kotesvara Rao and of course, our friendly and warm-hearted secretary Christin Hasemann.

My deepest gratitude goes to my family, including my wife Hue Chi, our 'kleine diamond' Lora - Bao Han, my mum and all of sisters and brothers, for their unflagging love and support throughout my life; this dissertation is simply impossible without them.

Abstract

Shaft kilns are widely used for the production of lime. For the purpose of process optimization (reducing energy consumption) and regulation (producing desired lime quality), the temperature and the lime burning profiles in the kilns must be known. However, practical measurements of these parameters are very difficult due to the movements of solid bed and high temperatures in the kilns. Therefore, it is important to determine these parameters by simulations. In this dissertation, mathematical models are developed to simulate the lime burning process in shaft kilns, focusing on normal shaft kilns and parallel flow regenerative (PFR) kilns.

The mathematical models are one-dimensional and steady state, which describe the mass and energy conservations of the gas and the solid phases by a system of ordinary differential equations. A shrinking core model is employed to describe the mechanisms and to calculate the decomposition process of limestone particles.

The models are used to determine significant parameters regarding the lime burning process such as: a) the core and surface temperatures of the solid (limestone / lime) particles, b) the gas temperature, c) the lime calcination degree or the residual CO_2, d) the pressure drop along the kiln height and e) the heat loss by kiln wall.

The models are also used to investigate variables that affect the lime burning process. The following variables have been investigated in detail by the models: a) energy consumption, b) kiln throughput, c) particle size, d) limestone origin, e) excess air number, f) fuel combustion behavior and g) solid bed height.

Observations from simulation results figure out that the maximum temperatures of solid particles in the PFR kilns are significantly lower than that in the normal shaft kilns. In the PFR kilns, they vary in the range of $1000 - 1100\ ^{\circ}C$ while in the normal shaft kilns they are in the range of $1400 - 1500\ ^{\circ}C$.

In addition, to support mathematical modeling, theoretical minimum values of the specific energy consumption were determined. It has been observed that with the PFR kilns, as a result of reusing flue gas for regenerative heat transfer (saving energy), the energy consumption required for this type of kilns is significantly lower than that of the normal shaft kilns.

The simulated results were validated by experiments with measuring temperature profiles in industrial shaft kilns. The measured temperatures are close to the solid temperature predicted by the models. The simulated and measured results are in good agreement.

Keywords: Normal shaft kilns, PFR kilns, Modeling and Simulations, Measurements, Lime calcination, Temperature profile.

Zusammenfassung

Schachtöfen werden häufig für die Herstellung von Kalk verwendet. Zur Prozessoptimierung (Reduzierung des Energieverbrauchs) und zur Regulierung (Herstellung gewünschter Kalkqualität) müssen die Temperatur- und Kalkverbrennungsprofile in den Öfen bekannt sein. Allerdings sind praktische Messungen dieser Parameter sehr schwierig, aufgrund der Bewegung des Festbettes und den hohen Temperaturen in den Öfen. Daher ist es wichtig, diese Parameter durch Simulationen zu bestimmen. In dieser Dissertation wurden mathematische Modelle entwickelt, um den Kalkbrennprozess in Schachtöfen zu simulieren, insbesondere normaler Schachtöfen und Gleichstrom-Regenerativ-Schachtöfen (GGR-Öfen).

Die entwickelten mathematischen Modelle sind eindimensional, stationär und beschreiben die Massen- und Energieerhaltung der Gas- und Feststoffphase durch ein System von gewöhnlichen Differentialgleichungen. Ein Schale-Kern-Modell wurde verwendet, um die Mechanismen zu beschreiben und den Zersetzungsprozess von Kalksteinpartikeln zu berechnen.

Unter Verwendung der Modelle wurden wichtige Parameter in Bezug auf den Kalkbrennprozess in den Öfen bestimmt, wie a) die Kern- und Oberflächentemperaturen der Feststoffpartikel (Kalkstein / Kalk), b) die Gastemperatur, c) der Kalzinierungsgrad oder der Rest-CO_2 Gehalt im Kalk, d) der Druckverlust über der Ofenhöhe und e) der Wärmeverlust durch die Ofenwand.

Ebenso konnten mit Hilfe der Modelle Parameter untersucht werden, welche den Kalkbrennprozess beeinflussen. Die folgenden Parameter wurden von den Modellen näher untersucht: a) Energieverbrauch, b) Durchsatz im Ofen, c) Partikelgröße, d) Herkunft des Kalksteins, e) Luftzahl, f) Brennverhalten der Brennstoffe und g) Festbetthöhe.

Betrachtungen der simulierten Ergebnisse zeigten, dass die maximalen Temperaturen der Feststoffpartikel in den GGR-Schachtöfen bedeutend niedriger sind als in den normalen Schachtöfen. In den GGR-Schachtöfen variieren die Temperaturen in einem Bereich von 1000-1100 °C während in den normalen Schachtöfen die Temperaturen im Bereich von 1400-1500 °C liegen.

Zusätzlich wurden, zur Unterstützung der mathematischen Modellierung, theoretische Minimalwerte des spezifischen Energieverbrauchs ermittelt. Es wurde deutlich, dass aufgrund der Wiederverwendung des Rauchgases für die regenerative Wärmeübertragung (Energieeinsparung) der Energieverbrauch des GGR-Schachtofen bedeutend geringer ist als für den normalen Schachtofen.

Die simulierten Ergebnisse wurden durch experimentelle Messungen von Temperaturprofilen in industriellen Schachtöfen validiert. Die gemessenen Temperaturen entsprechen annähernd der Feststofftemperatur, welche von den Modellen prognostiziert wurde. Die simulierten und gemessenen Ergebnisse stimmen gut überein.

Schlagwörter: Normale Schachtöfen, GGR Öfen, Modellierung und Simulationen, Messungen, Kalzinierung, Temperaturprofil.

Table of contents

Nomenclatures

a	thermal diffusivity	$[m^2/s]$
A	area	$[m^2]$
b	shape factor	$[-]$
c_p	specific heat capacity	$[kJ/kg/K]$
d	particle diameter	$[m]$
D^P	pore diffusion coefficient	$[m^2/s]$
f	form factor	$[-]$
h_u	calorific heating value	$[kJ/kg]$
Δh_{CO_2}	reaction enthalpy regarding to CO_2	$[kJ/kg]$
ΔH_R	molar reaction enthalpy	$[kJ/mol]$
k	reaction coefficient	$[m/s]$
K_{CO_2}	density of CO_2 in limestone	$[kg/m^3]$
L	length	$[m]$
$\dot{m}$	mass flux	$[kg/m^2/s]$
$\dot{M}$	mass flow	$[kg/s]$
$\widetilde{M}$	molar mass	$[kg/kmol]$
O	specific surface area	$[m^2/m^3]$
P	pressure, partial pressure	$[Pa]$
$\dot{q}$	heat flux	$[W/m^2]$
$\dot{Q}$	heat flow	$[W]$
r	radial coordinate	$[m]$
R	universal gas constant, R=8.314	$[J/mol/K]$
R_i	resistances of sub-process i	$[1/s]$
t	time	$[s]$
T	temperature	$[^oC]$ or $[K]$
V	volume	$[m^3]$
w	velocity	$[m/s]$
X	conversion degree	$[-]$
y_{CO_2}	mass fraction of CO_2 in limestone	$[kg/kg]$
z	axial coordinate	$[m]$

Greek symbols

α	heat transfer coefficient	[W/m^2/K]
β	mass transfer coefficient	[m/s]
γ	air to lime ration	[m^3/kg]
δ	thickness	[m]
ε	emissivity	[-]
ζ	empirical factor to determine porosity	[-]
κ	transient factor	[-]
λ	heat conduction coefficient	[W/m/K]
μ	dynamic viscosity	[m^2/s]
ρ	density	[kg/m^3]
σ	Stefan-Boltzmann constant, $5.67 \cdot 10^{-8}$	[W/m^2/K^4]
ν	kinematic viscosity	[m^2/s]
ψ	void fraction	[-]
λ	excess air number	[-]

Subscripts

a	air
A	area
ac	lime cooling air
af	combustion air
aL	lance cooling air
aT	transport air
D	diffusion
E	energy
eff	effective
eq	equilibrium
F	front, core
F	fuel
F	furnace
fg	flue gas
G	gas
k	reaction

M	mean
max	maximum
min	minimum
mix	mixture
mono	mono-dispersion
L	length
L	stoichiometric air demand
LS	limestone
OX	oxide
pd	poly-dispersion
P	pressure
P	particle
S	solid
S	sphere
W	wall, surface

Dimensionless number

Nu	Nusselt number
Pr	Prandtl number
Re	Reynolds number
Sc	Schmidt number
Sh	Sherwood number

1 Introduction

1.1 Overview and motivation

Lime is an important raw material, which is used in many branches of industry such as flue gas desulphurization, metallurgy, construction and manufacturing of paper. Lime is produced by thermal decomposition of limestone in shaft or rotary kilns.

Lime manufacturers have been recently facing more restrictions. On the one hand, the fuel price, the main cost for lime production, has been increasing rapidly. On the other hand, the demand of reducing the emissions has become stricter. In addition, the quality of quicklime needs to be maintained. For lime manufacturers, it is very important that the following two parameters are achieved:

- Low energy consumption

- Desired (uniform) lime quality

In fact, many lime manufacturers start to reduce their costs by using cheaper fuels, optimizing the burning system and atomizing the kiln process. However, mostly this is done by the method 'learning by doing', which consumes time and money.

Burning lime or decomposition of limestone is an endothermic process, in which the kinetics of the burning process strongly depend on temperatures [1, 2]. In principle, to regulate or optimize the lime burning process, the temperature and the concentration (conversion) profiles in the kilns must be determined. However, with burning lime in shaft kilns, practical determinations of these parameters are very difficult. For example, the measurements of the kiln temperatures by using thermocouples face two main problems. Firstly, due to high temperature in the firing zone, common thermocouples (e.g., Ni-Cr/Ni) are often damaged; therefore, special thermocouples (e.g., Pt-Rh/Pt) are required. Secondly, due to the movements of solid bed with dust creation, thermocouples can also be damaged during measurements. In this case, simulations are an alternative way to model the temperature and the lime burning profiles.

Many studies have been carried out to study the lime burning in shaft kilns. In most cases, however, the studies have been mainly concentrated on global energy and mass balances of the kilns [3-9]. Significant studies focusing on the temperature and the lime calcination profiles in the kilns are relatively rare. Numerical modeling of thermal processes in mixed-feed kilns was performed by Shagapov et al. [10] and YI-Zheng-ming et al. [11]. The basic kiln temperature and calcination profiles were simulated. No investigation of influencing factors, e.g., operating conditions, was performed. Senegacnik et al. [12,13] experimentally investigated temperature profiles and developed numerical solutions to calculate lime-burning

degree in an annular shaft kiln. The influence of convective heat transfer coefficient on the lime-burning degree was studied. With CFD (computational fluid dynamics) simulations, Drenhaus et al. [14] modeled the lime burning degree and the temperatures in a pilot vertical (normal) shaft kiln with 2 m bed height. The influence of the particle size on the time of lime calcination process was investigated.

The results of the few researchers above are primary indications for basic understanding of the lime burning process in shaft kilns. However, for the purpose of process regulations and optimizations, further information needs to be explored because many parameters that affect significantly the lime burning process have not yet been investigated. Therefore, the aim of this dissertation is to develop comprehensive mathematical models to simulate the lime burning process in shaft kilns, focusing on normal shaft kilns and parallel flow regenerative (PFR) kilns. The models provide significant data required for designing and regulating shaft kilns. Furthermore, the models are also useful for a purpose of training the kiln personnel. To obtain experience within the operations is very time consuming since the kilns react to changes in operating parameters extremely slowly.

1.2 Lime production

The world production of lime grew steadily from just under 60 million tons in 1960 to peaks of 120 million tons in 1995 and 170 million tons in 2006. Even due to the recent global economic recession (2008), published estimates of the world production of quicklime (Table 1-1) suggest that the total is approximately 310 million tons in 2010.

Table 1-1 Estimations of world production of quicklime and hydrated lime, including dead-burned dolomite, 1995 – 2010, [15 - 19].

Country	2000		2006		2010	
	Mt/year	%	Mt/year	%	Mt/year	%
Brazil	5.7	4.9	6.0	3.5	7.7	2.5
China	21.5	18.5	75.0	43.5	190.0	61.3
Germany	7.6	6.6	7.0	4.1	6.8	2.2
India	-	-	4.0	2.3	14.0	4.5
Italy	3.5	3.0	5.2	3.0	2.8	0.9
Japan (quicklime only)	7.7	6.6	10.0	5.8	9.4	3.0
Mexico	6.5	5.6	4.0	2.3	5.7	1.8
Russia	8.0	6.9	8.0	4.7	7.4	2.4
United States	19.6	16.9	20.0	11.6	18.0	5.8
Other countries	35.9	30.9	32.8	19.1	48.2	15.5
Total	116.0	100	172.0	100	310.0	100

China, the United States and India are recently the top producers for lime, producing more than 200 million tons per year, or ~70 % of world output. They are followed by Brazil, Japan, Germany and Russia with about 10 % of world output.

The principal industries using lime are the desulphurization of flue gas, steel processing, constructions and manufacturing of papers. As an example, **Table 1-2** shows an estimation of using lime in EU in 2006.

Table 1-2 Estimations of using lime in EU, 2006, [20].

Industrial sectors	Contribution, %
Steeling manufacturing	30 - 40
Environmental protection (e.g, flue gas desulfurization)	30
Construction and clay soil stabilization	15 – 20
Others: chemicals, PCC for paper, food and forestry, etc.	10 - 15

The lime industry is a highly energy-intensive industry with energy cost accounting up to 50% of total production cost. The common fuels in use are solid fuel (anthracite, coal, coke, and lignite), liquid fuel (oil), gas fuel (natural gas, waste gas) and others (alternative fuel).

1.3   Lime shaft kilns

The choice of the lime kilns is a paramount importance for a lime producer. It must be suitable for burning the selected feed-stone and for producing the required quality of quicklime. It must have sufficiently low capital and operating costs to produce quicklime at a competitive price. Its capacity must also be appropriate for the market requirements. A large variety of techniques and kiln designs has been used over the centuries and around the world. The concept of the shaft kiln has been modernized in a number of designs; the typical characteristics of some common kilns are summarized in **Table 1-3**, [21 - 24].

Table 1-3 Typical characteristics of common shaft kilns

Characteristics		Normal shaft	Mixed-Feed	Annular	PFR
Output capacity, t/d		150 –300	100 - 200	200 - 600	200 - 800
Inner diameter, m		2.0 – 3.0	2.5 –5.0	3.0 – 4.5	2.5 – 3.5*
Cross-sect. area, m^2		3 –7	6 – 30	20 - 23	6 - 10*
Height of solid bed, m		10 – 15	15 – 20	15 - 25	15 – 20
Output flux, t/d/m^2		40 – 45	10 – 25	15 - 30	20 - 30*
Solid velocity, m/h		1.8 – 2.0	0.5 – 1.0	0.6 – 0.7	0.6 – 1.4
Air flux, $m^3_{STP}/m^2/s$		0.6 - 0.7	0.1 - 0.12	0.6 – 0.8	0.8 - 1.1
Min. particle size, mm		30	20	30	20
Max. particle size, mm		150	200	250	160
Total press., drop, mbar		200 – 250	10 - 30	200 - 400	300 - 400
Mean kind of fuel		natural/lean gas lignite	anthracite coke	natural/lean gas coal/oil	natural/lean gas lignite/pet coke
Energy supply	MJ/kg_{lime}	3.8 - 4.8	3.9 - 4.5	3.8 - 4.1	3.3 - 4.0
	kcal/kg_{lime}	910 – 1150	930 - 1080	910 - 980	790 - 950
Max. solid temp., °C		1400 – 1500	1100 - 1300	1100 - 1200	1100 - 1200
Max. gas temp., °C		1500 – 1600	1300 - 1400	1200 - 1300	1200 - 1300
Lime	type	hard-burnt	hard/middle	middle/soft	soft-burnt
	reactivity	low	low/medium	medium/high	high

* Data given for one shaft

Some designs are more suitable for low outputs (below 100 t/d), while others can be used for much higher outputs (up to 800 t/d). Normal acceptable size for the feed-stone ranges from a minimum of 20 mm to a top size of up to 200 mm and even up to 250 mm. Some kilns are suitable for operation on gaseous, liquid and solid fuels, while the options for others are more restricted. Nowadays, many lime producers operate two or more types of kilns, using different sizes of stone feed, and producing different qualities of lime.

In practice, it typically takes about 1.75 kg of limestone to produce 1 kg of lime, the transportation of the raw material should be kept to a minimum. Therefore, lime kilns are normally located close to the limestone quarry.

1.4   Normal shaft kilns

Figure 1-1 and **Figure 1-2** illustrates the schemes of normal shaft kilns. These types of kilns are also named as RCE-kilns. In principle, the normal shaft kiln is a vertical single shaft where limestone is charged at the top of the kiln and quicklime is discharged at the bottom. The solid moves slowly downwards through the kiln by gravity. Heat to calcine the limestone is generated by fuel combustion where fuel is introduced with air in the middle of the kiln. Therefore, the solid above is preheated by hot exhaust gas in counter-current flow and the solid below is cooled by the cooling air introduced at the kiln bottom. In this way, material entering the kiln at the top is first preheated, then calcined and finally cooled during its passage through kiln. The gas leaving at the top of the kiln contains combustion gas and CO_2 dissociated from the limestone. The kiln is theoretically divided into three operating zones.

- Preheating zone: The upper part of the kiln where limestone is heated by hot exhaust gas to its calcination temperature of about 810 - 840°C.

- Burning zone: The middle part of the kiln in which the limestone is decomposed into quicklime and CO_2, fuel is burnt in preheated air.

- Cooling zone: The lower part of the kiln where lime emerging from burning zone is cooled by air before discharge.

1.5   PFR shaft kilns

The PFR kiln is a modern kiln with two-shafts (or three-shafts) defined by alternating burning and non-burning shaft operation. **Figure 1-3** and **Figure 1-4** show characteristic feature of a PFR kiln, which consists of two interconnected vertical shafts of either rectangular or circular cross sectional shape. Each shaft is subjected to two distinct modes of operation, burning and

non-burning mode. While one shaft operates in the burning mode (supplied by fuel and combustion air), the other shaft operates in the non-burning mode.

In burning mode, one shaft is characterized by the parallel flow of combustion air/gases and stone, whereas, in non-burning mode the other shaft is characterized by the counter-current flow of off-gases and stone. Combustion air is introduced under pressure at the top of the preheating zone above the stone bed. The complete kiln system is pressurized. The combustion air is preheated by the stone prior to mixing with the fuel. The combustion gases exit the burning shaft through a crossover-channel into the non-burning shaft. The off-gases transfer heat to the stone during the non-burning mode and then the stone reclaims the heat to the combustion air during the burning mode.

The above method of operation incorporates two key concepts:

- The stone-packed in the preheating zone in each shaft acts as a regenerative heat exchanger. The surplus heat in the gases is transferred to the stone in the non-burning mode. It is then transferred from the stone to the combustion air in the burning mode. Because of this alternative heat transfer, PFR kilns have the lowest specific energy consumption compared with other types of kilns.

- In parallel flow of PFR kilns, the fuel is introduced at the upper end of the burning zone and the combustion gases travel parallel to the material. As a result, the heat released from fuel combustion is mostly absorbed by the solid for calcination of limestone so that the temperature in the burning zone is typically 900 – 1200 °C on average. Because of parallel flow heating, PFR kilns are suitable for the production of soft-burnt, highly reactive lime.

Depending on the kiln manufacturers, different concepts of optimizing the kiln process have been developed to design the PFR kilns. For example, the shapes of the cross-section can be round / circular, rectangular or special design with D-shape (Cimpprogetti kilns, Figure 1-4); the cross-over channel can be direct (for rectangular kilns) or indirect / circular (for circular kilns). Some different designs of the kilns can be seen from **Figure 1-5** to **Figure 1-6**.
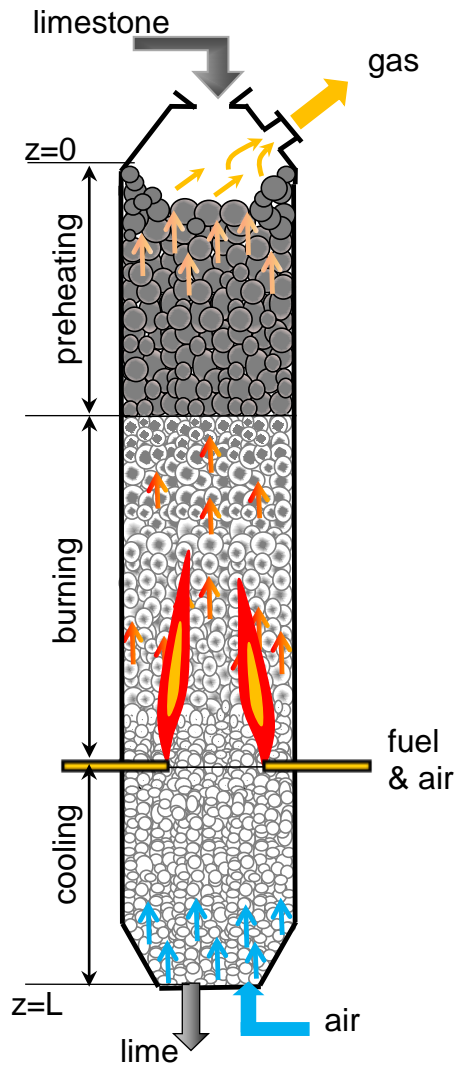
Figure 1-1: Schematic diagram of normal shaft kilns

Figure 1-2: Normal shaft kiln (source: http://www.rhi.at)
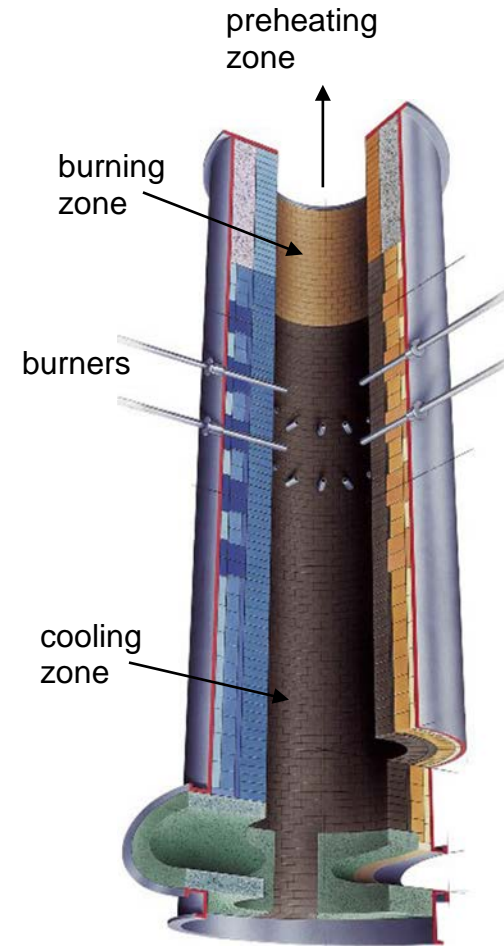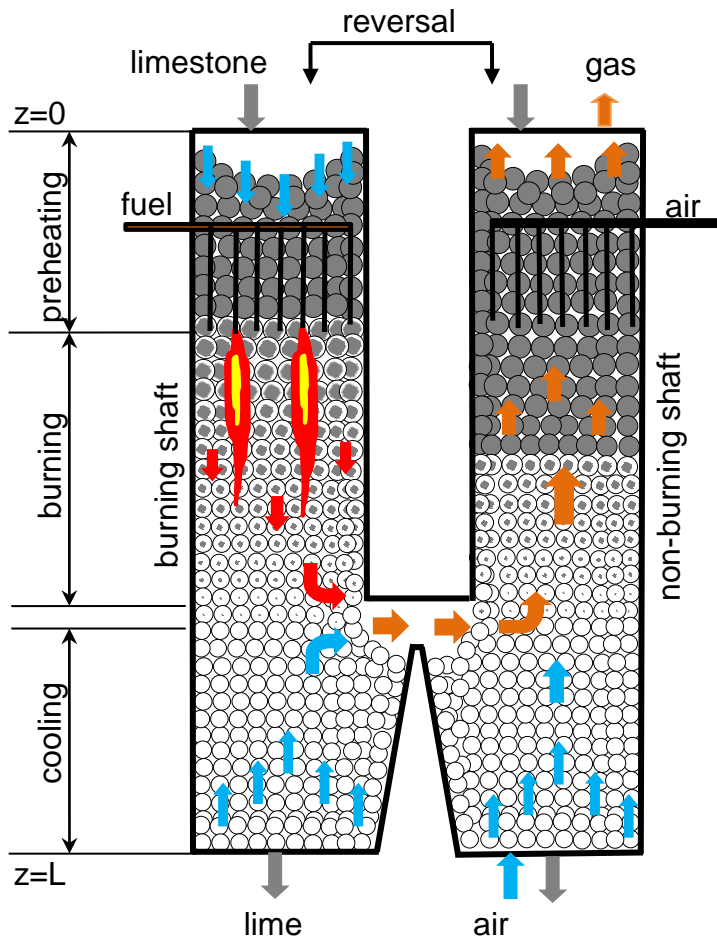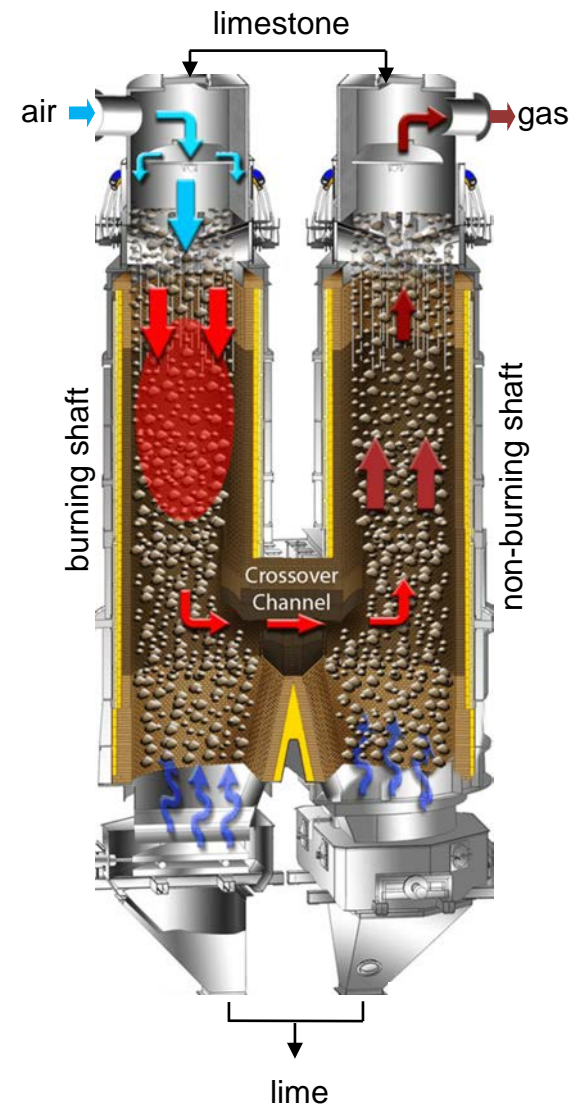
Figure 1-3: Schematic diagram of a PFR shaft kiln

Figure 1-4: PFR shaft kiln (source: http:// www.cimprogetti.com)

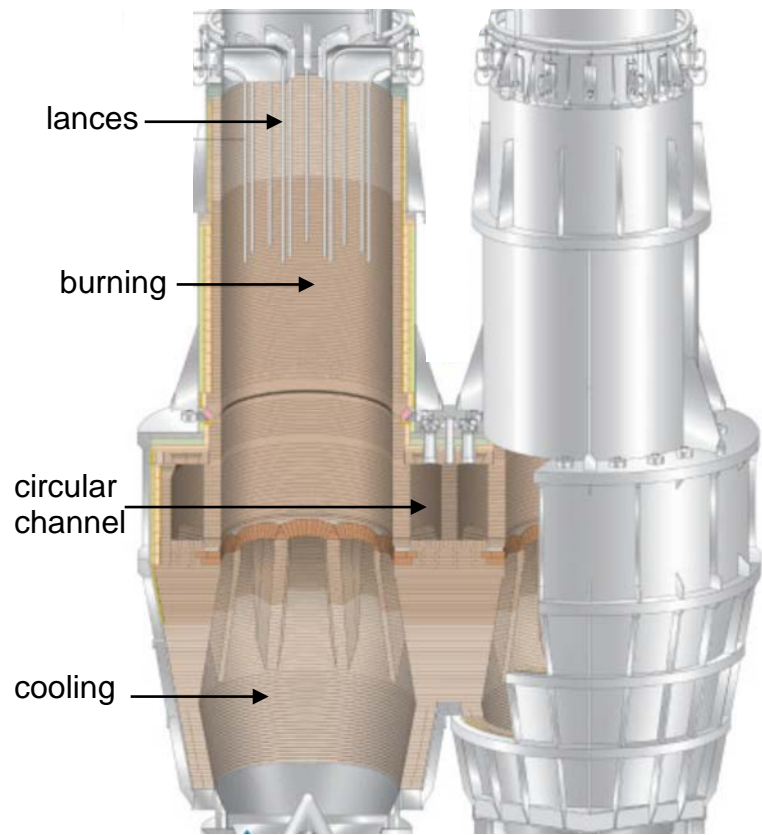Figure 1-5: Circular PFR kiln (source: http:// www.maerz.com)
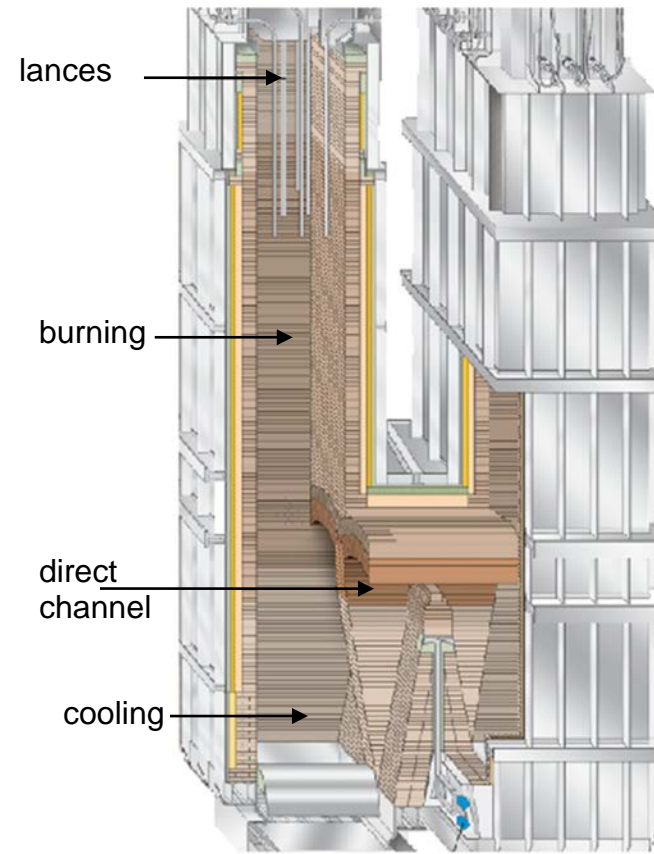

Figure 1-6: Rectangular PFR kiln (source: http:// www.maerz.com)

Figure 1-7: PFR- kiln (source: http:// www.maerz.com)

Figure 1-8: PFR- kiln (source: http:// www.cimprogetti.com)

2 General description of sub-processes

2.1 Determination of heat transfer coefficient

2.1.1 Convective heat transfer coefficient

The heat transfer in a shaft kiln (packed bed) is dominated by convection. One approach to estimate convective heat transfer coefficient (α) in a packed bed is given by Jeschar et al. [25, 26] in which a packed bed can be described as a bundle of parallel pipes. The Nusselt correlation in the packed bed is given as:

$$Nu_{bed} = 2 + 1.12 \cdot Re^{1/2} \cdot Pr^{1/3} \cdot \left(\frac{1 - \psi}{\psi} \right)^{1/2} + 0.005 \cdot Re \qquad (2\text{-}1)$$

where ψ is the void fraction of the packed bed.

The Nusselt number is defined as:

$$Nu_{bed} = \frac{\alpha \cdot d}{\lambda_g} \qquad (2\text{-}2)$$

where d is the size of the particle and λ_g is the gas thermal conductivity.

The Reynolds number is given by:

$$Re = \frac{w \cdot d}{\nu \cdot \psi} \qquad (2\text{-}3)$$

where ν is gas kinematic viscosity and w is the empty tube velocity that is called as superficial velocity, if no packing were present in the bed. This velocity is determined by:

$$w = w_{STP} \cdot \frac{\rho_{STP}}{\rho} \qquad (2\text{-}4)$$

where w_{STP} is the velocity at STP (standard temperature and pressure) condition, ρ and ρ_{STP} are the density at temperature T and at STP. The velocity w_{STP} is given as:

$$w_{STP} = \frac{\dot{V}_{STP}}{A_F} \qquad (2\text{-}5)$$

here $\dot{V}_{STP}$ is the gas volume flow at STP and A_F is the cross-section area of the kiln.

11

The Prandtl number is defined as:

$$Pr = \frac{\nu \cdot \rho \cdot c_p}{\lambda_g}$$

(2-6)

here c_p is the specific heat capacity of the gas.

There is another model so called single-particle model, which is also commonly used to determine the heat transfer coefficient in a packed bed. Bes [27] has compared the convective heat transfer coefficients obtained from the two approaches. The results from the model based on single particle are slightly lower than those from the hydraulic diameter model. For the typical air velocity of about 1 m/s at standard temperature and pressure, the difference between the results of both approaches is less than 20%.

2.1.2   Overall heat transfer coefficient

The solid particle has a temperature distribution in a radial direction since the heating-up and the cooling-down of solid particles is a transient process. To calculate the temperature profile inside the particle, the Fourier differential equation must be solved and this requires a lot of effort. In the industrial practice, however, an assumed homogeneous average temperature (calorific temperature) is often more preferred, to make the energy balance easier. For this purpose, Jeschar et al. **[26]** & Mills [28] introduced a modified overall heat transfer coefficient, α_κ.

$$\alpha_\kappa = \frac{1}{\dfrac{1}{\alpha} + \dfrac{d/2}{\kappa \cdot \lambda}}$$

(2-7)

where λ is the thermal conductivity of the solid particle, and κ is the transient factor given as:

$$\kappa = \begin{cases} 3 \text{ for a plate} \\ 4 \text{ for a cylinder} \\ 5 \text{ for a sphere} \end{cases}$$

(2-8)

2.2   Determination of mass transfer coefficient

In simulation of limestone decomposition, the convective mass transfer of the produced CO_2 into the gaseous ambience must be calculated. With analogy to heat transfer, the mass transfer

coefficient of CO_2 from the limestone surface to the gas, β, can be calculated from the Sherwood function.

$$Sh = 2 + 1.12 \cdot Re^{1/2} \cdot Sc^{1/3} \cdot \left(\frac{1-\psi}{\psi}\right)^{1/2} + 0.005 \cdot Re \qquad (2\text{-}9)$$

The Sherwood function is defined as:

$$Sh = \frac{\beta \cdot d}{D_{CO2-Air}} \qquad (2\text{-}10)$$

where $D_{CO2\text{-}Air}$ is the binary diffusivity of CO_2 in air, which will be determined in the next.

The Schmidt number Sc is defined as:

$$Sc = \frac{\nu}{D_{CO2-Air}} \qquad (2\text{-}11)$$

2.3 Gas mixture properties

To calculate the Nusselt and the Reynolds numbers the material property values have to be calculated at the gas temperature T because the temperature difference is significant. The material property values are calculated with the following equations given by Specht [29]:

$$\lambda = \lambda_o \cdot \left(\frac{T}{T_o}\right)^{n_\lambda} \qquad (2\text{-}12)$$

$$\mu = \mu_o \cdot \left(\frac{T}{T_o}\right)^{n_\mu} \qquad (2\text{-}13)$$

$$a = a_o \cdot \left(\frac{T}{T_o}\right)^{n_\mu + 1 - n_c} \qquad (2\text{-}14)$$

$$\rho = \rho_o \cdot \left(\frac{T}{T_o}\right)^{-1} \qquad (2\text{-}15)$$

13

$$c_p = c_{po} \cdot \left(\frac{T}{T_o}\right)^{n_c} \tag{2-16}$$

$$\nu = \nu_o \cdot \left(\frac{T}{T_o}\right)^{n_\mu + 1} \tag{2-17}$$

$$D = D_o \cdot \left(\frac{T}{T_o}\right)^{n_D + 1} \tag{2-18}$$

From Eq.(2-18), the diffusivity of the CO_2 in air, $D_{CO2\text{-}Air}$ given before in Eqs.(2-10)-(2-11), can be approximated with $D_o = 0.14 \cdot 10^{-4} \, m^2/s$ and $n_D = 1.71$.

In the above equations, T_o is the reference temperature taken as 273 K. The material properties of gas components at the temperature T_o are gathered in **Table 2-1**.

Table 2-1 Material properties of gases at $T_o = 273$ K

Gas	$\widetilde{M}$	ρ_o	c_{po}	n_c	λ_o	n_λ	μ_o	n_μ	Pr
unit	kg/kmol	kg/m^3	J/kg/K	-	W/m/K	-	mg/m/s	-	-
N_2	28	1.26	1000	0.11	0.024	0.76	16.8	0.67	0.70
CO	28	1.26	1000	0.12	0.024	0.78	16.8	0.67	0.70
Air	29	1.29	1000	0.10	0.025	0.76	17.4	0.67	0.70
O_2	32	1.44	900	0.15	0.025	0.80	19.7	0.67	0.70
CO_2	44	1.98	840	0.30	0.017	1.04	14.4	0.77	0.73
H_2O	18	0.81	1750	0.20	0.016	1.42	8.7	1.13	0.95

The properties of gas mixtures can be calculated with the following formulas:

$$\rho_M = \sum \rho_i \cdot \tilde{x}_i \tag{2-19}$$

$$\lambda_M \approx \sum \lambda_i \cdot \tilde{x}_i \tag{2-20}$$

$$c_{pM} = \sum c_{pi} \cdot x_i = \frac{1}{\rho_M} \sum c_{pi} \cdot \tilde{x}_i \cdot \rho_i \tag{2-21}$$

where $\tilde{x}_i$ is the molar or volume fraction of component i in a gas mixture and x_i the mass fraction of component i in a gas mixture.

14

2.4 Flow pattern in packed bed

2.4.1 Void fraction

Shaft kilns are basically packed bed reactors. The void fraction has significant effect on the heat and mass transfer. The void fraction Ψ of a packed bed is defined as:

$$\Psi = \frac{\text{Bed volume} - \text{Packing volume}}{\text{Bed volume}}$$

(2-22)

The void fraction can be influenced by the method of packing (random or regular, loose or dense), particle shape (sphere, cylinder, etc), and particle size distribution.

For infinitely extended, regular packing of equally sized, large spheres the void fraction is:

> 0.476   for simple cubic packing
> 0.395   for cubic space centered packing
> 0.259   for cubic face centered packing.

For random packing of equally sized, large spheres the void fraction is:

> 0.4 - 0.42   for loose packing
> 0.36 - 0.38   for dense packing.

Figure 2-1 shows a particle size distribution in a packed bed as an example. The void fraction does not depend on the average particle size, but much on the width of the particle size distribution, which is characterized by the ratio between the maximum (coarse, d_c) and minimum (fines, d_f) size, Furnas [30]. **Figure 2-2** shows the influences of the ratio d_c/d_f and the volume fraction (Q_f) of fine particles on the void fraction. When the ratio $d_c/d_f =1$ (mono-dispersion), the void fraction has the maximum value (Ψ_{mono}) of about 0.4. The void fraction decreases rapidly with the increases of the ratio d_c/d_f, especially with d_c/d_f greater than 3. The theoretical minimum value of the void fraction is about 0.16. In addition, at the same ratio d_c/d_f, the void fraction decreases with increasing the Q_f from 0 to about 30 %, but it increases while Q_f is greater than 30 %. There are two limiting cases in which the void fraction depends on the Ψ_{mono} and the Q_f as given in the figure. The more closely or sharply the particle size distributes, the lower is the void fraction.

An empirical equation to determine the actual void fraction of a packed bed with a random packing of particles with different sizes, is introduced by Tsotsas [31]:

$$\Psi_{pd} = \Psi_{mono}\left[1 - 0.259\zeta + 0.017\zeta^2 - 0.112\zeta^3\right] \qquad (2\text{-}23)$$

where Ψ_{pd} stands for the void fraction of poly-dispersion packing of a packed bed and ζ is a corresponding factor defined as:

$$\zeta = \left[\frac{\sum V_i / d_i^2}{\left(\sum V_i / d_i\right)^2} - 1\right] \qquad (2\text{-}24)$$

where V_i and d_i are the volume fraction and the size of fraction i.
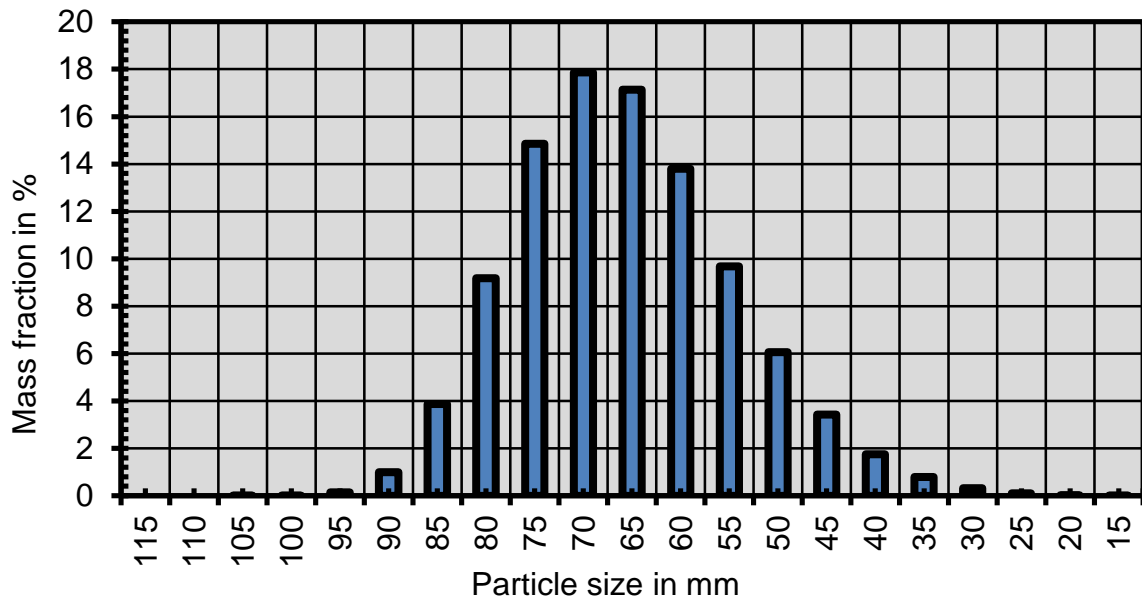
Figure 2-1: An example of particle size distribution of limestones
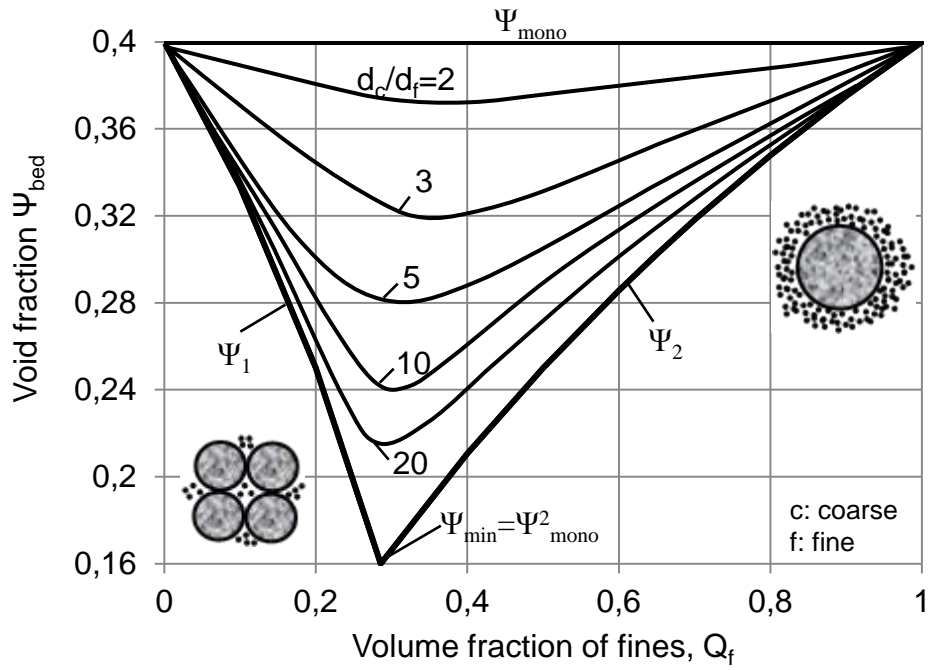
Figure 2-2: Bed porosity of bi-dispersed packing of spheres, Furnas [30]

Two limiting cases:

$$\Psi_1 = \Psi_{mono} \cdot \left[1 - \frac{(1 - \Psi_{mono})}{\Psi_{mono}} \cdot \frac{Q_f}{1 - Q_f} \right] \qquad \text{and} \qquad \Psi_2 = \Psi_{mono} \cdot \left[\frac{Q_f}{1 - \Psi_{mono} + \Psi_{mono} \cdot Q_f} \right]$$
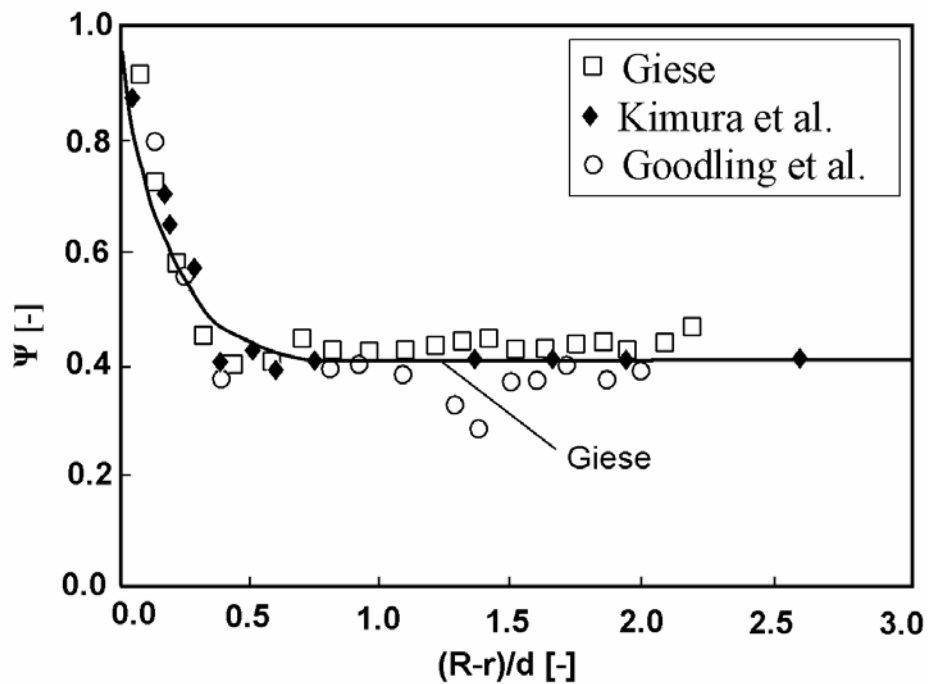
Figure 2-3: Radial porosity profile in tubes packed with imperfect spheres

The void fraction mentioned above is an average void fraction of the entire packed bed. However, in a radial direction of the packed bed, especially in the region near the wall, the void fraction is much higher than the others Giese [32]. This is due to the wall effect as shown in **Figure 2-3**.

2.4.2 Pressure drop

The pressure drop in the packed bed can be described by two different models: a) a hydraulic diameter model and b) a one particle cross-flow model, Bes [27]. In this study, the hydraulic diameter model is used to calculate the pressure drop. In this model, the flow through a packed bed can be regarded as fluid flow past some number of submerged objects, in which the hydraulic diameter is defined as:

$$d_H = \frac{V_H}{A_H} = \frac{\psi}{O}$$

(2-25)

where V_H is the volume that is available for flow in the packed bed, A_H is the wetted surface in the packed bed and O is the specific surface are of the packed bed, which are determined from the specific surface (A_P) and the volume (V_P) of a single particle in the bed:

$$O = \frac{V_P}{A_P} \cdot (1 - \psi)$$

(2-26)

The specific surface area O can be calculated if the geometry of the particles and the void fraction in the bed are known. For examples, with spheres, the value of O is obtained as:

$$O = \frac{6}{d} \cdot (1 - \psi)$$

(2-27)

There are two existing equations given Ergun [33] and Brauer [34] to determine the pressure drop of a packed bed. As an example, the Ergun equation is used in this dissertation to determine the pressure drop. This equation is based on the model conception that the real packed bed can be replaced by a parallel connection of flow channels, and the pressure drop calculation is similar to the one phase pipe flow, however with the hydraulic diameter of the packed bed as characteristic dimension. The Ergun equation is described as follows:

$$\Delta P = \int_{z=0}^{L} 150 \cdot \frac{(1-\Psi)^2}{\Psi^3} \cdot \frac{\rho \cdot \nu \cdot w}{\bar{d}^2} dz + \int_{z=0}^{L} 1.75 \cdot \frac{(1-\Psi)}{\Psi^3} \cdot \frac{\rho \cdot w^2}{\bar{d}} dz$$

(2-28)

where $\bar{d}$ is the Sauter mean diameter and w is the superficial velocity defined as before.

18

The first term of the Ergun equation describes the change of pressure under viscous flow, while the second term accounts for change of pressure at turbulent flow (kinematic energy loss). The second term is dominant in this equation. It can be seen from this equation that the pressure drop along the length of the packed bed depends on the packing size, the bed void fraction, the gas velocity, density and viscosity.

The Sauter mean diameter is described as:

$$\overline{d} = \left[\sum_{i=1}^{n} \left(\frac{V_i}{V} \cdot \frac{1}{d_i} \right) \right]^{-1} \qquad (2\text{-}29)$$

where V is total mass or volume of all solid particles and V_i is mass or volume of solid particle class i.

In the Eq. (2-28), the void fraction and the particle size are constant values, however the gas properties (viscosity, density and velocity) are functions of gas temperature. Therefore, to determine the pressure drop the gas temperature must be calculated. The method of calculating the gas temperature will be mentioned in one of the following chapters, which described process modeling and simulation.

3   Decomposition of limestone

3.1   Limestone characterization

The main component of limestone is calcium carbonate ($CaCO_3$), which is formed by the compaction of the remains of coral animals and plants on the bottoms of oceans. It can be a soft white substance (chalk) through to a very hard substance (marble). Most commercial limestone deposits are a brownish rock. As an example, the chemical composition and bulk density of some limestone are shown in **Table 3-1**, Cheng [35].

Table 3-1 Chemical composition and bulk density of some typical limestone

Chemical composition, (%)	Cretaceous limestone	Jurassic limestone	Devonian limestone	Marble
CaO	52.47	55.70	54.29	55.34
MgO	0.30	0.190	0.39	0.59
SiO_2	4.68	0.240	1.83	0.08
Fe_2O_3	0.24	0.032	0.21	0.05
Al_2O_3	0.63	0.043	0.08	0.01
K_2O	0.08	0.007	0.02	0.004
Na_2O	0.03	0.013	0.01	0.01
BaO	0.01	0.012	0.02	0.01
SrO	0.03	0.004	0.02	0.01
Mn_XO_Y	0.03	0.013	0.02	0.004
SO_3	0.05	-	0	-
Weight loss (CO_2), %	41.50	43.51	43.05	43.97
Density, (kg/m^{-3})	2510	2610	2680	2710

3.2   Lime quality

3.2.1   Lime reactivity

The burning grade of lime can be characterized by its reactivity. The lower the decomposition temperature is held during the decomposition of limestone, the higher will be the lime reactivity. In the practice, the lime reactivity is detected by the velocity of temperature increase of the water-lime-slurry, after the 150 g lime powder of grain size of 0-3 mm was dosed into 600 ml distilled water of 20°C. From the slaking-curve, which indicates the temperature increase of the slurry due to the hydration reaction of lime, a parameter t_{60} can be read out, which means after this time the slurry temperature will increase from 20 up to 60°C

(DIN EN 459-2 2002). When t_{60} is shorter than 2 min, then the lime is said to be soft-burnt. When t_{60} is in the range 2 min to 6 min, the lime is said as medium-burnt and the lime is hard-burnt when t_{60} is longer than 6 min. As an example, **Figure 3-1** shows the results of measuring t_{60} of three different limes, Schwertmann [36]. In this figure, it can be seen that the t_{60} of a soft-burnt lime sample is about 1.8 min, t_{60} of a medium-burnt sample is 4 min and that of a hard-burnt lime is approximately 7 min.
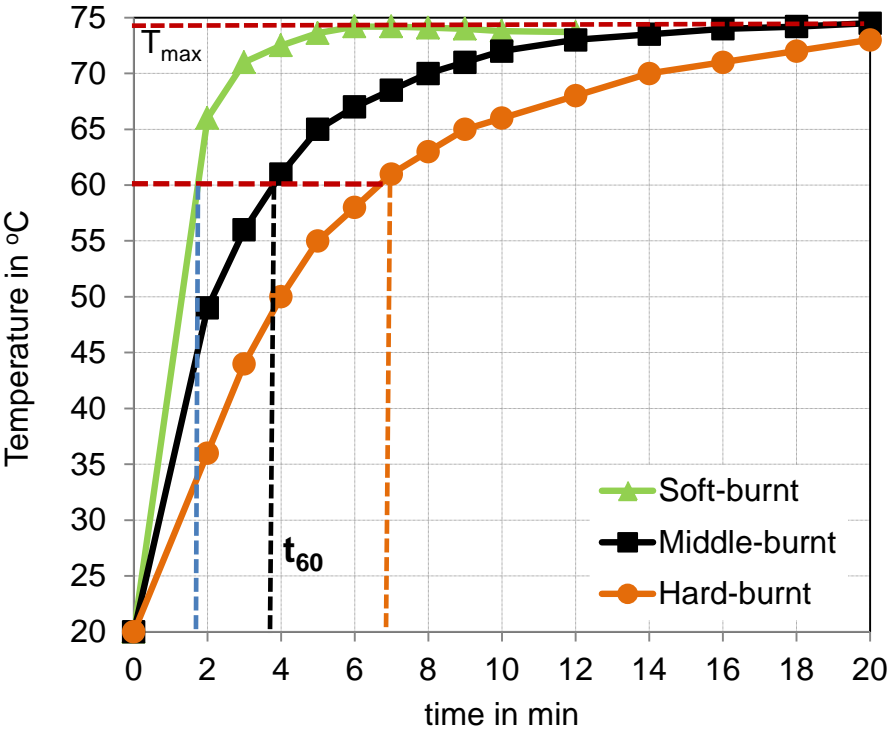

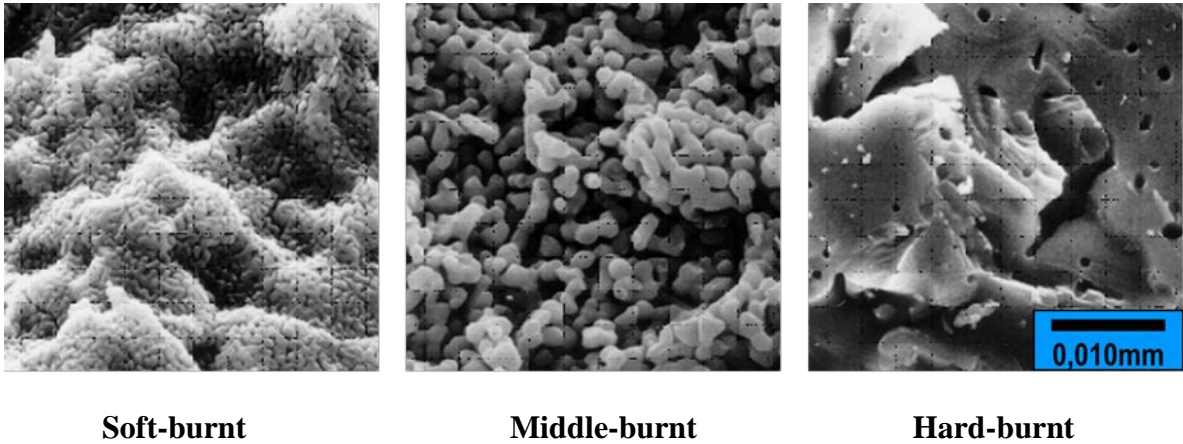Figure 3-1: Measurement of lime reactivity, Schwertmann [36]

Soft-burnt   **Middle-burnt**   **Hard-burnt**

Figure 3-2: SEM pictures of lime, Schwertmann [36]

The t_{60}-value is correlated with the specific surface area of the lime (for example BET-surface area), or the porosity of the lime. The higher the temperature at the end of the burning process, the smaller will be the specific surface and the porosity; hence the t_{60}-value will be longer. This is decided by the development of the crystal structure or the sintering effect in the lime. Under Scanning Electronic Microscope (SEM), limes of different reactivity have different crystal structure and pores system, which is shown in **Figure 3-2**.

3.2.2 Residual CO_2 in lime

Another measurement of the lime quality is the residual CO_2 (Res.CO_2) in the lime. This refers to the content in percentage of the mass of the un-reacted CO_2 to the mass of the lime.

$$\text{Res.CO}_2 = \frac{\dot{M}_{CO2} - \dot{M}_{CO2(R)}}{\dot{M}_{LS} - \dot{M}_{CO2(R)}} \tag{3-1}$$

where $\dot{M}_{CO2}$ is the total mass flow of CO_2 in limestone, $\dot{M}_{CO2(R)}$ is the total mass flow of CO_2 decomposed and $\dot{M}_{LS}$ is the mass flow of limestone, which is related to $\dot{M}_{CO2}$ as:

$$\dot{M}_{LS} = \frac{1}{y_{CO2}} \cdot \dot{M}_{CO2} \tag{3-2}$$

where y_{CO2} is the mass fraction of CO_2 in the limestone, which varies for different limestones, for example, with pure calcium carbonate $y_{CO_2} = 0.44$ kg$_{CO2}$/kg$_{LS}$.

The conversion degree X is defined as the ratio of the total mass of reacted CO_2 to the mass of CO_2 content in the limestone

$$X = \frac{\dot{M}_{CO2(R)}}{\dot{M}_{CO2}} \tag{3-3}$$

From above equations the relation between the conversion degree and the residual CO_2 content is obtained as:

$$X = \frac{y_{CO_2} - \text{Res.CO}_2}{(1 - \text{Res.CO}_2) \cdot y_{CO_2}} \tag{3-4}$$

and

$$\text{Res.CO}_2 = \frac{1}{\dfrac{1}{y_{CO_2}} - X} - \frac{1}{\dfrac{1}{y_{CO_2} \cdot X} - 1} \tag{3-5}$$

3.3 Limestone decomposition model

The decomposition of limestone is an endothermic topochemical reaction described as follows, Oates [1]:

$$CaCO_3 \quad + \quad \Delta H_R \quad = \quad CaO \quad + \quad CO_2 \tag{3-6}$$

(solid)   (reaction enthalpy) (solid)   (gaseous)
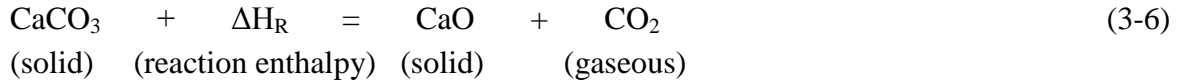
The calcination process can be explained by using a partially decomposed piece of carbonate, whose profiles of CO_2 partial pressure and temperature are shown in **Figure 3-3**. The specimen comprises a dense carbonate core surrounded by a porous oxide layer. In the calcination reactor at temperature T_g heat is transferred by radiation and convection (symbolized by α) to the solid surface at a temperature of T_{sw}. By means of thermal conduction (λ) heat penetrates through the porous oxide layer to reach the reaction front, where the temperature is T_{sf}. As the reaction enthalpy is many times greater than the internal energy, the heat flowing further into the core is negligible during reaction. Therefore, the core temperature is only slightly lower than the front temperature. Once heat is supplied, the chemical reaction (k) then takes place, for which the driving force is the deviation of CO_2 partial pressure from the equilibrium (P_{eq}- P_f). The released CO_2 diffuses (D^P) through the porous oxide layer to the surface and finally passes by convection (β) to the surroundings where the CO_2 partial pressure P_g exists. The four physical transport processes and the chemical kinetics involved are therefore interconnected.
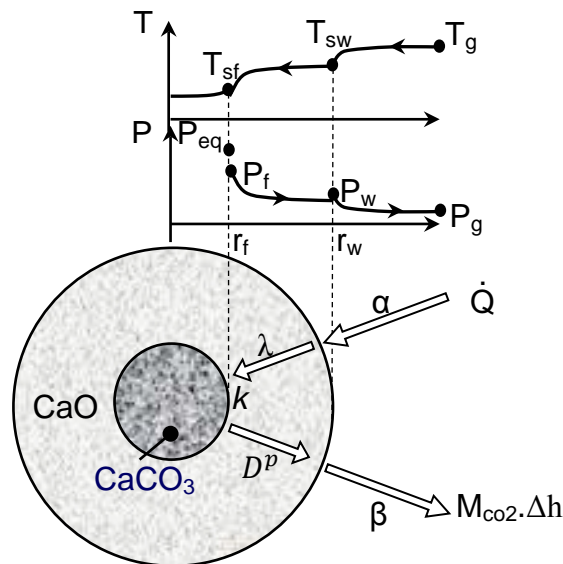
Figure 3-3: Decomposition model of limestone particle

To calculate the decomposition of a single limestone particle, a one-dimensional shrinking core model was established by Szekely et al. [37] and Kainer et al. [38], which is based on the assumptions of an ideal sample geometry (sphere, cylinder or plate), a pseudo steady state condition and constant material properties. A system of heat and mass balance equations, which are used to calculate the decomposition of limestone, are given as follows:

The heat balance equation (e.g., for spheres) is obtained by heat conduction from the particle surface through the lime layer to the reaction front.

$$\dot{Q} = 4\pi r_w r_f \cdot \frac{\lambda}{(r_w - r_f)} \cdot \left(T_{sw} - T_{sf} \right) \tag{3-7}$$

The mass balance equation of CO_2 is obtained by combining the mass transfer at the particle surface and the diffusion in the lime layer:

$$\dot{M}_{CO_2} = 4\pi r_w r_f \cdot \frac{D^P}{\left(\dfrac{r_w - r_f}{D^P} + \dfrac{1}{\beta} \right)} \cdot \frac{1}{R_{CO2}} \cdot \left(\frac{P_f}{T_{sf}} - \frac{P_g}{T_{sw}} \right) \tag{3-8}$$

For the reaction at the front, the reaction rate is proportional to the deviation of partial pressure from equilibrium.

$$\dot{M}_{CO_2} = 4\pi r_f^2 \cdot \frac{k}{R_{CO2} \cdot T_{sf}} \cdot \left(P_{eq} - P_f \right) \tag{3-9}$$

where the equilibrium pressure is defined as:

$$P_{eq} = P_o \cdot \exp\left(-\frac{\Delta H_R}{RT_{sf}} \right) \tag{3-10}$$

with P_o is 2.15×10^7 bar and ΔH_R is 168 kJ mol^{-1}, Silva et al. [39].

The heat flow and the mass flow of the CO_2 are finally related by:

$$\dot{Q} = \Delta h_{CO_2} \cdot \dot{M}_{CO_2} \tag{3-11}$$

where Δh_{CO_2} is the specific reaction enthalpy corresponding to the produced CO_2 in mass, 3820 kJ/kg.

From above equations, the decomposition parameters such as mass flows of CO_2 decomposed ($\dot{M}_{CO_2}$), moving reaction front (r_f) and reaction temperature (T_{sf}), can be calculated.

The mass flow of CO_2 can be expressed as:

$$\dot{M}_{CO_2} = -4\pi r_f^2 \cdot K_{CO_2} \cdot \frac{dr_f}{dt} \tag{3-12}$$

where K_{CO_2} is the density of CO_2 in the limestone, e.g. 1190 kg_{CO_2}/m^3 for a pure limestone with a density of about 2700 kg/m^3.

It is more convenient to introduce the conversion degree X for calculations. The conversion degree X is given before in Eq.(3-3). It can be defined in another way related to the moving front with time dependency as:

$$X = \frac{\dot{M}_{CO2(t=0)} - \dot{M}_{CO2(t)}}{\dot{M}_{CO2(t=0)}} = 1 - \left(\frac{r_f}{r_w}\right)^b \tag{3-13}$$

where b is the shape factor, b=1, 2 or 3 for a plate, cylinder or sphere, respectively.

From Eq. (3-7) to Eq.(3-13), a couple of differential equations were derived to calculate the conversion degree X and the decomposition temperature T_{sf}, Kainer et al. [38].

$$\frac{dX}{dt} \cdot [R_\lambda \cdot f_1(X)] = 1 \tag{3-14}$$

$$\frac{dX}{dt} \cdot [R_\beta + R_D \cdot f_1(X) + R_k \cdot f_2(X)] = 1 \tag{3-15}$$

where $f_1(X)$ and $f_2(X)$ are the form functions, for example with spheres, these functions are described as:

$$f_1(X) = 2 \cdot \left[(1-X)^{-\frac{1}{3}} - 1\right] \tag{3-16}$$

$$f_2(X) = \frac{1}{3} \cdot (1-X)^{-\frac{2}{3}} \tag{3-17}$$

The resistances R_i, where T_{sf} is included, are given in the following equations.

25

$$R_\lambda = \frac{K_{CO_2} \cdot \Delta h_{CO_2}}{T_{sw} - T_{sf}} \cdot \frac{r_w^2}{2 \cdot \lambda \cdot b} \tag{3-18}$$

$$R_k = \frac{K_{CO_2} \cdot R_{CO_2} \cdot T_{sf}}{P_{eq} - P_g} \cdot \frac{r_w}{k} \tag{3-19}$$

$$R_D = \frac{K_{CO_2} \cdot R_{CO_2} \cdot T_{sf}}{P_{eq} - P_g} \cdot \frac{r_w^2}{2 \cdot D^P \cdot b} \tag{3-20}$$

$$R_\beta = \frac{K_{CO_2} \cdot R_{CO_2} \cdot T_{sf}}{P_{eq} - P_g} \cdot \frac{r_w}{\beta \cdot b} \tag{3-21}$$

3.4 Determination of material properties

The material properties of limestones such as the thermal conductivity, the reaction coefficient and the pore diffusivity are important input parameters for modeling the lime burning process. Therefore, in this study, experiments were carried out to determine these parameters. The experimental apparatus is shown schematically in **Figure 3-4**. According to Kainer et al. [38], the material properties can be evaluated by an analytical solution. The evaluation requires particles of cylindrical or spherical shape. Hence, cylinders were prepared from large stone pieces using hollow drillers.

In Figure 3-4, the limestone specimens were suspended from a balance with which the weight loss and therefore the conversion degree could be recorded continuously. In order to have well-defined flow conditions around the specimen, pure air was introduced from the bottom of the furnace with a known volume flow. A small hole was drilled in the center of the specimen. The temperature in the hole was measured simultaneously with the weight loss by a thermocouple. The knowledge of this core temperature is essential to analyze the material properties of limestone.

The tests were performed using cylinders with diameters in the range of 20 – 25 mm, **Figure 3-5**. The length / diameter ratios of cylinders ranged from 4 to 10 and the cylinders were insulated at the top and bottom so that they could be regarded as infinitely long and treated as one-dimensional.
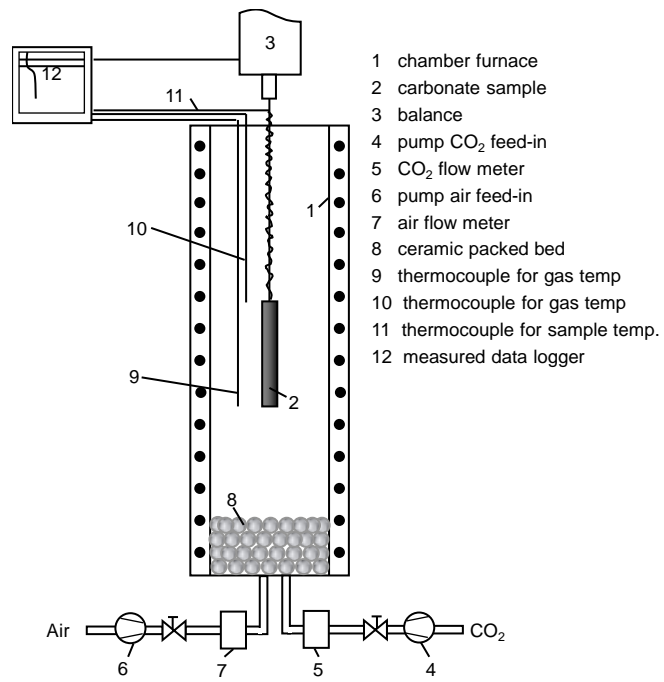
Figure 3-4: Experimental apparatus for measuring limestone decomposition

1 chamber furnace
2 carbonate sample
3 balance
4 pump CO_2 feed-in
5 CO_2 flow meter
6 pump air feed-in
7 air flow meter
8 ceramic packed bed
9 thermocouple for gas temp
10 thermocouple for gas temp
11 thermocouple for sample temp.
12 measured data logger

Figure 3-5: Cylindrical samples of limestones from different sources
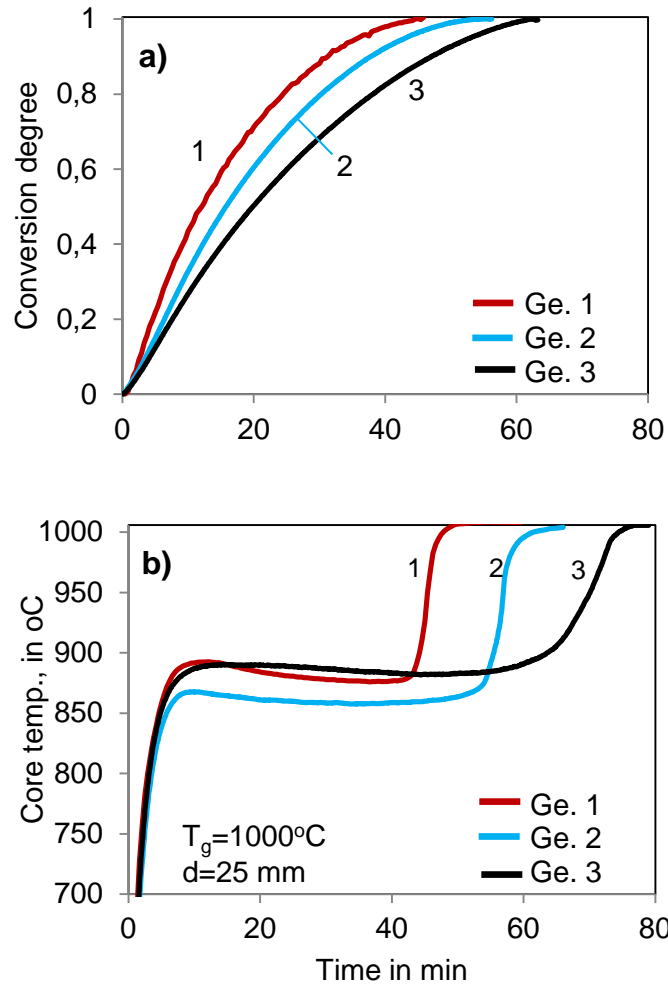
Figure 3-6: Conversion degree and calcination temperature of limestone of different origins

As an example, **Figure 3-6** shows the results of measuring the conversion degree and the core temperature for three different kinds of limestones from Germany. Experiments were carried out at the same furnace temperature of 1000 °C. It can be seen that the limestone Ge. 1 decomposes completely after 45 min while the limestone Ge. 3 needs a significant longer time with about 65 min. The limestone Ge. 2 is in between the two other samples. The calcination temperatures are also different. The limestone Ge. 2 has the lowest core temperature with about 860 °C and the limestone Ge. 3 has the highest core temperature with about 890 °C.

The material properties of three above limestones are determined by using an analytical solution given by Kainer et al. [38] and the results are shown in **Table 3-2**. It can be seen that the material properties are significantly different, especially the reaction coefficient and the pore diffusivity. The difference in the material properties causes the difference in the decomposition behavior.

28

Table 3-2 Properties of limestone of different origins

Limestone	$k \cdot 10^{-2}$, [m/s]	λ [W/m/K]	$D^P \cdot 10^{-4}$ [m^2/s]
Ge.1	0.98	0.70	1.63
Ge.2	0.76	0.74	1.28
Ge.3	0.54	0.73	2.4

4 Energy and mass balance

4.1 Energy and mass balance of normal shaft kiln

4.1.1 Process description

The schematic diagram of the normal shaft kiln is shown before in the Figure 1-1 with three operating sections: the preheating, the reaction and the cooling zones. To calculate the energy consumption, the reaction and the cooling zone have to be treated together and the preheating zone has to be separated, Bes [40]. This division is necessary because the gas temperature (T_g) between the preheating and the reaction zone has to be higher than the solid equilibrium temperature (T_{eq}) at that position so that the 2nd law of the thermodynamics is fulfilled, as shown in Error! Reference source not found.. This equilibrium position is called as 'pinch' point in chemical engineering. The balance is independent on the direction of the gas flow in the reaction zone. In case of the counter-current flow, the gas leaving the reaction zone has the highest CO_2 concentration at the transition to the preheating zone. Therefore, this CO_2 concentration determines the end of the preheating and the beginning of the reaction.
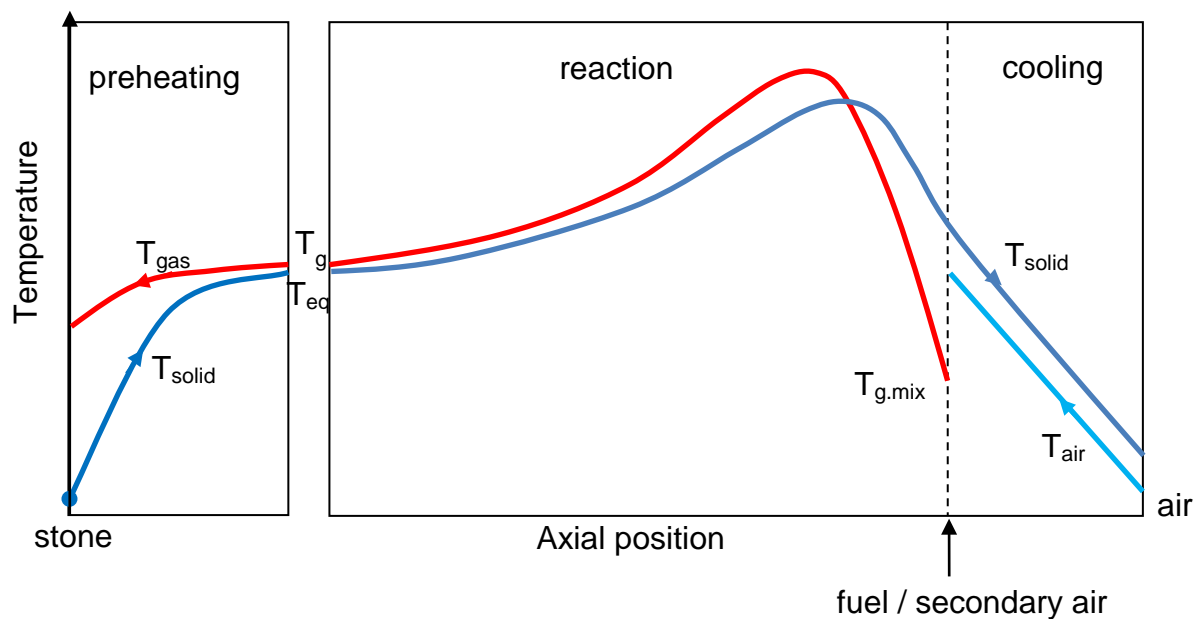

Figure 4-1: Principal temperature profiles in normal shaft kilns

4.1.2 Energy balance

Error! Reference source not found. shows the heat input and output flows in the reaction zone and the cooling zone. In these zones, the main heat input is the mass of fuel $\dot{M}_f$ multiplied by

its heating value h_u. The other heat inputs are from the limestone at equilibrium temperature T_{eq} and from the air. The heat from the limestone is $\dot{M}_{LS} \cdot c_{LS} \cdot T_{eq}$. The air flow is divided into the air flow through the cooling zone $\dot{M}_{ac}$ and the air flow blown into the kiln with the fuel $\dot{M}_{af}$. The air blown in with the fuel can be preheated (except transport air). Therefore, its temperature was denoted as T_{af}. The heat input for these two air flows $\dot{M}_a \cdot c_{pa} \cdot T_a$ is calculated relative to the ambient temperature T_e ($T_a = T_e$).
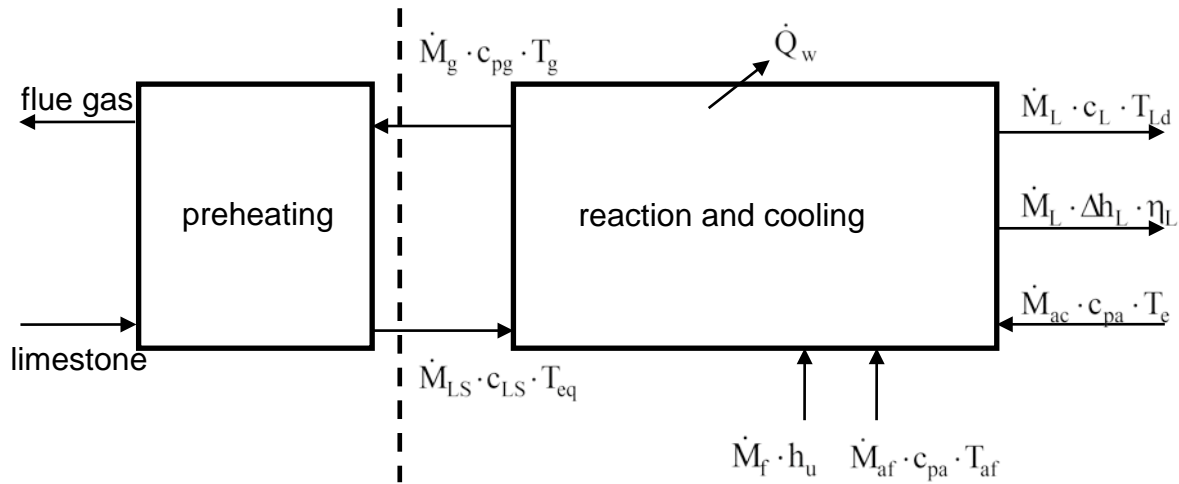
Figure 4-2: Heat inputs and outputs in the reaction and cooling zones of normal shaft kilns

The main energy output is the energy consumed by the limestone decomposition $\dot{M}_L \cdot \Delta h_L \cdot X_L$. Here, X_L is the conversion degree and $\Delta h_L = 3.18$ MJ/kg$_{lime}$ is the reaction enthalpy related to the ambient temperature. Experimental research results summarized by Chai and Navrotsky [41] mentioned the value $\Delta \tilde{h} = 178 \pm 1$ MJ/kmol. The other heat outputs are the heat output with the lime, the gas and the heat loss through the wall. The change of the flue gas and the lime mass flows due to the incomplete calcination can be neglected with an error smaller than 1%. The decomposition of the magnesite fraction is assumed to be equal to the limestone decomposition for simplifying and the evaporation enthalpy of the moisture in the limestone is neglected.

In heat balances, the enthalpies are always referred to the reference temperature $T_{ref.}$ (0 ^{o}C), Bes [40]. The sensible heat of the phase is given as:

$$\dot{Q} = \dot{M} \cdot c_p \cdot (T - T_{ref.}) = \dot{M} \cdot c_p \cdot (T - 0^o C) = \dot{M} \cdot c_p \cdot T \tag{4-1}$$

Here the temperature T is taken in degree Celsius.

The energy balance equation is given as:

$$\dot{M}_f \cdot h_u + \dot{M}_{ac} \cdot c_{pa} \cdot T_e + \dot{M}_{af} \cdot c_{pa} \cdot T_{af} + \dot{M}_{LS} \cdot c_{LS} \cdot T_{eq}$$
$$= \dot{M}_L \cdot c_L \cdot T_{Ld} + \dot{M}_L \cdot \Delta h_L \cdot X_L + \dot{M}_g \cdot c_{pg} \cdot T_g + \dot{Q}_w \tag{4-2}$$

The air mass flow depends on the air demand L, the kind of fuel, the air excess number λ_f and the operating conditions:

$$\dot{M}_a = \dot{M}_{ac} + \dot{M}_{af} = \lambda_f \cdot L \cdot \dot{M}_f \tag{4-3}$$

The mass flow of limestone $\dot{M}_{LS}$ is given by:

$$\dot{M}_{LS} = \dot{M}_L \cdot \frac{1}{1 - y_{CO_2}} \tag{4-4}$$

The flue gas mass flow $\dot{M}_g$ consists of the air flow, the fuel flow and the CO_2 flow produced by the calcination $\dot{M}_{CO_2L}$:

$$\dot{M}_g = \dot{M}_a + \dot{M}_f + \dot{M}_{CO_2L} \tag{4-5}$$

where the CO_2 flow produced by decomposition is given by:

$$\dot{M}_{CO_2L} = \dot{M}_{LS} \cdot y_{CO_2} = \frac{y_{CO_2}}{1 - y_{CO_2}} \cdot \dot{M}_L \tag{4-6}$$

From Eq. (4-2) - (4-6) the energy consumption per kg of lime is obtained.

$$E = \frac{\dot{M}_f \cdot h_u}{\dot{M}_L} = \frac{c_L \cdot T_{Ld} + \Delta h_L \cdot X_L + \dfrac{y_{CO_2}}{1 - y_{CO_2}} \cdot c_{pg} \cdot T_g - \dfrac{1}{1 - y_{CO_2}} \cdot c_{LS} \cdot T_{eq} + \dfrac{\dot{Q}_w}{\dot{M}_L}}{1 + [\lambda_f \cdot L \cdot c_{pa} \cdot T_e - (1 + \lambda_f \cdot L) \cdot c_{pg} \cdot T_g] / h_u} \tag{4-7}$$

There are different kinds of fuels commonly used in shaft kilns such as natural gas, lean gas, oil, lignite, anthracite and coal. For example, the composition, the air demand and the net heating values, for three types of fuel: natural gas, lignite and anthracite are shown in **Table 4-1** and **Table 4-2**.

Table 4-1 Composition in % Vol, air demand and net heating value of natural gas

	CH_4	C_2H_6	H_2	CO_2	CO	N_2	L [kg$_{air}$/kg$_{fuel}$]	h_u [MJ/kg$_{fuel}$]
Natural gas	0.93	0.05	0	0.01	0	0.01	16.1	47.7

Table 4-2 Composition (dry and ash free), air demand and net heating value of solid fuel

	C	H	O	S	N	Water	Ash	L [kg$_{air}$/kg$_{fuel}$]	h$_u$ [MJ/kg$_{fuel}$]
Anthracite	0.92	0.04	0.02	0.01	0.01	0.04	0.06	10.1	29.7
Lignite	0.70	0.05	0.25	-	-	0.10	0.06	6,8	20

To solve the Eq. (4-7) it is necessary to know the value of the equilibrium temperature T_{eq}, which has to be lower than the gas temperature T_g. Both temperatures are unknown. The equilibrium temperature depends on the carbon dioxide concentration and thus on the kind of fuel and the operating conditions. This dependence will be described in the following chapter.

4.1.3 Mass balance of CO$_2$

The carbon dioxide concentration in the flue gas decides the equilibrium temperature T_{eq} at which the decomposition starts. The CO_2 in the flue gas is produced by both the combustion of the fuel and the decomposition of the limestone. The carbon dioxide concentration in the flue gas leaving the reaction zone x_{CO_2fg} can be calculated from the mass balance of CO_2:

$$\dot{M}_{gf} \cdot x_{CO_2f} + \dot{M}_{CO_2L} = (\dot{M}_{gf} + \dot{M}_{CO_2L}) \cdot x_{CO_2fg} \tag{4-8}$$

The mass flow of CO_2 produced by the fuel combustion $\dot{M}_{gf} \cdot x_{CO_2f}$ and the mass flow of CO_2 produced by the limestone decomposition $\dot{M}_{CO_2L}$ leave the reaction zone with total gas flow:

$$\dot{M}_g = \dot{M}_{gf} + \dot{M}_{CO_2L} \tag{4-9}$$

The mass flow of combustion gas depends on the mass flow of the fuel and the air as:

$$\dot{M}_{gf} = \dot{M}_a + \dot{M}_f = (1 + \lambda_f \cdot L) \cdot \dot{M}_f \tag{4-10}$$

The CO_2 concentration x_{CO_2f} in the combustion gas is determined according to Specht [42].

The CO_2 flow produced by decomposition is given by:

$$\dot{M}_{CO_2L} = \dot{M}_{LS} \cdot y_{CO_2} = \frac{y_{CO_2}}{1 - y_{CO_2}} \cdot \dot{M}_L \tag{4-11}$$

The lime mass flow $\dot{M}_L$ can be replaced by the energy consumption E.

$$E = \frac{\dot{M}_f \cdot h_u}{\dot{M}_L} \qquad (4\text{-}12)$$

Then the CO_2 concentration of the flue gas leaving the reaction zone is calculated as:

$$x_{CO_2fg} = \frac{E \cdot (1 + \lambda_f \cdot L) \cdot x_{CO_2f(\lambda_f)} + \frac{y_{CO_2}}{1 - y_{CO_2}} \cdot h_u}{E \cdot (1 + \lambda_f \cdot L) + \frac{y_{CO_2}}{1 - y_{CO_2}} \cdot h_u} \qquad (4\text{-}13)$$

From Eq. (4-13), it can be seen that the CO_2 fraction in the flue gas depends on the energy consumption E, the air excess number λ_f, the type of limestone y_{CO_2} and the kind of fuel h_u.

4.1.4 Equilibrium temperature

As mentioned above, to solve the energy balance equation, Eq. (4-7), it is necessary to know the equilibrium temperature T_{eq} at which the decomposition begins. This temperature is a function of the CO_2 concentration x_{CO_2fg} or the CO_2 partial pressure in the flue gas P_{CO_2}. The equilibrium temperature T_{eq} is obtained from the Eq.(3-10) in the chapter 3 as:

$$T_{eq} = \frac{\Delta H_R}{R} \cdot \left[\ln\left(\frac{P_o}{P_{CO_2}}\right) \right]^{-1} \qquad (4\text{-}14)$$

where the CO_2 partial pressure P_{CO_2}, which depends on the CO_2 concentration and the kiln pressure P_{kiln}, is calculated as:

$$P_{CO_2} = x_{CO_2fg} \cdot P_{kiln} \qquad (4\text{-}15)$$

From Eq. (4-13) to Eq. (4-15), it can be seen that the equilibrium temperature also depends on the energy consumption, the air excess number, the type of limestone and the kind of fuel.

As an example, **Figure 4-3** and Figure 4-4 show the CO_2 concentrations and calcination temperatures for natural gas and lignite fuel as functions of the excess air number. The energy consumptions of E = 3.8 MJ/kg$_{lime}$ and E = 4.5 MJ/kg$_{lime}$ which correspond to a relatively low and high energy usage were taken. The lower the energy consumption and the air excess number, the higher is the carbon dioxide concentration. Lignite gives the higher CO_2 in the flue gas. The line for E = 3.8 MJ/kg$_{lime}$ for lignite ends at $\lambda_f = 1.05$, since for the higher excess

34

air numbers, such so low energy consumption is no more possible. Similarly the line for E = 3.8 MJ/kg$_{lime}$ for natural gas ends at $\lambda_f = 1.3$.

4.1.5   Energy consumption

With the set of equations given previously, the energy consumption can be calculated iteratively. In Eq. (4-7) all values are known except the gas temperature T_g between the preheating and the reaction zone. This temperature depends on the heat exchange, the zone length and the lime throughput and thus on the kinetic of the process. The larger the heat transfer and the higher the kiln, the smaller is the difference in temperature between gas and solid. Because the gas temperature T_g is unknown hence its value was taken as parameter for the following calculations.

Figure 4-5 shows the energy consumption as a function of the difference in temperature at the transition to the reaction zone $\Delta T_{eq} = T_g - T_{eq}$ for some typical fuels. For the calculation a residual CO_2 of 2 %, a heat loss through the wall of 200 kJ/kg$_{lime}$, a CO_2 mass fraction in the limestone $y_{CO2} = 0.42$ kg$_{CO2}$/kg$_{LS}$, a lime discharge temperature $T_{Ld} = 80°C$ and an air excess number of $\lambda = 1.2$ were assumed. The energy consumption for the temperature difference $\Delta T_{eq} = 0$ is the minimum possible value. It can be seen that the energy consumption increases linearly with the increase of the temperature difference.

Other calculations, which investigate the influences of the excess air number, the type of fuel, the type of limestone and the wall loss on the energy consumption, can be seen from Bes [40].
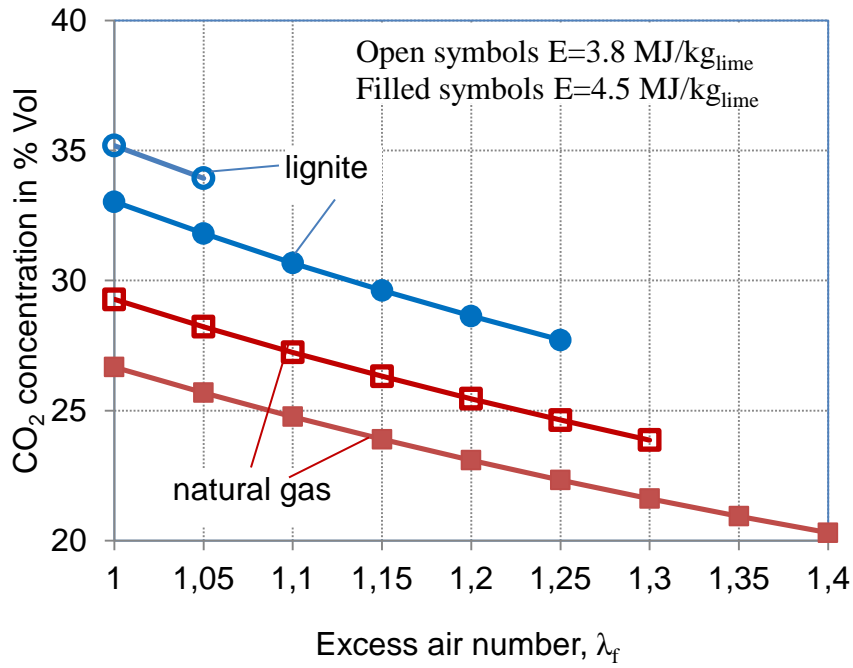
Figure 4-3: CO_2 concentration in the flue gas
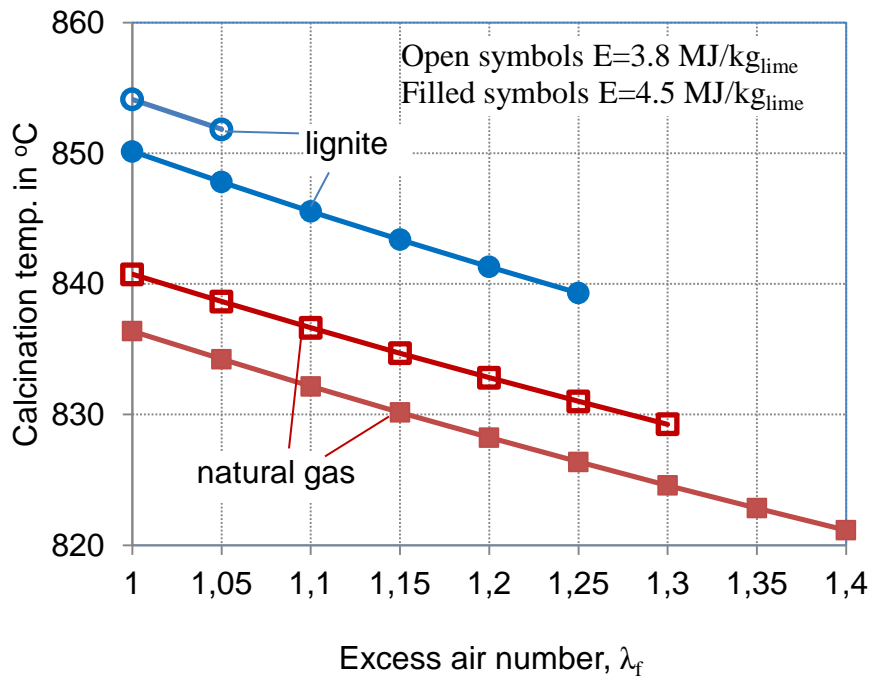
Figure 4-4: Starting calcination temperature
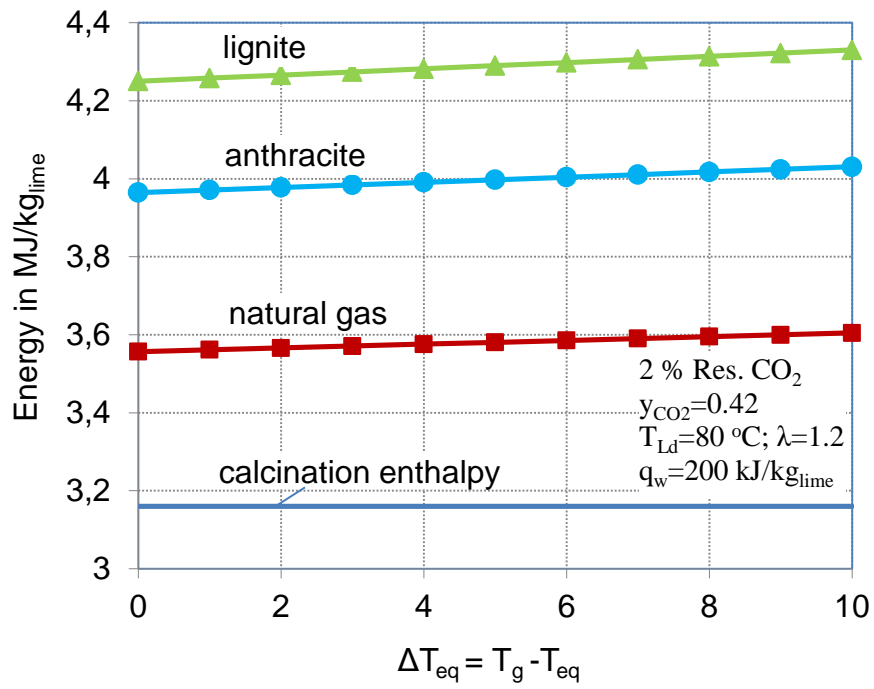
Figure 4-5: Energy consumption as function temperature difference between gas and solid at the beginning of burning zone

4.2 Energy and mass balance of PFR kiln

4.2.1 Process description

As shown before in the Figure 1-3, the PFR kiln consists of two connected shafts. Each shaft is subject to two distinct modes of operation, burning (firing) and non-burning (preheating). One shaft operates in the firing mode the other shaft operates simultaneously in the preheating mode. The alternative firing/preheating shaft sequence serves as a regenerative preheating process. Heat is transferred to the limestone from the flue gas during the preheating mode and then the heat is reclaimed by the combustion air from the limestone during the firing mode. Therefore, the preheating mode acts as a heat regenerator with the stone charge.

Figure 4-6 shows principal temperature profiles in the PFR kilns. The temperature profiles are demonstrated for three operating zones: the preheating, the reaction and the cooling zones in the same manner as shown before in the normal shaft kilns. A remark here is that with the PFR kilns, the preheating zone acts as a heat regenerator since the stone gets heat from the flue gas then it transfers heat to the combustion air. As a simplification for the energy balance, it can be assumed that the preheating zone has two heat exchangers: the first one is used for the heat transfer process from the flue gas to the stone; the second one is used for the heat transfer process from the stone to the combustion air. These two heat exchangers are interconnected.

Similar to the normal shaft kilns, the energy balance is done with handling together the reaction and the cooling zones. However, calculations must take into account the effects of the alternative heat transfer, in which the combustion air is preheated by the stone before entering the reaction zone.
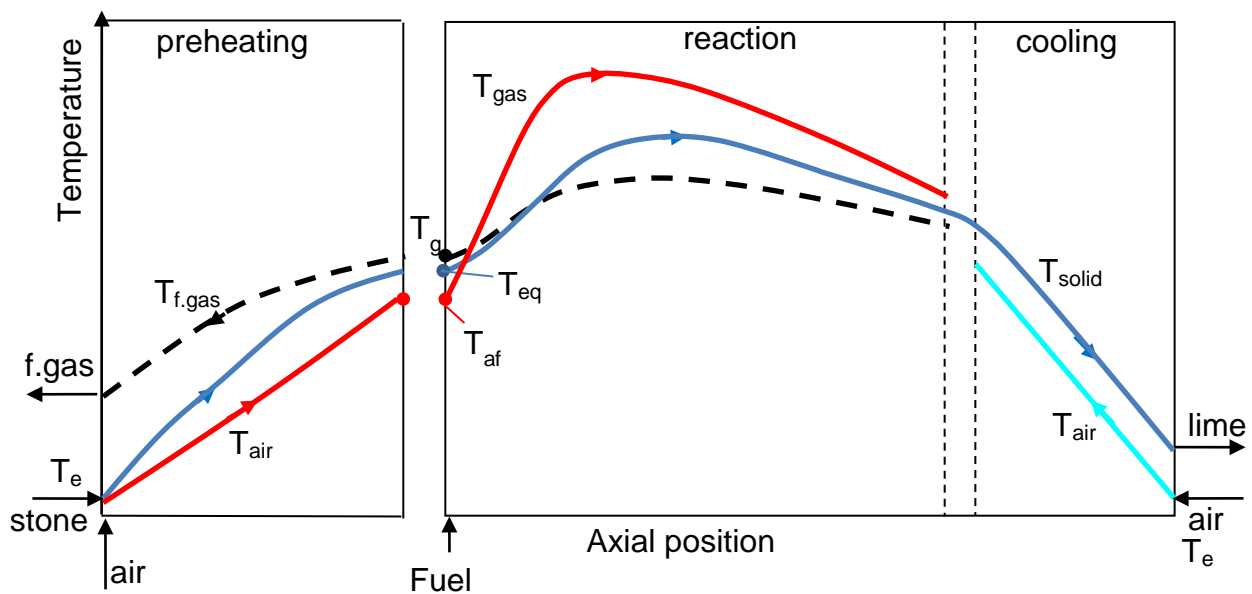
Figure 4-6: Principal temperature profiles in the PFR kilns

38
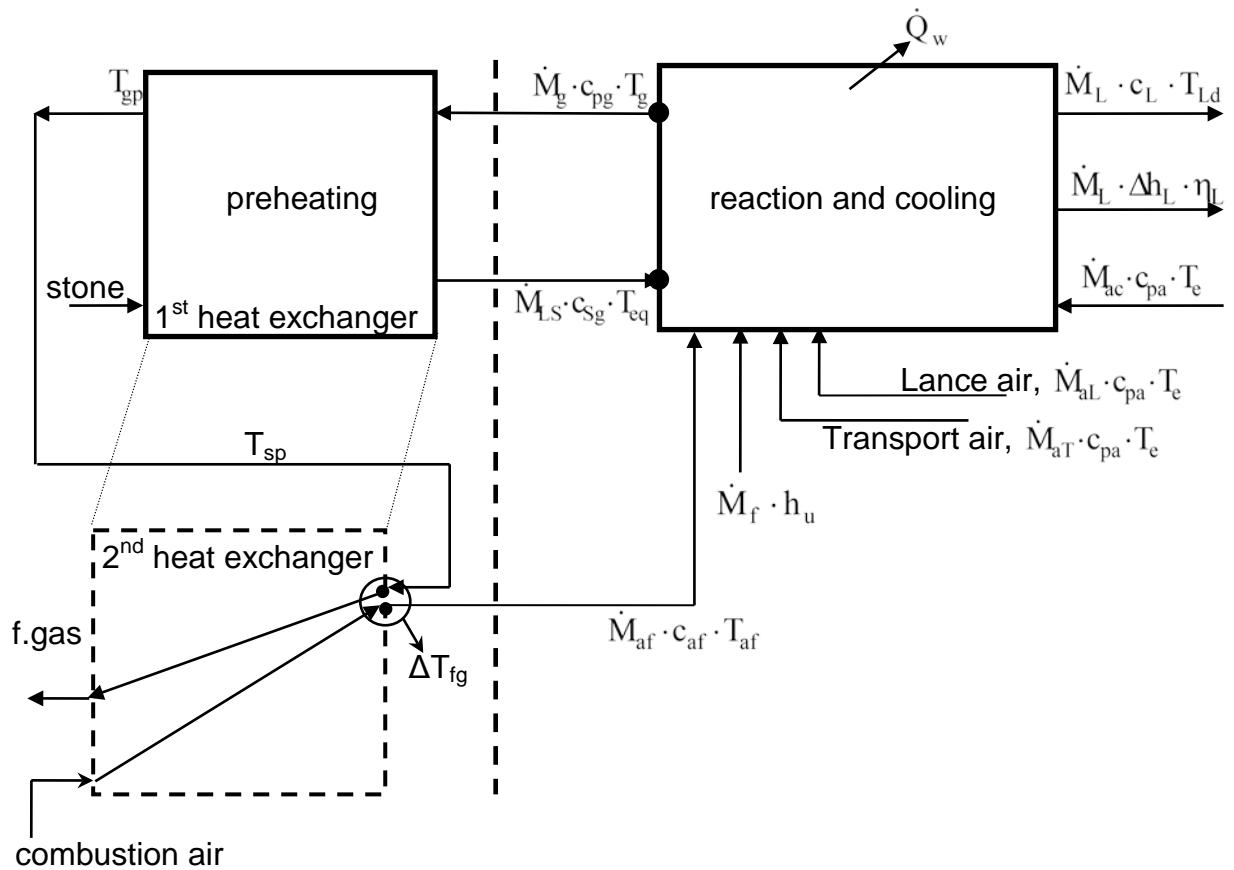
Figure 4-7: Heat inputs and outputs in the reaction and cooling zones of the PFR kilns

4.2.2 Energy balance

Figure 4-7 shows the heat flow inputs and outputs in the reaction and the cooling zones as well as the preheating zone (including additional heater). The energy balance is done for the reaction and the cooling zones, where the main heat input for these zones is from the fuel $\dot{M}_f \cdot h_u$. The other heat inputs are from the limestone at the equilibrium temperature T_{eq} and from the air. The heat from the limestone is $\dot{M}_{LS} \cdot c_{LS} \cdot T_{eq}$. The air flow includes the combustion air flow $\dot{M}_{af}$ which comes to the reaction zone at the preheated air temperature T_{af}, the cooling air flow $\dot{M}_{ac}$ and the lance-cooling air flow $\dot{M}_{aL}$. In case of using solid fuel, an additional air is added to transport the solid fuel through the lances, so called transport air, $\dot{M}_{aT}$. The heat of the cooling air $\dot{M}_{ac} \cdot c_{pa} \cdot T_e$, the heat of the lance-cooling air $\dot{M}_{aL} \cdot c_{pa} \cdot T_e$ and that of the transport air $\dot{M}_{aT} \cdot c_{pa} \cdot T_e$ are calculated relative to the ambient temperature T_e. The heat of the combustion air $\dot{M}_{af} \cdot C_{pa} \cdot T_{af}$ is calculated with respect to the preheated air temperature T_{af}. This temperature is also an unknown parameter and it will be discussed in the next parts.

The heat output is considered the same as the normal shaft kiln which includes the main heat consumed by the limestone decomposition $\dot{M}_L \cdot \Delta h_L \cdot X_L$. The other heat outputs are the heat output with the lime $\dot{M}_L \cdot c_L \cdot T_{Ld}$, with the gas $\dot{M}_g \cdot c_{pg} \cdot T_g$ and the heat loss by the wall $\dot{Q}_w$.

Then the energy balance in the PFR kiln can be determined as:

$$\dot{M}_f \cdot h_u + \dot{M}_{af} \cdot c_{pa} \cdot T_{af} + \dot{M}_{ac} \cdot c_{pa} \cdot T_e + \dot{M}_{aL} \cdot c_{pa} \cdot T_e + \dot{M}_{aT} \cdot c_{pa} \cdot T_e + \dot{M}_{LS} \cdot c_{LS} \cdot T_{eq}$$
$$= \dot{M}_L \cdot c_L \cdot T_{Ld} + \dot{M}_L \cdot \Delta h_L \cdot X_L + \dot{M}_g \cdot c_{pg} \cdot T_g + \dot{Q}_w \tag{4-16}$$

In this equation the temperature T is taken in degree Celsius, ^{o}C.

The combustion air mass flow is calculated as:

$$\dot{M}_{af} = \lambda_f \cdot L \cdot \dot{M}_f \tag{4-17}$$

where λ_f is the excess air number, which represents the combustion air, it is also called as effective excess air number. This λ_f is smaller than the total excess air number, which will be defined in the next.

The cooling air flow depends on the cooling air factor γ_{ac} (m^{3}air/kg$_{lime}$).

$$\dot{M}_{ac} = \gamma_{ac} \cdot \rho_a \cdot \dot{M}_L \tag{4-18}$$

with ρ_a is the density of the air at the ambient temperature.

The lance-cooling air flow depends on the lance-cooling air factor γ_{aL} (m^{3}air/kg$_{lime}$).

$$\dot{M}_{aL} = \gamma_{aL} \cdot \rho_a \cdot \dot{M}_L \tag{4-19}$$

The transport air flow depends on the transport air factor γ_{aT} (m^{3}air/kg$_{lime}$).

$$\dot{M}_{aT} = \gamma_{aT} \cdot \rho_a \cdot \dot{M}_L \tag{4-20}$$

Then the total air flow blown into the kiln is summarized as:

$$\dot{M}_a = \dot{M}_{af} + \dot{M}_{ac} + \dot{M}_{aL} + \dot{M}_{aT} = \lambda_{total} \cdot L \cdot \dot{M}_f \tag{4-21}$$

while λ_{total} is the total excess air number.

The flue gas mass flow consists of the total air flow, the fuel flow and the CO_2 flow produced by the calcination:

$$\dot{M}_g = \dot{M}_a + \dot{M}_f + \dot{M}_{CO_2L}$$
(4-22)

The CO_2 flow produced by the decomposition is determined as before. Therefore, the energy consumption per kg of lime in the PFR kiln is obtained finally as:

$$E = \frac{c_L \cdot T_{Ld} + \Delta h_L \cdot X_L + \dfrac{y_{CO_2}}{1 - y_{CO_2}} \cdot c_{pg} \cdot T_g - \dfrac{1}{1 - y_{CO_2}} \cdot c_{LS} \cdot T_{eq} - \left(\gamma_{ac} + \gamma_{aL} + \gamma_{aT}\right) \cdot \rho_a \cdot c_{pa} \cdot T_e + \dfrac{\dot{Q}_w}{\dot{M}_L}}{1 + [\lambda_f \cdot L \cdot c_{pa} \cdot T_{af} - \left(1 + \lambda_f \cdot L\right) \cdot c_{pg} \cdot T_g] / h_u}$$
(4-23)

With the set of equations given previously, the energy consumption can be calculated iteratively. In Eq. (4-23) all values are now known except the gas temperature T_g and the preheated combustion air temperature T_{af}. The gas temperature T_g is determined by the way as same as the normal shaft kiln with introducing the temperature difference parameter ΔT_{eq} at the 'pinch' point. The preheated combustion air temperature T_{af} is considered as a parameter for the calculation as well. This temperature will be defined as a function of the stone temperature in the preheating zone T_{sp}. The details of determination of T_{af} will be provided in the next paragraph.

The limestone temperature in the preheating zone (the first heat changer) T_{sp} can be assumed as the gas temperature T_{gp}, which leaves the first heat exchanger to the second heat changer, Figure 4-7. This gas temperature T_{gp} is calculated from the energy balance in the first heat exchanger.

$$\dot{M}_g \cdot c_{pg} \cdot \left(T_g - T_{gp}\right) = \dot{M}_{LS} \cdot c_{LS} \cdot \left(T_{eq} - T_e\right)$$
(4-24)

The temperature T_{sp} ($T_{sp} = T_{gp}$) represents the limestone temperature in the preheating zone during the burning mode. Therefore, it depends on the alternative heat transfer in which the flue gas gives heat to the stone (in the non-burning mode) and then the stone transfers heat to the combustion air (in the burning mode). The temperature T_{gp} is also affected by the preheating zone length and the operating conditions.

Then the energy consumption in Eq. (4-23) can be calculated, where the unknown parameter T_{af} is considered as a function of the limestone temperature T_{sp} by introducing the temperature difference ΔT_{fg} defined as:

$$\Delta T_{fg} = T_{sp} - T_{af}$$
(4-25)

41

The temperature difference ΔT_{fg} will be considered as a parameter for next calculations. This difference is affected by the heat transfer between the stone and the combustion air and the preheating zone length. The larger the heat transfer and the longer the preheating zone, the smaller the difference in temperature between the combustion air and the limestone.

4.2.3   Mass balance of CO_2

Similar to the normal shaft kiln, the CO_2 concentration in the burning shaft of the PFR kiln decides the temperature, at which the calcination begins. The CO_2 is produced by the combustion of the fuel and the calcination of the limestone. The mass balance equation for the CO_2 in the firing zone of the burning shaft is given by:

$$\dot{M}_{gf} \cdot x_{CO_2f} + \dot{M}_{CO_2L} = \left(\dot{M}_{gf} + \dot{M}_{CO_2L}\right) \cdot x_{CO_2bg} \tag{4-26}$$

where $\dot{M}_{gf} \cdot x_{CO_2f}$ is the mass flow of CO_2 produced by the fuel combustion and $\dot{M}_{CO_2L}$ is the mass flow of CO_2 produced by the limestone decomposition.

The combustion gas flow, which includes the combustion air and the fuel flow, is given as:

$$\dot{M}_{gf} = \dot{M}_{af} + \dot{M}_f = \left(1 + \lambda_f \cdot L\right) \cdot \dot{M}_f \tag{4-27}$$

The CO_2 flow produced by decomposition is given by:

$$\dot{M}_{CO_2L} = \dot{M}_{LS} \cdot y_{CO_2} = \frac{y_{CO_2}}{1 - y_{CO_2}} \cdot \dot{M}_L \tag{4-28}$$

The lime mass flow $\dot{M}_L$ can be replaced by the energy consumption E as before.

$$E = \frac{\dot{M}_f \cdot h_u}{\dot{M}_L} \tag{4-29}$$

Finally, the CO_2 concentration in the firing zone of the burning shaft x_{CO_2bg} is calculated.

$$x_{CO_2bg} = \frac{E \cdot \left(1 + \lambda_f \cdot L\right) \cdot x_{CO_2f(\lambda_f)} + \dfrac{y_{CO_2}}{1 - y_{CO_2}} \cdot h_u}{E \cdot \left(1 + \lambda_f \cdot L\right) + \dfrac{y_{CO_2}}{1 - y_{CO_2}} \cdot h_u} \tag{4-30}$$

From Eq. (4-30), it can be seen that the CO_2 concentration in the burning shaft depends on the energy consumption E, the excess air number λ_f, the type of limestone y_{CO_2} and the kind of fuel with h_u and x_{CO_2f}.

4.2.4   Equilibrium temperature

The equilibrium temperature of the PFR kiln is calculated in the same way as that of the normal shaft kiln as well. This temperature is also a function of CO_2 concentration in the burning shaft, which is defined in Eq. (4-30). Thus, it depends on the energy consumption, the effective excess air number, the type of limestone and the kind of fuel.
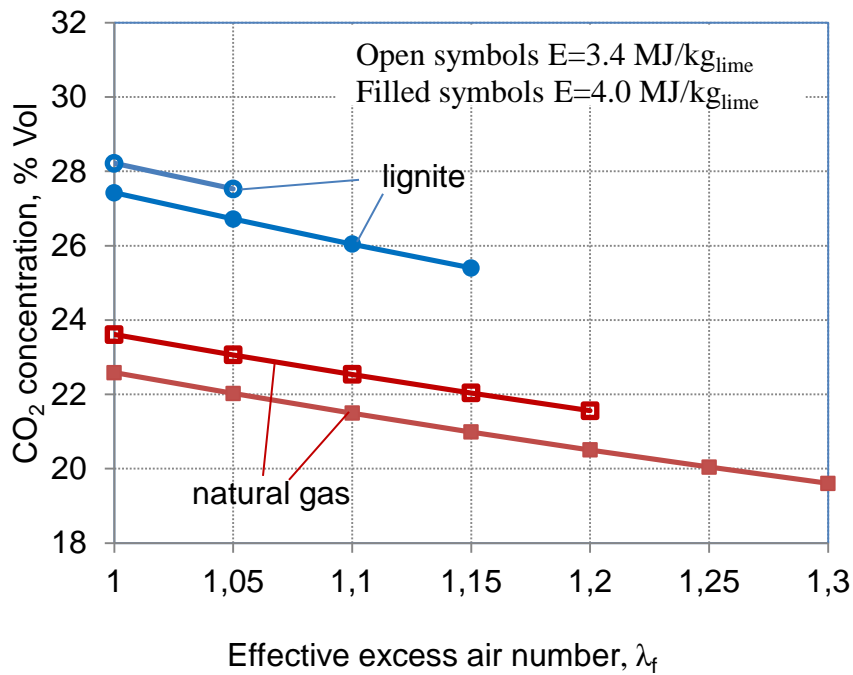
Figure 4-8: CO_2 concentration in the firing zone of the PFR kilns
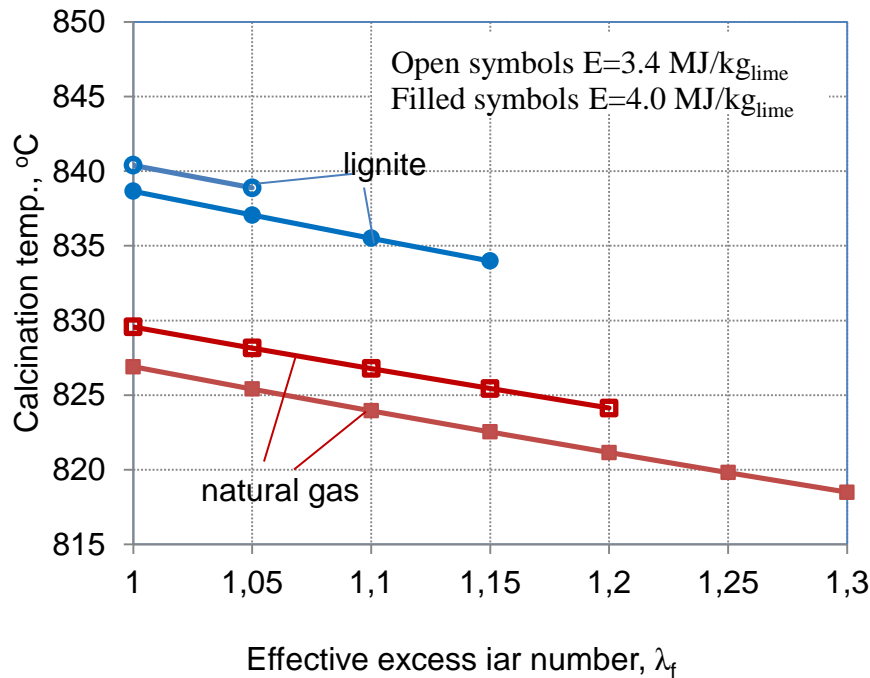
Figure 4-9: Starting calcination temperature in the firing zone of the PFR kilns

As an example, **Figure 4-8** and **Figure 4-9** show the CO_2 concentrations and calcination temperatures for natural gas and lignite depending on the effective excess air number. The energy consumptions E = 3.4 MJ/kg$_{lime}$ and E = 4.0 MJ/kg$_{lime}$ that correspond to a relatively low and high value of energy usage were taken. The lower the energy consumption and the air excess number are, the higher the carbon dioxide concentration is. Lignite gives the higher CO_2 in the gas phase. The lines for E = 3.4 MJ/kg$_{lime}$ and E = 4.0 MJ/kg$_{lime}$ for lignite end at λ_f = 1.05 and λ_f = 1.15, as for the higher excess air numbers, further low energy consumption is no more possible.

It is remarkable here that the CO_2 concentration in the flue gas and the equilibrium temperature in the PFR kilns are significantly lower than those in the normal shaft kilns. The reason is that the total excess air number in the PFR kilns is much higher since it includes the combustion air, the cooling air, the lance-cooling air and the transport air. As an example, **Figure 4-10** shows some calculated values of the total excess air number in dependence on the effective excess air number. The calculations were done with natural gas fuel and the cooling air factor (γ_{ac}) varying in the range of 0.6 - 0.7 m^3$_{air}$/kg$_{lime}$. It can be seen from the figure that while the effective air number changes from 1.0 to 1.2, the total excess air number varies in the range from 1.75 to 2.1.
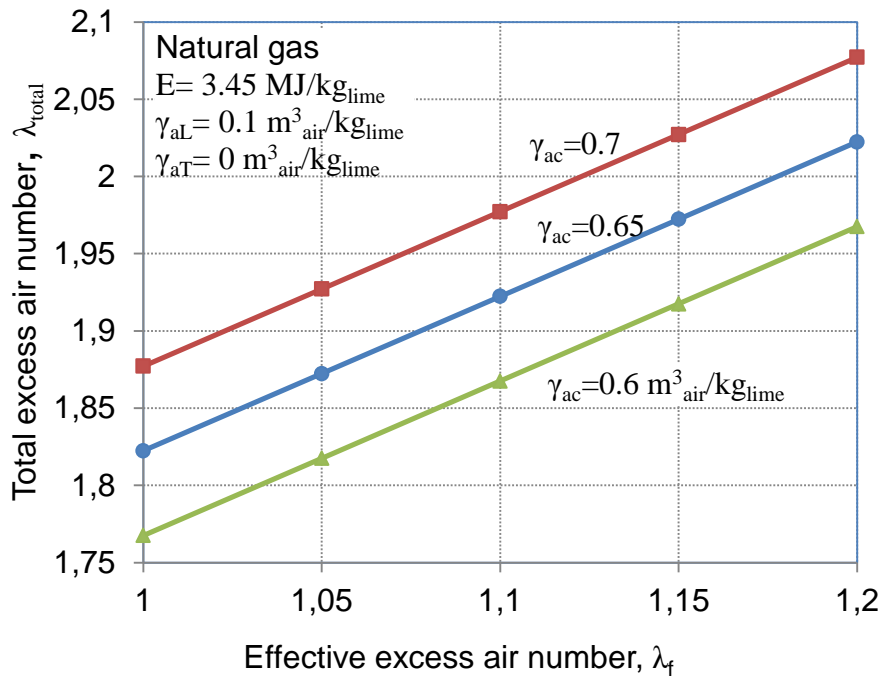
Figure 4-10: Total excess air number in the PFR kilns

4.2.5 Energy consumption

a) Influences of temperature difference between limestone and preheated air

The energy consumption can be calculated iteratively by Eq. (4-23) where all values are known except the gas temperature T_g and the preheated combustion air temperature T_{af}. The T_g is determined by the method as same as the normal shaft kiln by introducing the temperature difference ΔT_{eq}. The T_{af} is defined by means of introducing the temperature difference between the combustion air and the limestone ΔT_{fg} as discussed previously.

Figure 4-11 shows the influence of the ΔT_{fg} on the energy consumption. For the calculation a of 2 %, a heat loss through the wall of 200 kJ/kg$_{lime}$, a CO_2 mass fraction in the limestone y_{CO2} =0.42 kg$_{CO2}$/kg$_{l.stone}$, a lime discharge temperature T_{Ld} = 80°C and an air excess number of 1.2 were assumed. The influence of the ΔT_{fg} was investigated in the range from 0 to 10 K. The results have shown that with the increase of this temperature difference in the calculated range, there is no significant change in the energy consumption. Therefore, the influence of this temperature difference is also relatively low and it was set to 5 K in the further calculations.

A remark here is that the energy consumption required for the PFR kiln is obviously lower than that of the normal shaft kiln. For example, with the same lignite fuel and the excess air number of about 1.2, the energy consumption of the PFR kiln is about 3.8 MJ/kg$_{lime}$ while that

of the normal shaft kiln is almost 4.2 MJ/kg$_{lime}$. This reduction of the energy is a result of regenerative heat transfer arrangement in the PFR kilns, [43,44].
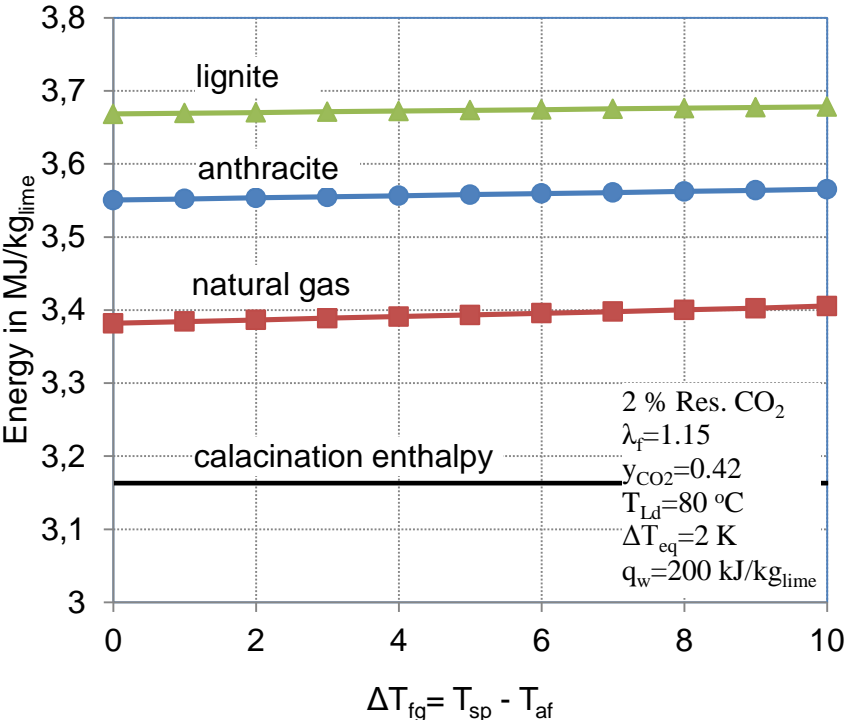
Figure 4-11: Energy consumption as function of temperature difference between stone and combustion air at the beginning of burning zone

b) Influences of types of fuel

Figure 4-12 shows the energy consumption as a function of the kind of fuel and the effective excess air number. Calculations were done with three fuels natural gas, lignite and anthracite. The other inputs were kept the same as the previous calculation. It can be seen that at the same excess air number, the lignite fuel requires the highest energy consumption while the natural gas requires the lowest energy consumption. The energy consumption increases considerably with the increase of the excess air number.

The chart contains the following annotations:

2 % Res. CO_2
$y_{CO2}=0.42$
$T_{Ld}=80\ °C$
$\Delta T_{eq}=2\ K$; $\Delta T_{fg}=5\ K$
$q_w=200\ kJ/kg_{lime}$
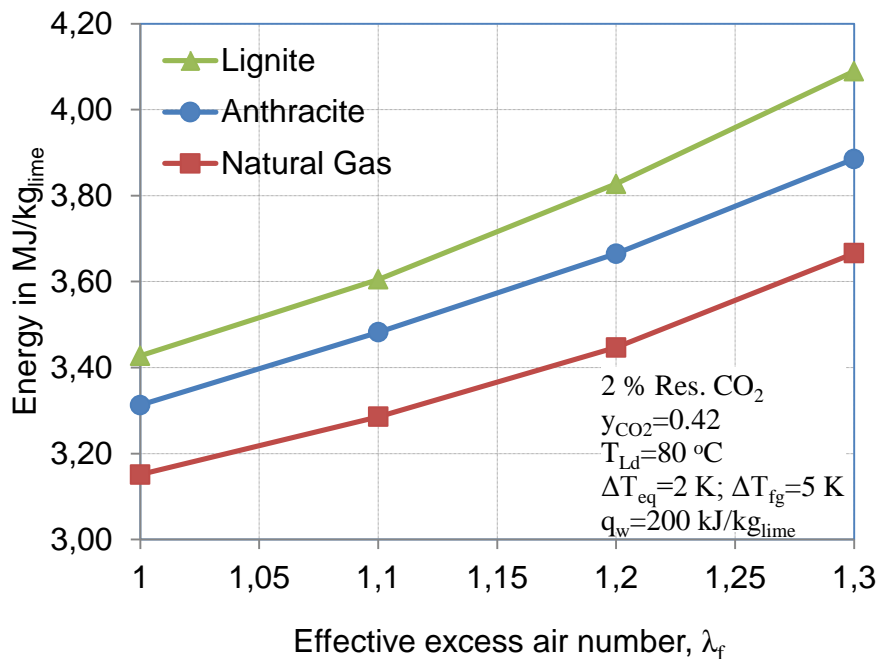
Figure 4-12: Energy consumption for different fuel as function of excess air number

c) Influences of types of limestone

Figure 4-13 shows the energy consumption as a function of the CO_2 mass fraction in the limestone. The calculation was done for three values of CO_2 residual with respect to 0%, 1% and 2% and the fuel used is the natural gas. The other parameters were kept the same as the previous calculation. It can be seen that the energy consumption increases almost linearly with the CO_2 mass fraction. Additionally, the energy consumption decreases while the residual CO_2 increases.

d) Influences of heat loss by kiln wall

Finally, the influence of the heat loss on the energy consumption is discussed in **Figure 4-14**. The energy consumption is shown again in dependence on the air excess number for the two types of fuel natural gas and lignite. The other input parameters were kept as the same as before, however additionally for an adiabatic wall, the wall without heat loss is considered. It can be seen that the energy difference is 270 to 330 kJ/kg_{lime}, which is about 35 to 70 % more than the heat loss of 200 kJ/kg_{lime}. The reason is that the energy to cover the heat loss has to be generated with a low pyrotechnical efficiency because the temperature of the gas leaving the reaction zone is high. As a result, the actual heat loss is much higher than the portion transferred through the wall.
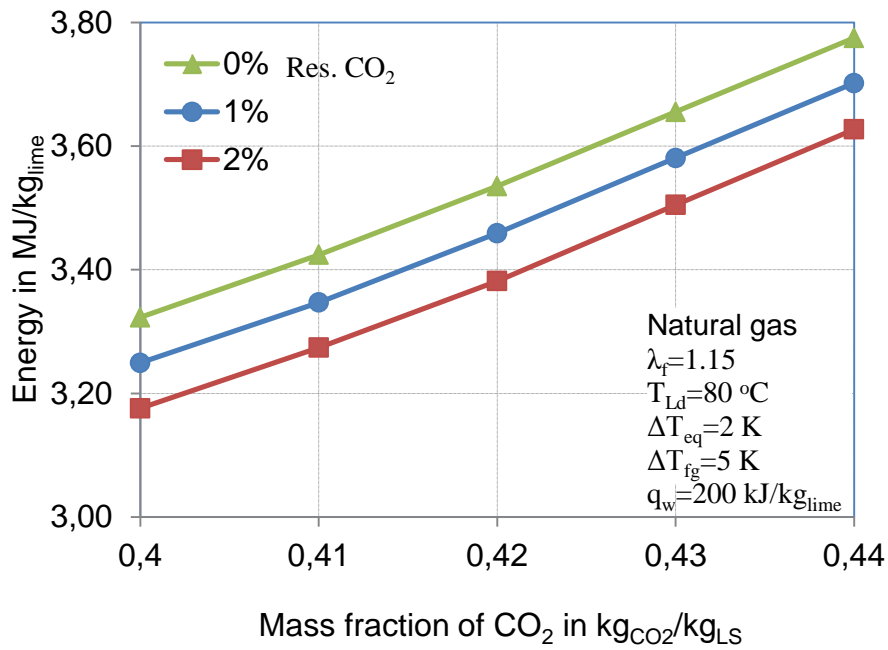
Figure 4-13: Energy consumption as function of mass fraction of CO_2 in limestone
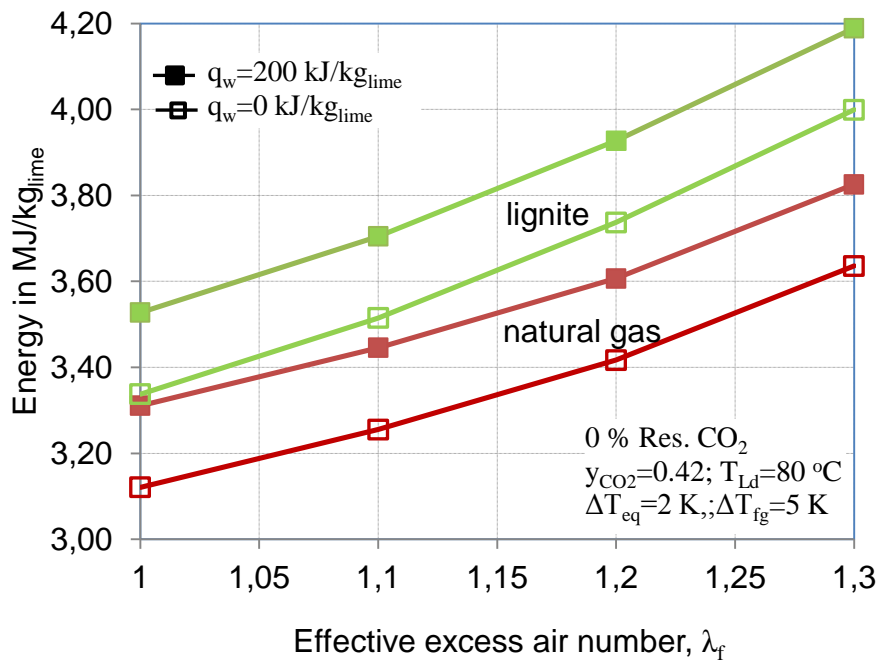
Figure 4-14: Energy usage with and without heat lost through the kiln wall

4.3 Conclusions

The theoretical minimum values of the specific energy consumptions required for the normal shaft kilns and the PFR kilns are determined in this chapter. The energy consumption depends on the following parameters:

- The conversion degree of lime or residual CO_2: The higher the lime conversion degree (lower residual CO_2), the higher the energy consumption

- The type of limestone: E.g., the higher the mass fraction of CO_2 in limestone (more $CaCO_3$), the more the energy required

- The types of fuel: E.g., the lower the heating value of the fuel, the higher the energy consumption

- The excess air number: The larger the excess air number, the more energy consumption required

- The temperature difference between the gas and solid at the 'pinch' point: The higher the temperature difference, the higher the energy consumption

- The alternative heat transfer from the flue gas to the limestone and to the combustion air (PFR kilns only): The better the heat transfer process (the higher the preheated combustion air temperature), the lower the energy consumption

Results of calculations have revealed that due to the regenerative heat transfer (reusing the flue gas for preheating the limestone), the energy consumption required for the PFR kilns is significantly lower than that of the normal shaft kilns.

In the above calculations of the energy consumption, it was assumed that the lime discharge temperature, the flue gas temperature, the residual CO_2 and the heat loss are known as inputs for calculations. However, they are strongly affected by operating conditions of the burning process. Therefore, they must be determined by mathematical modeling, which will be presented in the next chapters.

5 Simulation of lime calcination in normal shaft kiln

5.1 Mathematical model

5.1.1 Energy balance equation

a) Preheating and cooling zone

The energy balance is established for the gas (g) and the solid (s) in a section of kiln length dz, **Figure 5-1**. In the preheating and the cooling zones, the solid particles are heated up and cooled down by the gas, thus these two zones can be considered as heat exchangers. The energy balance equations are described as:

solid$_{in}$　　　　　　　　　gas$_{out}$

$$\dot{M}_{s(z)} \cdot c_{ps} \cdot (T_{s(z)} - T_{s.ref}) \qquad \dot{M}_{g(z)} \cdot c_{pg} \cdot (T_{g(z)} - T_{g.ref})$$

dz

$$\dot{M}_{s(z+dz)} \cdot c_{ps} \cdot (T_{s(z+dz)} - T_{s.ref}) \qquad \dot{M}_{g(z+dz)} \cdot c_{pg} \cdot (T_{g(z+dz)} - T_{g.ref})$$

solid$_{out}$　　　　　　　　　gas$_{in}$
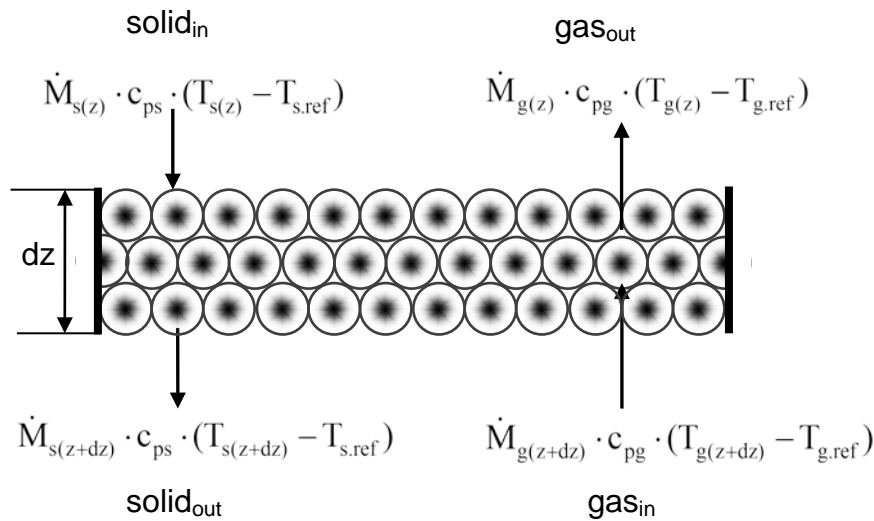
Figure 5-1: Scheme of normal shaft kilns with a section length dz

- **For the gas**

$$\dot{M}_g \cdot c_{pg} \cdot \frac{dT_{g(z)}}{dz} = \alpha_{\kappa(z)} \cdot A_F \cdot O \cdot (1 - \psi) \cdot (T_g - T_s) - \frac{d\dot{Q}_{w(z)}}{dz} \tag{5-1}$$

The change of the gas enthalpy flow is equal to the heat transferred between the gas and the solid and the local wall heat loss.

- **For the solid**

$$\dot{M}_s \cdot c_{ps} \cdot \frac{dT_{s(z)}}{dz} = \alpha_{\kappa(z)} \cdot A_F \cdot O \cdot (1 - \psi) \cdot (T_s - T_g) \qquad (5\text{-}2)$$

The change of the solid enthalpy flow is equal to the heat transferred between the gas and the solid. Here $\dot{M}$ represents the mass flow, c_p the specific heat capacity, T the temperature, α_κ the overall heat transfer coefficient, A_F the cross-sectional area of the furnace, O the specific surface of the stones in m^2/m^3, ψ the void fraction of the bed and $\dot{Q}_w$ the local wall heat loss.

It is known that the heating-up or the cooling-down of solid particles is a transient process, in which a solid particle has a temperature distribution in a radical direction. However, to simplify for the energy balance, the solid temperature is considered as the mean value. Therefore, in the above equations the overall heat transfer coefficient is used.

In Eq.(5-1), the local wall heat loss ($\dot{Q}_w$) is due to the heat loss by conduction ($\dot{Q}_{w\lambda}$) through the wall, which is determined (e.g., for a circular cross-section) as:

$$\dot{Q}_{w\lambda(z)} = 2\pi L R_w \cdot \lambda_w \cdot (T_{ki(z)} - T_{kw(z)}) / \ln(R_w / R_{in}) \qquad (5\text{-}3)$$

with λ_w is the wall thermal conductivity, R_{in} and R_w are the kiln inner and outer radius, T_{ki} and T_{kw} are the wall inner and outer temperatures, **Figure 5-2**. The T_{ki} is assumed as the gas temperature T_g, and T_{kw} is calculated from the heat balance at the wall surface as:

$$\dot{Q}_{w\lambda(z)} = \dot{Q}_{wc(z)} + \dot{Q}_{wr(z)} = 2\pi L R_w \cdot \left(\alpha_w \cdot (T_{kw(z)} - T_e) + \sigma \cdot \varepsilon \cdot T_{kw(z)}^4 \right) \qquad (5\text{-}4)$$

where ($\dot{Q}_{wc}$) and ($\dot{Q}_{wr}$) are the heat flows by convection and radiation from the wall surface to the ambience, α_w is the convective heat transfer coefficient (for the air), σ the Stefan-Boltzmann constant and ε the wall emissivity.

The total wall heat loss is obtained by taking integral the local wall heat loss along the kiln axis.
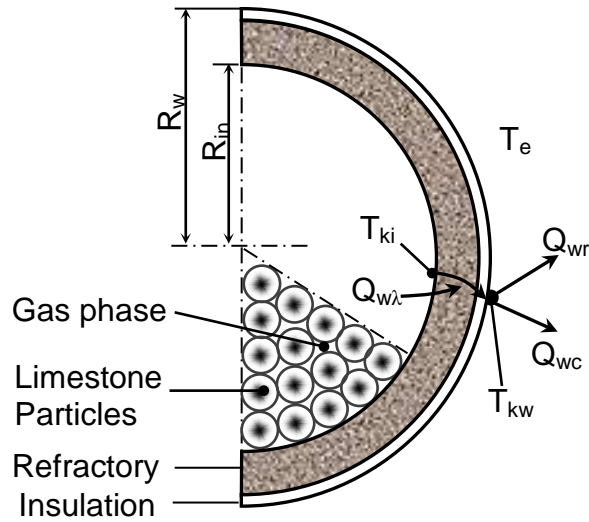
Figure 5-2: Heat transfer at the kiln wall of shaft kilns

b) Reaction zone

- **For the gas**

$$\frac{d}{dz}\left[\dot{M}_{g(z)} \cdot c_{pg} \cdot T_{g(z)}\right] = \frac{d\dot{M}_{f(z)}}{dz} \cdot h_u - \alpha_{(z)} \cdot A_F \cdot O \cdot (1-\psi) \cdot \left(T_g - T_{sw}\right) - \frac{d\dot{Q}_{w(z)}}{dz} \qquad (5\text{-}5)$$

- **For the solid**

$$\frac{d}{dz}\left[\dot{M}_{s(z)} \cdot c_{ps} \cdot T_{sw(z)}\right] = \alpha_{(z)} \cdot A_F \cdot O \cdot (1-\psi) \cdot \left(T_g - T_{sw}\right) - \frac{d\dot{M}_{CO2(z)}}{dz} \cdot \Delta h_{CO_2} \qquad (5\text{-}6)$$

In Eq. (5-5), the change of the gas enthalpy flow is equal to the local heat produced by the fuel combustion minus the heat transferred from the gas to the solid and the local wall heat loss. Here $\dot{M}_f$ means the mass flow of the fuel, h_u the calorific heating value of the fuel, α the convective heat transfer coefficient, T_{sw} the surface temperature of the solid particle.

In Eq. (5-6), the change of the solid enthalpy flow is equal to the heat transferred from the gas and the heat consumed by the decomposition. Here $\dot{M}_{CO_2}$ and Δh_{CO_2} are the mass flow and the specific reaction enthalpy with respect to decomposed CO_2. A remark from this equation is that the heat consumed by calcination is much higher than the solid enthalpy flow. Therefore, the change of the mean temperature of the solid is approximated by the change of the surface temperature. This surface temperature is used to calculate the heat transfer in this zone.

The kinetics of the combustion behavior and the flame length in shaft kilns is unknown since it is very complex to describe. It depends on the kind of fuel and the type of kiln. Therefore, the heat of the combustion in Eq. (5-5) is treated in a simplified way, in which the fuel combustion is described corresponding to a given fuel burning degree X_f.

$$\frac{d\dot{M}_{f(z)}}{dz} = \dot{M}_f \cdot \frac{dX_{f(z)}}{dz} \tag{5-7}$$

The burning degree X_f is approximated by a function with initial conditions $X_f = 0$ at the beginning of the flame (burner level, z_b) and $X_f = 1$ at the end of the flame (z_r), **Figure 5-3**. The function of X_f is given as:

$$X_{f(z)} = 1 - \exp(a \cdot (z_b - z)^b) \tag{5-8}$$

where a and b are factors used to adjust the flame length L_f ($L_f = z_b - z_r$), which depends on the kinds of fuel and kilns. If the $X_{f(zr)}$ is taken as 0.9999, the factor a is obtained from Eq.(5-8) in dependence on b and L_f as:

$$a = \frac{4\ln(10)}{(z_b - L_f)^b} \tag{5-9}$$

In Eq. (5-6), the mass flow of the CO_2 decomposed in the length dz is calculated as:

$$\frac{d\dot{M}_{CO2(z)}}{dz} = \frac{1}{w_s} \cdot \frac{d\dot{M}_{CO2}}{dt} \tag{5-10}$$

where w_s is the stone velocity and $d\dot{M}_{CO2}/dt$ is the mass flow of the CO_2 decomposed in the time dt, which is determined as before in chapter 3. The stone velocity w_s is calculated as:

$$w_s = \frac{\dot{M}_L}{\rho_L} \cdot \frac{1}{A_F} \tag{5-11}$$

with $\dot{M}_L$ and ρ_L are the flow and the density of the lime.
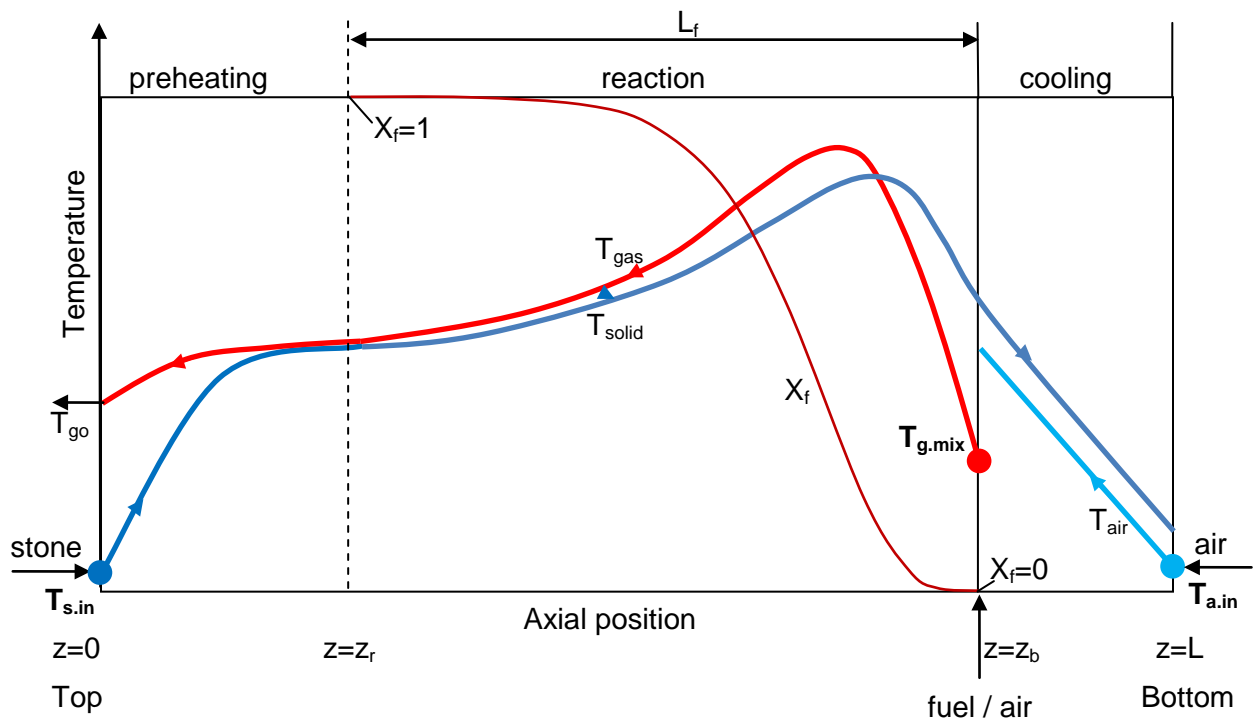
Figure 5-3: Temperature and fuel burning profiles in a normal shaft kiln

5.1.2 Mass balance equation

The mass flows of the gas and the solid in the preheating and the cooling zones are constant. However, in the reaction, due to the limestone decomposition, the mass flow of the gas and that of the solid change. The mass balance equations for the gas and the solid in the reaction zone are given as:

- **For the gas**

$$\dot{M}_{g(z)} = \dot{M}_f + \dot{M}_a + \dot{M}_{CO_2(z)} \tag{5-12}$$

The gas flow includes the flows of the fuel, the air and the CO_2 produced by the decomposition.

- **For the solid**

$$\dot{M}_{s(z)} = \dot{M}_{LS} - \dot{M}_{CO_2(z)} \tag{5-13}$$

The solid flow decreases since the CO_2 is dissociated from the solid to the gas.

5.1.3 Boundary value problem and numerical solution

The system of ordinary differential equations describing the energy conservations needs to be solved numerically to get temperature profiles. Initial values for solving these equations are given as:

$$T_s\,(z=0) = T_{s.in} \qquad\qquad\qquad\qquad\qquad (5\text{-}14)$$

$$T_g\,(z=L) = T_{a.in} \qquad\qquad\qquad\qquad\qquad (5\text{-}15)$$

Here the initial values are given at the kiln top (z=0) with the stone inlet temperature ($T_{s.in}$) and at the kiln bottom (z=L) with the air inlet temperature ($T_{a.in}$), Figure 5-3. These initial values are at two points of the solution domain, thus numerical solutions face typical problems. These problems are so called boundary value problems. The boundary value problem is considered as one of the most difficult problems for simulations of lime burning in shaft kilns, which have also been reported by other authors [45 - 50].

To be more convenient and effective for developing numerical solutions, the preheating and the reaction zones are handled together while the cooling zone is calculated separately. For calculating the preheating and the reaction zones, the initial value of the gas temperature ($T_{a.in}$) in Eq.(5-15) is replaced by $T_{g.mix}$; the temperature of the mixture of fuel / secondary air and cooling air at the burner level (z_b).

$$T_g\,(z=z_b) = T_{g.mix} \qqquad\qquad\qquad\qquad\qquad (5\text{-}16)$$

In general, the Runge-Kutta method is employed to solve differential equations in which the initial values are normally given at one point of the solution domain. However, due to the boundary value problem it is not possible to apply in this case. Therefore, numerical solutions can be employed by incorporating the shooting method with the help of the Runge-Kutta method. Nevertheless, the equations describe the complex of heat and mass transfer and chemical reactions while all of them are coupled so that the solution must be good enough to minimize errors of every single integration step in the solution domain. In this study, some commercial solvers, for example, bvp4c (a MATLAB code), which is able to solve the boundary value problem, are also used.

The shooting method is a numerical solution for solving the boundary value problem by reducing it to the solution of an initial value problem. The solution is based on a shooting progress where the program is employed to target an objective from a given position in the solution domain. For example, to calculate the gas temperature in the preheating and reaction zones where the gas temperature $T_{g.mix}$ is known at the end of the reaction zone (burner level), different values of T_{go} at the kiln top must be given as starting points, then the program will

try to target the initial value $T_{g..mix}$. After succeeding to reach the $T_{g.mix}$, a final value of the T_{go} is calculated and a gas temperature profile is determined as well.

As mentioned before, the commercial solver bvp4c is also used for developing the numerical solution. This is a finite difference code, which implements the 3-stage Lobatto IIIa formula. The code provides continuous solution with fourth-order accuracy uniformly in the interval of integration. The solution is done in the solution domain with two point boundary conditions where mesh selection and error control are based on the residual of the continuous solution. Error! Reference source not found. show flowcharts of the numerical solutions developed by using the commercial solver bvp4c.

To understand the behavior of the differential equations, sensitivity analysis of the numerical solution was done by using the two above methods. The results obtained by both numerical methods are similar. However, sometime the numerical solutions become sensitive while verifying inputs of the equations. The following variables have been reported with significant effects on the sensitivity of the solutions.

- The starting / initial values: T_{go}, $T_{g.mix}$, $T_{s.in}$, $T_{a.in}$
- The operating parameters: Energy input, kiln throughput, particle size etc.
- The kiln dimension: Height, diameter

It is difficult to conclude the reasons that cause the solution to become sensitive. The first reason is the boundary value problem. The second reason is the complex coupling of the heat and mass transfer and chemical reactions in the differential equations. From a mathematical point of view, the third reason is that the systems of differential equations have 'stiff' equations or non-unique equations, which typically cause instability for numerical solutions.

In this dissertation, to make the numerical solution methods easier, the following assumptions are made.

- The conditions at every cross-section along the kiln axis are homogeneous
- All stone particles are considered as spheres with the same size
- The radiative heat transfer is neglected
- The combustion of the fuel is treated in a simplified way with a given burning profile
- The gas is considered as an ideal mixture containing N_2, O_2, CO_2 and H_2O

```
          ┌──────────────┐
          │    start     │
          └──────────────┘
                  │
                  ▼
        ╱────────────────────╱
       ╱  Input parameters  ╱
      ╱────────────────────╱
                  │
                  ▼
      ╱──────────────────────────╱
     ╱  Assume gas temp., at the ╱
    ╱   burner level T_{g.mix}  ╱
   ╱──────────────────────────╱
                  │
                  ▼
        ┌──────────────────────────────┐
        │ Calculation preheating and   │
        │        reaction zone         │
        └──────────────────────────────┘
                  │
                  ▼
        ┌──────────────────────────────┐
        │   Calculation cooling zone   │
        └──────────────────────────────┘
                  │
                  ▼
  ┌────────────────┐        ◇
  │ Modify T_{g.mix} │   N  ◇   ◇
  └────────────────┘ ◇ Energy balances ?
                        ◇   ◇
                          ◇
                          │ Y
                          ▼
                ╱──────────────────╱
               ╱  Output results  ╱
              ╱──────────────────╱
                          │
                          ▼
                  ┌──────────────┐
                  │     End      │
                  └──────────────┘
```
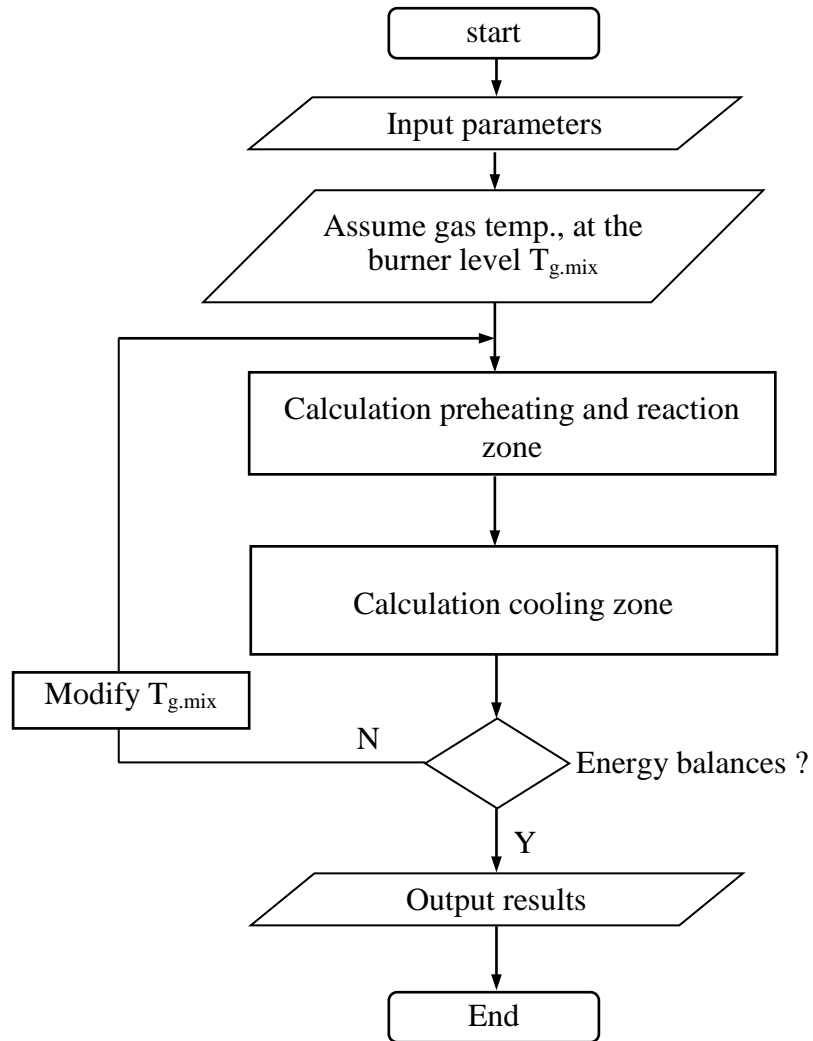
Figure 5-4: Numerical solution with using commercial solver bvp4c in MATLAB

5.2 Results of simulation

5.2.1 Basic input data

Table 5-1 describes general input variables for simulations. The kiln has a total solid bed height of 15 m, in which the height of the cooling zone is 4 m. The fuel used is natural gas with the specific energy consumption E=3.8 MJ/kg$_{lime}$ and the excess air number λ_f=1.2. The specific kiln throughput ($\dot{m}_{lime}$) is 23.3 t/d/m^2. The mean particle size (d) is taken as 70 mm and the void fraction of the bed is assumed as a constant value ψ=0.38. The limestone contains 96 % in mass of the calcium carbonate and the rest is inert.

Table 5-1 Basic data for simulation of the normal shaft kiln

	Input variables	**Units**	**Value**
	Total length of solid bed	m	15
Kiln dimension	Length of preheating and reaction zone	m	11
	Length of cooling zone	m	4
Combustion process	Heat consumption (natural gas fuel)	MJ/kg$_{lime}$	3.8
		kcal/kg$_{lime}$	908
	Excess air number	-	1.2
Kiln operating process	Limestone input flow	t/d/m^2	40.2
	Lime output flow	t/d/m^2	23.3
	Cooling (primary) air flow	m$^3_{air}$/kg$_{lime}$	0.70
	Secondary air flow	m$^3_{air}$/kg$_{lime}$	0.63
	Fuel flow	m^3/kg$_{lime}$	0.1
	Air feed temperature	^{o}C	20
	Limestone feed temperature	^{o}C	20
Lime and limestone	Mean particle size	mm	70
	Average void fraction of solid bed	-	0.38
	CaCO$_3$ content in limestone	% mas	96

5.2.2 Principal temperature and conversion profile

Figure 5-5 shows the principal temperature and the mass fraction profiles in the normal shaft kiln with basic data given in Table 5-1. The mass fraction is defined as the mass ratios of the gas or the solid to the lime, kg/kg_{lime}. Figure 5-5 is illustrated in the horizontal direction, which is transferred corresponding to the schematic diagram of the normal shaft kiln shown before in Figure 1-1. The coordinate 0 m represents the top of the kiln. Initially, the limestone is charged into the kiln from the top at the ambient temperature of 20 °C. Then it is preheated by the hot gas in the preheating zone and its temperature increases rapidly until the reaction temperature (820°C) at about 3.1 m. At this position, the limestone decomposition begins and its mass fraction starts decreasing. The end of the preheating zone indicates the beginning of the reaction zone. In the reaction zone, both the solid surface (T_{sw}) and core (T_{sf}) temperatures are depicted together. At the end of this zone (11 m), the fuel and the secondary air are injected at the ambient temperature, and then they mix with the hot air coming from the cooling zone. The gas mixture has an average temperature of about 700 °C, which is lower than that of the solid. When the gas temperature is lower than that of the solid, the decomposition process is not possible since the gas cools the solid. The combustion is assumed to start immediately from the end of the reaction zone, thus the gas temperature increases sharply and it exceeds the solid temperature at about 10.6 m. As a result, the gas, on the way to the kiln top, transfers heat to the solid and the decomposition process is possible. The calcination zone lies from 3.1 m to 10.6 m. The solid, on the way to the kiln bottom, gets heat from the combustion gas; therefore, its temperature keeps increasing in the reaction zone until it reaches a maximum value of about 1432 °C at 10.6 m. The solid leaves the reaction zone with a temperature of about 1080 °C and then enters the cooling zone, where it is cooled down by the cooling air until it reaches discharge temperature. In the cooling zone, the heat capacity ratio of the lime to the air is assumed as one, thus both temperature profiles are linear.

59
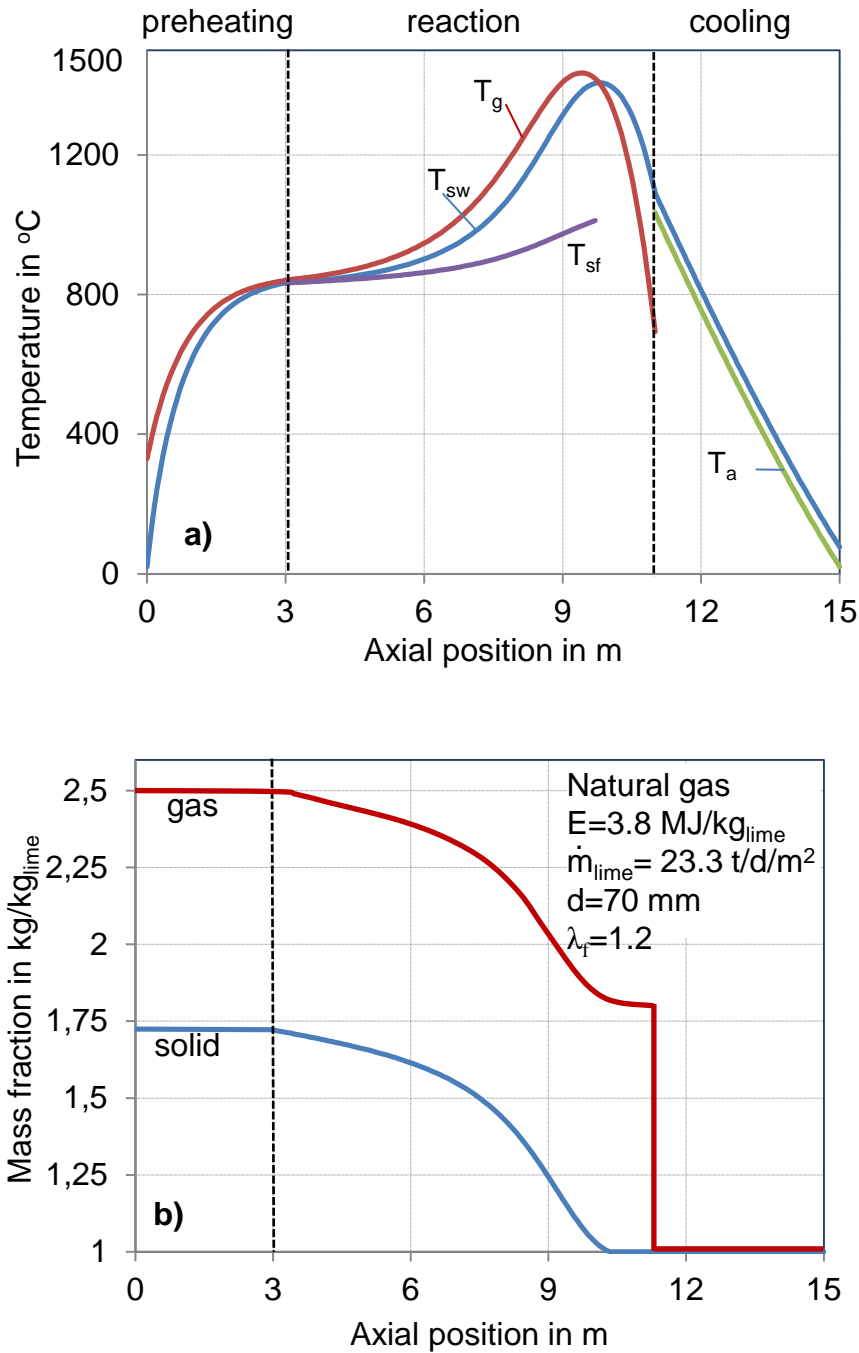
Figure 5-5: Principal temperature and mass fraction profiles in the normal shaft kilns

In addition, other characteristic values of this simulation are summarized in **Table 5-2**. The temperature of the flue gas is 308 $^{\circ}$C and that of the lime discharge is 80 $^{\circ}$C. A remark here is that these temperatures are considered as mean values obtained directly at the top / bottom of the solid bed. Measured values are often lower since the gas at the top is mixed with false air and the lime temperature is detected only after discharge. The maximum temperature of the gas is 1468 °C and that of the solid is 1432 °C. The heat loss through the kiln wall is about 6.2 % of the total energy input and the pressure drop is 202 mbar.

Table 5-2 Simulation results of the normal shaft kiln

Outputs	Unit	Value
Flue gas temperature	^{o}C	308
Lime discharge temperature	^{o}C	80
Calcination starts at	m	3.1
Calcination length	m	7.5
Lime conversion	%	100
Maximum gas temperature	^{o}C	1468
Maximum solid temperature	^{o}C	1432
Heat loss by kiln wall	%	6.2
Total pressure drop	mbar	202

5.2.3 Pressure drop profile

Figure 5-6 reveals a typical pressure drop profile along the normal shaft kiln. Simulations were done with the mean particle size of 70 mm, the average kiln void fraction of 0.38 and the gas property depending on the gas temperature simulated as before.
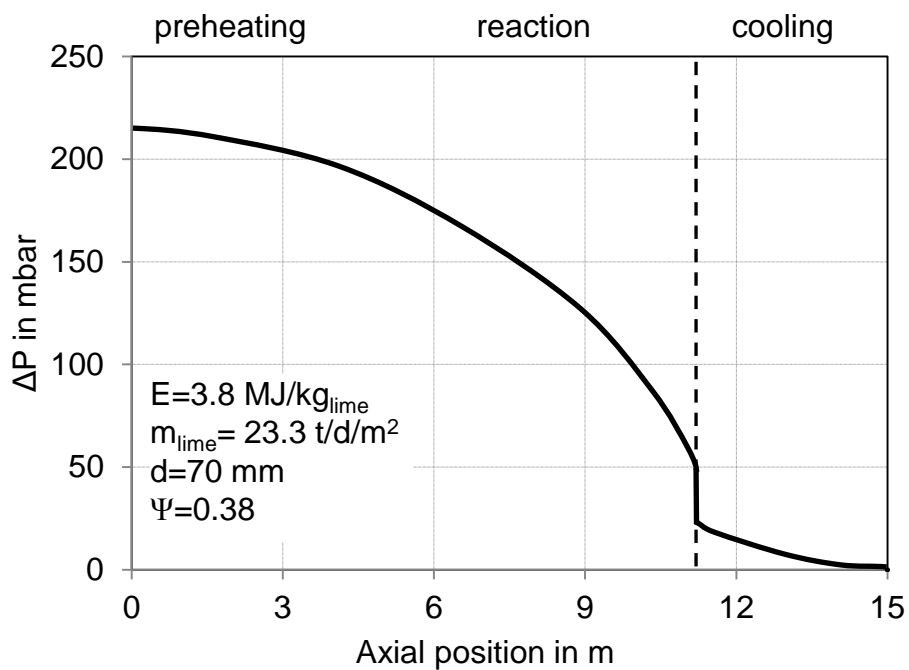

Figure 5-6: Principal pressure drop profile along the normal shaft kilns

As seen from Table 5-2, the total pressure drop of the kiln is about 202 mbar, however the pressure drop is different in every zone. For instance, in the cooling zone it is relatively small due to low gas flow (only cooling air). In the burning and preheating zones, the pressure drop is much higher due to two reasons: a) the gas flow is much higher because the fuel, the secondary air and the decomposed CO_2 are all added in these zones, b) the kiln temperature is also higher.

5.3   Influencing parameters

5.3.1   Influence of energy input

Figure 5-7 shows the temperature and the conversion (solid mass fraction) profiles for different energy inputs. As an example, the energy input was varied in the range from 3.7 to 3.9 MJ/kg$_{lime}$. Other input parameters for simulations were kept the same as given before in Table 5-1.

The higher the energy input, the more fuel is introduced, thus the more heat is generated by the combustion. This causes an increase of the gas and the solid temperatures. As a result, the limestone decomposes faster and requires a shorter calcination zone. A higher energy results in a shorter preheating zone and an earlier beginning of the calcination process.

In addition, **Table 5-3** summarizes the characteristic values of simulations. It can be seen that an increase of the energy results in an increase of the flue gas and the lime discharge temperatures. However, the flue gas temperature changes in a stronger way. The maximum temperatures of the gas and the solid also increase significantly with the increase of the energy. A decrease of the energy extends the length of the calcination zone since the temperature decreases. For instance, with a decrease of energy until 3.7 MJ/kg$_{lime}$, the calcination zone becomes so long, thus a complete calcination is not possible. Furthermore, the more fuel is injected, the more air is required (higher gas flow), which results in a higher pressure drop.
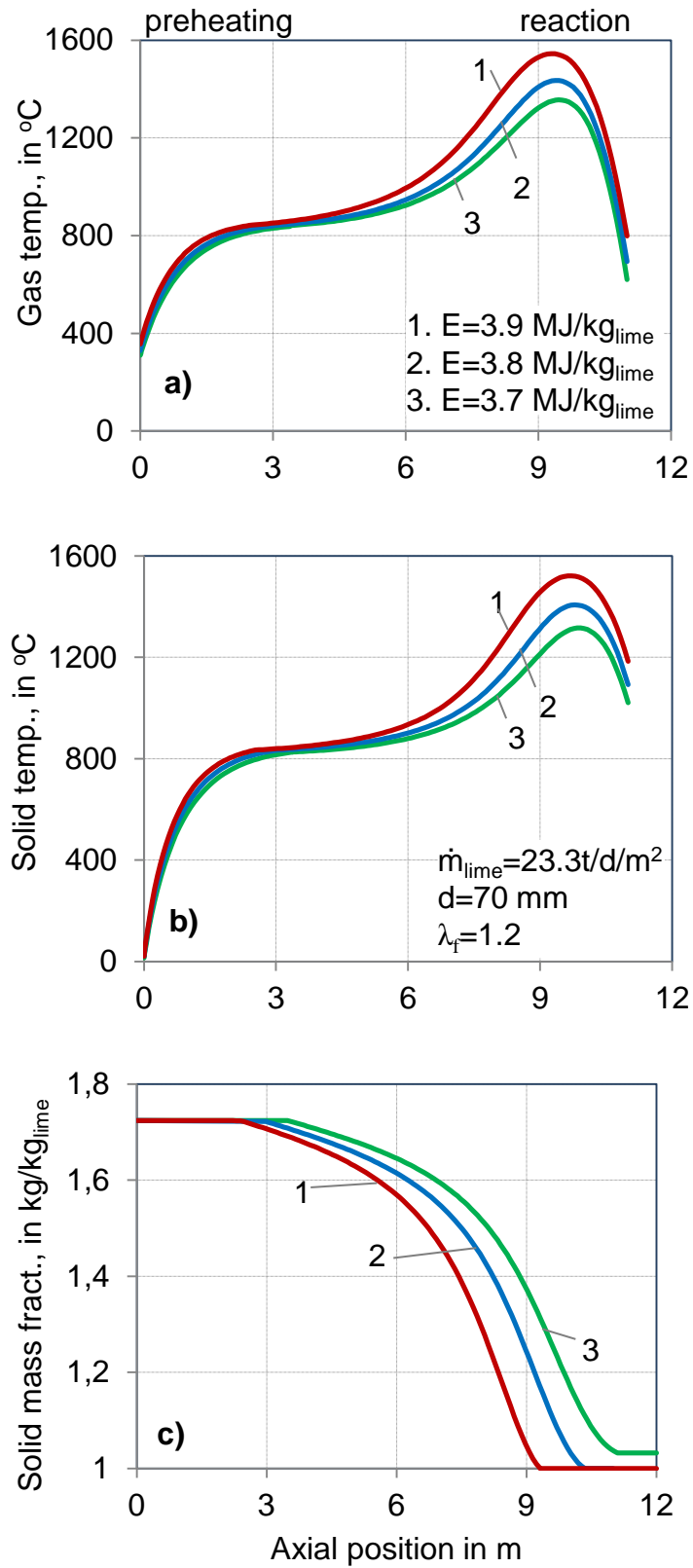
Figure 5-7: Influence of energy input on the temperature and the conversion profiles

Table 5-3 Influence of energy input

Energy input	MJ/kg	3.7	3.8	3.9
Flue gas temperature	^{o}C	301	308	338
Lime discharge temp.	^{o}C	76	80	98
Calcination start at	m	3.4	3.1	2.2
Calcination length	m	7.6	7.5	6.9
Lime conversion	%	98.8	100	100
Max. gas temperature	^{o}C	1398	1468	1565
Max. solid temperature	^{o}C	1352	1432	1519
Total pressure drop	mbar	180	202	236

5.3.2   Influence of lime throughput

Figure 5-8 and **Table 5-4** show the simulations for different kiln throughputs in the same manner as before. As an example, the kiln throughput was changed in the range of 23.3 ± 2 $t/d/m^2$. Other input parameters such as the energy were kept the same as before.

A lower kiln throughput leads to a longer residence time of the limestone. Consequently, the limestone gets more time to decompose, thus the calcination zone becomes shorter. The kiln temperature decreases with the increase of the throughput. Therefore, in order to get the same conversion degree (e.g., complete calcination) the length of the calcination zone must be extended. If this length is not sufficient, a complete calcination cannot be achieved. For instance, in this simulation, an incomplete calcination is observed with 25 $t/d/m^2$ throughput.

Table 5-4 Influence of lime throughput

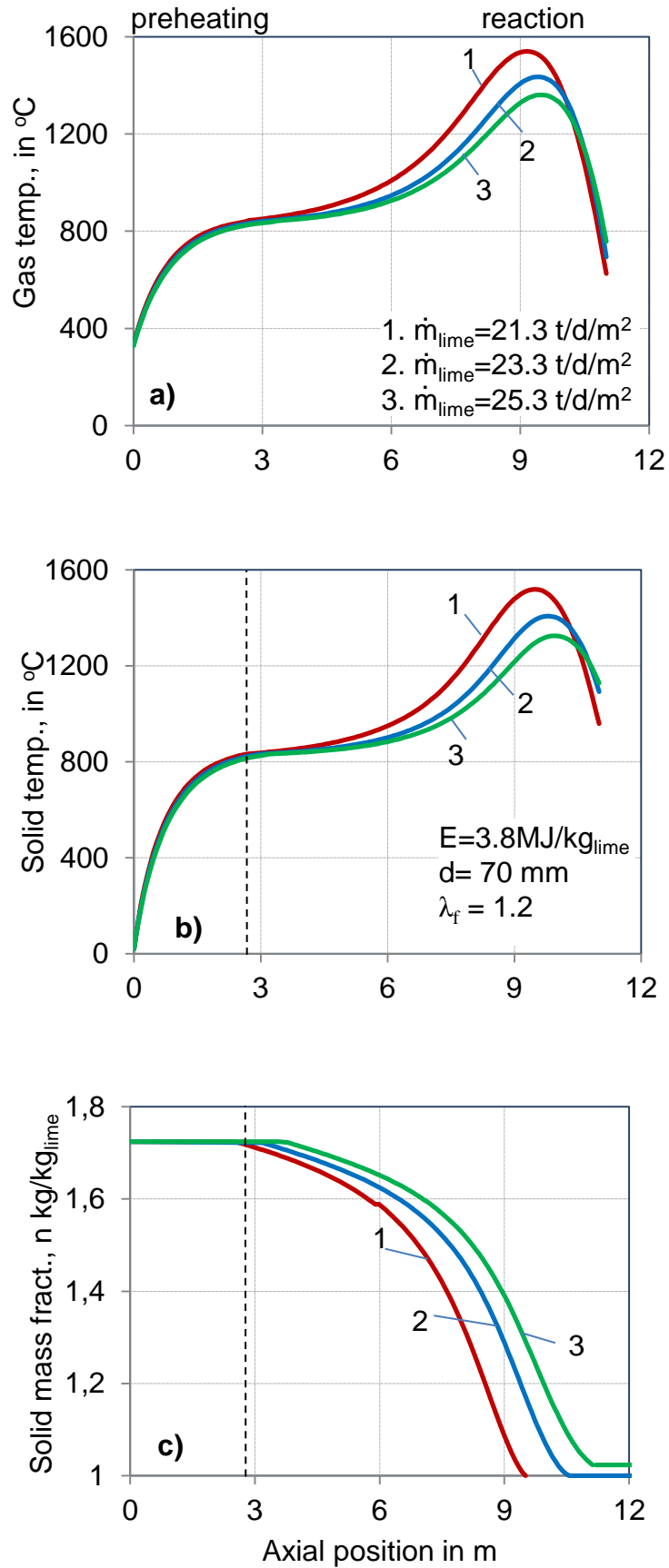| Lime throughput	$t/d/m^2$	21.3	23.3	25.3
Flue gas temperature	^{o}C	309	308	315
Lime discharge temp.	^{o}C	77	80	88
Calcination starts at	m	2.5	3.1	3.2
Calcination length	m	6.7	7.5	7.8
Lime conversion	%	100	100	98.6
Max. gas temperature	^{o}C	1556	1468	1421
Max. solid temperature	^{o}C	1526	1432	1325
Total pressure drop	mbar	192	202	238

Figure 5-8: Influence of kiln throughput on the temperature and the conversion profiles

The incomplete calcination causes the increases of the flue gas and the lime discharge temperature, Table 5-4. The reason is that a small amount of heat produced by the combustion, which is not consumed by the calcination, is transferred to the flue gas and the lime discharge. Additionally, a higher kiln throughput leads to a higher gas flow, thus it results in a higher pressure drop.

A remark is observed that the kiln throughput affects the maximum temperature of the solid bed. Therefore, it has an indirect effect on the lime reactivity. The lower the kiln throughput, the higher the maximum temperature is and the lower the expected reactivity of lime is.

5.3.3 Influence of particle size

Figure 5-9 and **Table 5-5** show the simulation results for different particle sizes. As mentioned before, here the particle size represents the mean value of a distribution. Simulations were done for three sizes of 65, 70 and 75 mm while other inputs were kept the same as before.

A smaller particle decomposes faster and requires a shorter calcination zone. An increase of the particle size requires an extension of the calcination zone. A complete calcination cannot be obtained with large particle sizes if the length for calcination is not sufficient. For instance, in this simulation, an incomplete calcination is observed with the size of 75 mm. The larger the stone size, the longer the preheating zone is required. In addition, the kiln maximum temperatures and the pressure drop increase considerably with the decrease of the particle size, Table 5-5.

Table 5-5 Influence of particle size

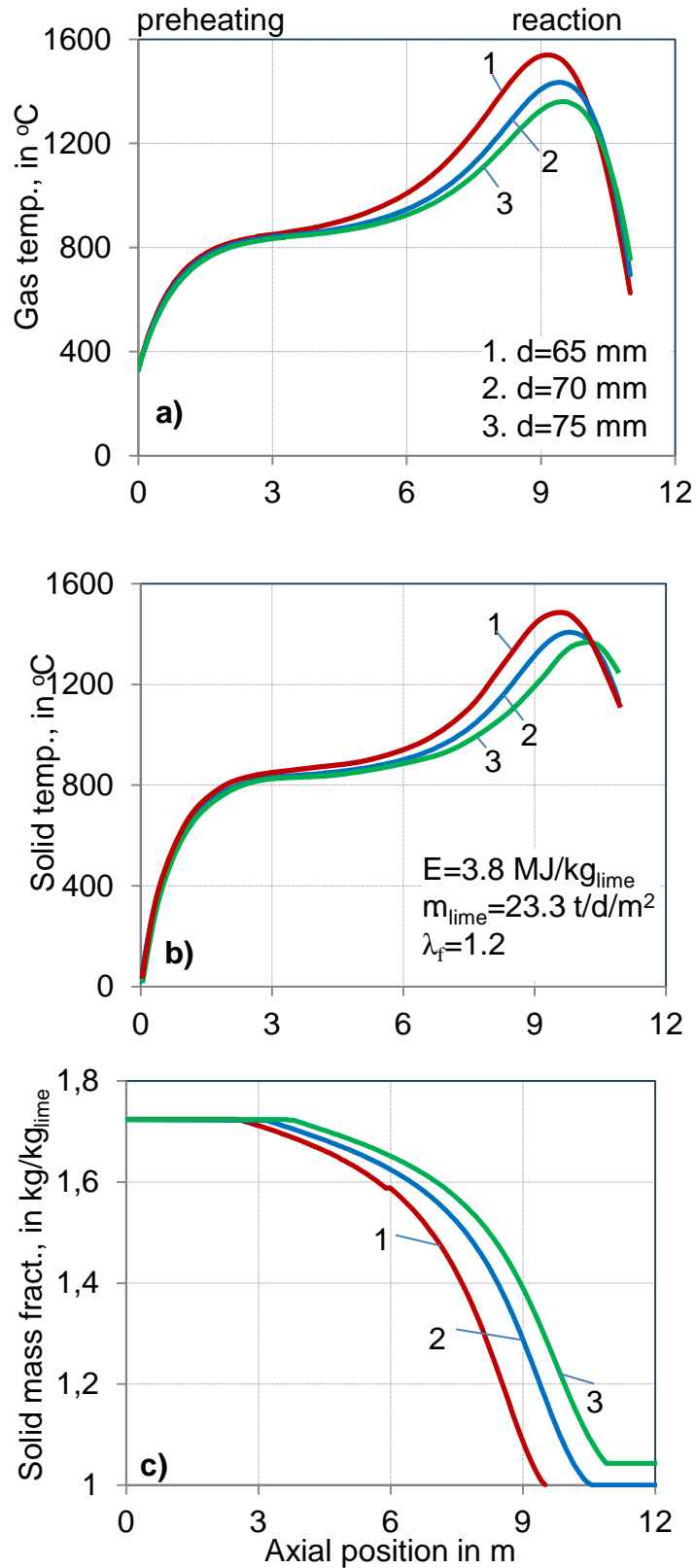| Particle size	mm	65	70	75
Flue gas temperature	^{o}C	310	308	320
Lime discharge temp.	^{o}C	78	80	83
Calcination starts at	m	2.8	3.1	3.2
Calcination length	m	7.1	7.5	7.8
Lime conversion	%	100	100	98.2
Max. gas temperature	^{o}C	1536	1468	1421
Max. solid temperature	^{o}C	1503	1432	1328
Total pressure drop	mbar	220	202	185

Figure 5-9: Influence of particle size on the temperature and the conversion profiles

5.3.4 Influence of limestone origin

To see how the material properties influence the process, simulations were done for three different kinds of limestones, which have different properties as shown before in Table 3-2. The simulation results are shown in **Figure 5-10** and **Table 5-6**.

The limestone (Ge.1) with the highest reaction coefficient decomposes with the highest calcination rate and requires the shortest calcination zone. In contrast, the limestone (Ge.3) with the smallest reaction coefficient decomposes with the lowest calcination rate and needs the longest calcination zone. It is remarkable that with the same operating conditions, the limestone Ge.3 does not completely decompose. Therefore, to get complete calcination for this limestone, higher energy input or lower kiln throughput are required.

Table 5-6 Influence of limestone property

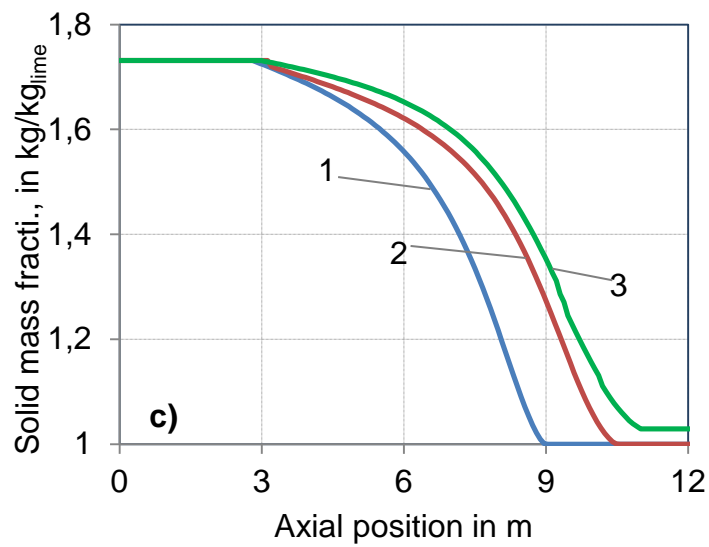| Limestone	-	Ge.1	Ge.2	Ge.3
Flue gas temperature	^{o}C	308	308	319
Lime discharge temp.	^{o}C	80	80	86
Calcination starts at	m	3.1	3.1	3.1
Calcination length	m	5.8	7.5	8.0
Lime conversion	%	100	100	98.3
Max. gas temperature	^{o}C	1470	1459	1446
Max. solid temperature	^{o}C	1451	1432	1416
Total pressure drop	mbar	206	202	196
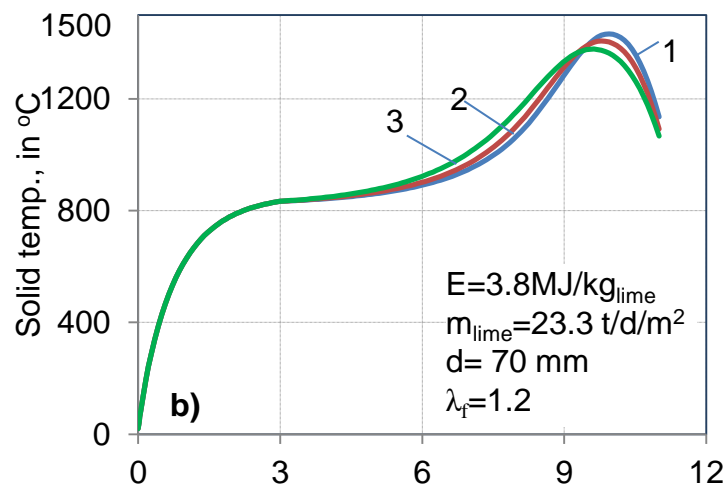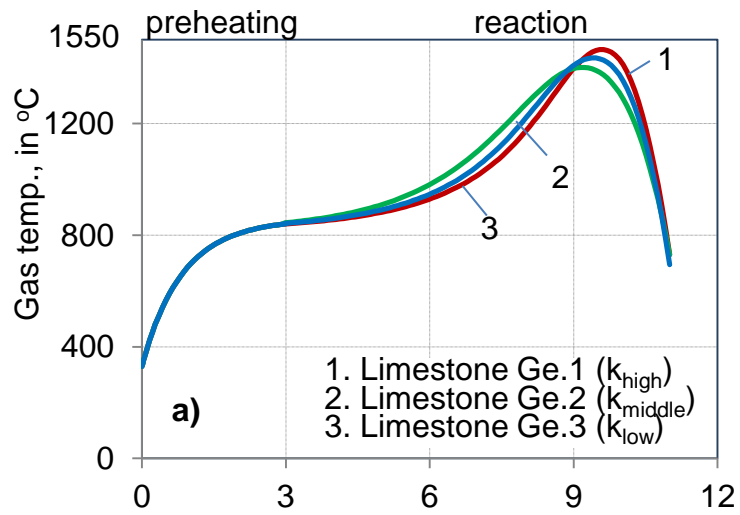
Figure 5-10: Influence of limestone origin on the temperature and the conversion profiles

5.3.5 Influence of excess air number

Figure 5-11 and **Table 5-7** show the simulation results for different excess air numbers varied in the range from 1.2 to 1.4. A smaller excess air number causes a higher kiln temperature, leading to a shorter calcination zone. An increase of the excess air number results in an increase of the calcination zone since the kiln temperature decreases. With an increase of the excess air number up to 1.4, the temperature becomes so low that the length of calcination is not sufficient to obtain a complete calcination. Additionally, an increase of the excess air number results in a higher gas flow, thus it causes a greater pressure drop.

Table 5-7 Influence of excess air number

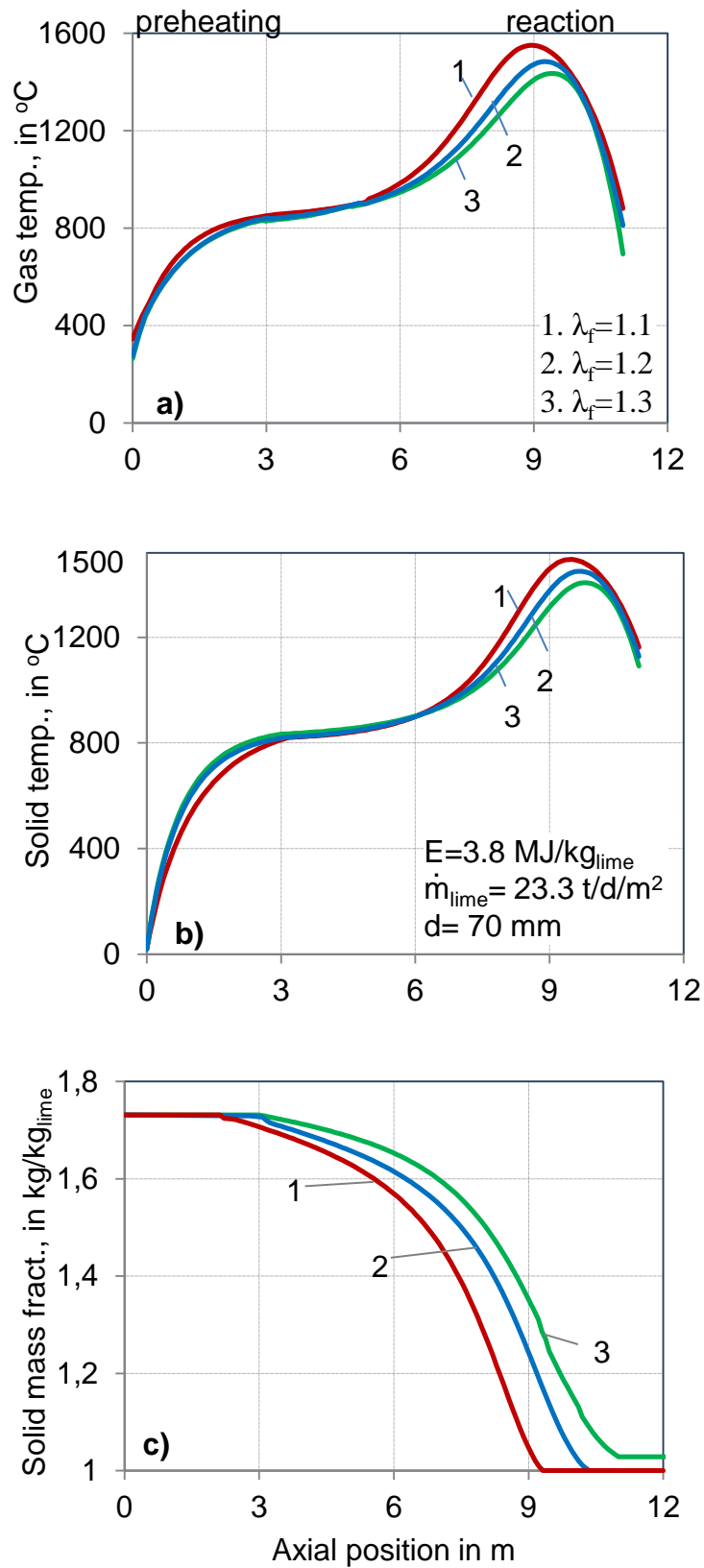| Excess air number	-	1.1	1.2	1.3
Flue gas temperature	^{o}C	324	308	298
Lime discharge temp.	^{o}C	83	80	76
Calcination starts at	m	3.3	3.1	2.8
Calcination length	m	7.7	7.5	8.2
Lime conversion	%	100	100	97.8
Max. gas temperature	^{o}C	1497	1468	1433
Max. solid temperature	^{o}C	1466	1432	1408
Total pressure drop	mbar	196	202	218

Figure 5-11: Influence of excess air number on the temperature and the conversion profiles

5.3.6 Influence of fuel combustion behavior

As mentioned before, it is very complex to describe the kinetics of the combustion process in shaft kilns. The complex combustion behavior of the fuel is treated in a simplified way with respect to the length of the flame. Therefore, the influence of the fuel combustion behavior on the process will be represented by the influence of the flame length.

Table 5-8 Influence of fuel combustion behavior

Flame length	-	short (4.5 m)	long (6.0 m)
Flue gas temperature	^{o}C	315	309
Lime discharge temp.	^{o}C	82	80
Calcination starts at	m	3.4	2.9
Calcination length	%	7.3	8.0
Lime conversion	^{o}C	99.1	100
Max. gas temperature	^{o}C	1480	1363
Max. solid temperature	mbar	1441	1338
Total pressure drop	^{o}C	204	195

As an example, **Figure 5-12** shows the influences of two given flame lengths on the gas and the solid temperatures. A long flame shifts the peaks of temperatures upward and causes the calcination process to begin earlier. It is remarkable that a short flame causes a significant increase of the peaks of temperature. For instance, in this case, the peak of temperature of the short flame is almost 110°C higher than that of the long flame. Additionally, when the flame is short, the length for calcination becomes shorter as well, **Table 5-8**. A complete calcination cannot be obtained if this length is not sufficient. For instance, with 4.5 m flame length, an incomplete calcination is observed.
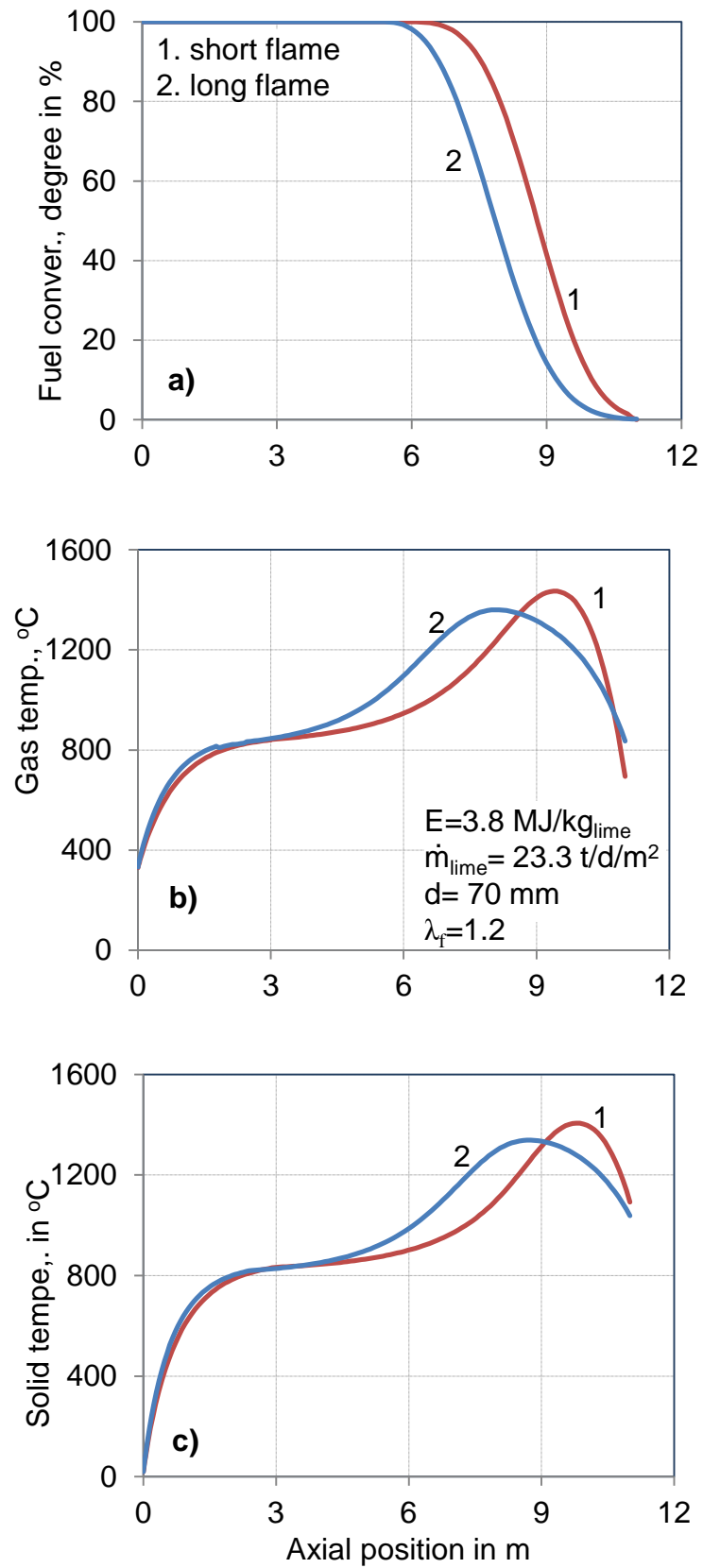
Figure 5-12: Influences of fuel combustion behavior on the temperature profiles

6 Simulation of lime calcination in PFR kiln

6.1 Simplification of PFR kiln for modeling

The PFR kiln consists of two shafts connected by a channel as shown before in Figure 1-3. Each shaft is subjected to two distinct modes of operations, burning and non-burning mode, in which the periodic time for each mode is about 8 – 15 min. On the one hand, for the process modeling, it is very difficult to describe mathematically the periodic transient behavior. On the other hand, it gives no more information to the expected results as mentioned in the introduction. Therefore, if the reversal time between two shafts can be assumed extremely short, then the non-burning shaft can be simplified as pipes located inside the burning shaft. These pipes act as heat exchangers for the heat transfer process between the gas (from non-burning shaft) and the solid. Two shafts can be simplified as one shaft, which is shown in **Figure 6-1**. The new shaft has three typical operating zones as before with the preheating, the burning and the cooling zones.

In this dissertation, the mathematical model will be developed with respect to the simplified shaft. Therefore, the mean values of the periodic fluctuations are considered.

6.2 Mathematical model

6.2.1 Energy balance equation

a) Preheating and cooling zone

In the cooling zone, the energy balance equations are described by the same way as given before, Eq(5-1)-(5-2).

In the preheating zone, there are two heat transfer processes: a) from the flue gas (fg) to the solid, and b) from the solid to the combustion air (a). The energy balance equations for the combustion air and the flue gas are also described by the same way as before, Eq(5-1). The solid involves in two heat transfer processes, thus its energy balance equation is described as:

$$\dot{M}_s \cdot c_{ps} \cdot \frac{dT_{s(z)}}{dz} = \alpha_{\kappa.fg(z)} \cdot A_F \cdot O \cdot (1-\psi) \cdot (T_{fg} - T_s) - \alpha_{\kappa.a(z)} \cdot A_F \cdot O \cdot (1-\psi) \cdot (T_s - T_a) \qquad (6\text{-}1)$$

The change of the solid enthalpy flow is equal to the heat transferred from the flue gas to the solid and the heat transferred from the solid to the combustion air. Here $\alpha_{\kappa.fg}$ and $\alpha_{\kappa.a}$ are the overall heat transfer coefficient with respect to the flue gas and the combustion air.
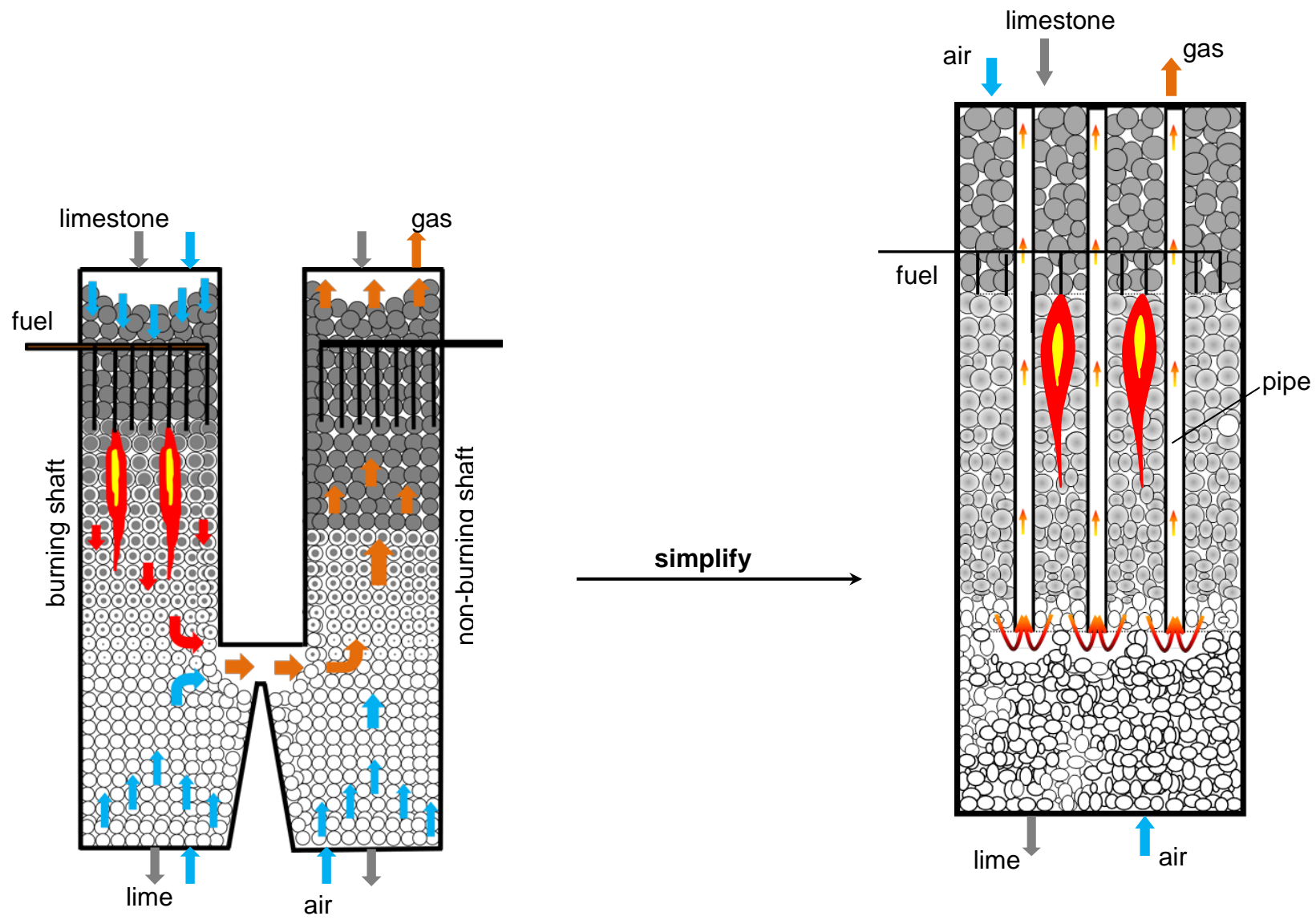
Figure 6-1: Simplification of the PFR shaft kilns

flue gas$_{out}$

$\dot{M}_{fg} \cdot c_{pfg} \cdot (T_{fg(z)} - T_{fgref})$

solid$_{in}$

$\dot{M}_{s(z)} \cdot c_{ps} \cdot (T_{s(z)} - T_{s,ref})$

gas$_{in}$

$\dot{M}_{g(z)} \cdot c_{pg} \cdot (T_{g(z)} - T_{g,ref})$

dz

$\dot{M}_{s(z+dz)} \cdot c_{ps} \cdot (T_{s(z+dz)} - T_{s,ref})$

solid$_{out}$

$\dot{M}_{g(z+dz)} \cdot c_{pg} \cdot (T_{g(z+dz)} - T_{g,ref})$

gas$_{out}$

$\dot{M}_{fg} \cdot c_{pfg} \cdot (T_{fg(z+dz)} - T_{fgref})$

flue gas$_{in}$
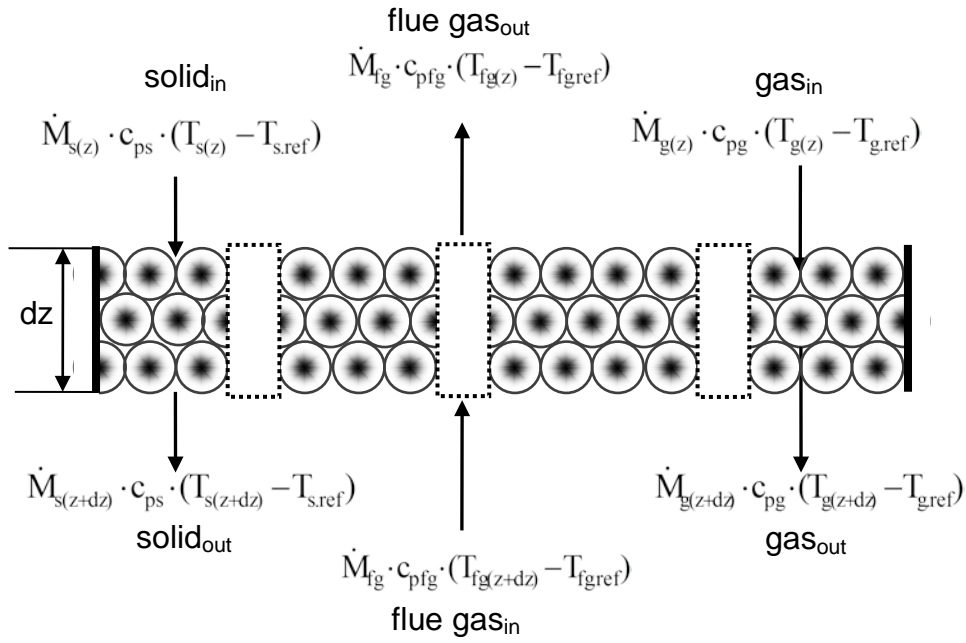
Figure 6-2: Scheme of a simplified PFR kiln with section of length dz

a) Reaction zone

- **For the gas**

$$\frac{d}{dz}\left[\dot{M}_{g(z)} \cdot c_{pg} \cdot T_{g(z)} \right] = \frac{d\dot{M}_{f(z)}}{dz} \cdot h_u - \alpha_{(z)} \cdot A_F \cdot O \cdot (1-\psi) \cdot (T_g - T_{sw}) - \frac{d\dot{Q}_{w(z)}}{dz} \qquad (6\text{-}2)$$

The energy balance equation for the gas in the reaction zone is described by the same way as given before, Eq.(5-5).

- **For the solid**

$$\frac{d}{dz}\left[\dot{M}_{s(z)} \cdot c_{ps} \cdot T_{s(z)} \right] = \alpha_{(z)} \cdot A_F \cdot O \cdot (1-\psi) \cdot (T_g - T_{sw}) + \alpha_{fg(z)} \cdot A_F \cdot O \cdot (1-\psi) \cdot (T_{fg} - T_{sw}) \qquad (6\text{-}3)$$

$$- \frac{d\dot{M}_{CO2(z)}}{dz} \cdot \Delta h_{CO2}$$

The change of the solid enthalpy flow is equal to the heat transferred between the combustion gas and the solid and the heat transferred between the flue gas and the solid.

- **For the flue gas**

$$\frac{d}{dz}\left[\dot{M}_{fg} \cdot c_{pfg} \cdot T_{fg(z)}\right] = \alpha_{fg(z)} \cdot A_F \cdot O \cdot (1 - \psi) \cdot (T_{fg} - T_{sw}) \tag{6-4}$$

The change of the enthalpy flow of the flue gas is equal to heat transferred between the flue gas and the solid.

6.2.2 Mass balance equation

Similar to the normal shaft kiln, the mass balance equations are described for the reaction zone as a representative case since the mass flows of the gas and the solid change in this zone due to the limestone decomposition.

- **For the gas (burning shaft)**

$$\dot{M}_{g(z)} = \dot{M}_f + \dot{M}_{af} + \dot{M}_{aT} + \dot{M}_{CO_2(z)} \tag{6-5}$$

The gas flow includes the fuel flow, the combustion air flow $\dot{M}_{af}$, the transport air flow $\dot{M}_{aT}$ (for solid fuel) and the decomposed CO_2 flow. The gas flow changes due to the CO_2 flow produced by the limestone decomposition.

- **For the solid**

$$\dot{M}_{s(z)} = \dot{M}_{LS} - \dot{M}_{CO_2(z)} \tag{6-6}$$

The mass balance equation for the solid is given as before in Eq.(5-13).

- **For the flue gas (non-burning shaft)**

$$\dot{M}_{fg} = \dot{M}_g + \dot{M}_{ac} + \dot{M}_{aL} \tag{6-7}$$

The flue gas flow is constant along the kiln. It includes the total gas flow from the burning shaft $\dot{M}_g$, the total cooling air flow $\dot{M}_{ac}$ and the lance cooling air flow $\dot{M}_{aL}$.

6.2.3 Boundary value problem and numerical solution

Similar to the normal shaft kilns, the initial values for solving the system of ordinary differential equations are given with the stone inlet temperature $T_{s.in}$ and the combustion inlet air temperature $T_{af.in}$ at the kiln top (z=0) and with the cooling air inlet temperature $T_{ac.in}$ at the kiln bottom (z=L), **Figure 6-3**.

$$T_g (z=0) = T_{af.in} \tag{6-8}$$

$$T_s (z=0) = T_{s.in} \tag{6-9}$$

$$T_{fg} (z=L) = T_{ac.in} \tag{6-10}$$

In this case, numerical solutions face again the boundary value problems. As mentioned before, to be easier for numerical solutions, the preheating and reaction zones are handled together while the cooling zone is calculated separately. With calculating the preheating and the reaction zones, the initial value of the gas temperature is given by $T_{g.mix}$, which is the temperature of the gas mixture at the crossover-channel ($z_{channel}$).

$$T_{fg} (z=z_{channel}) = T_{g.mix} \tag{6-11}$$

The temperature at the crossover-channel is measured and it varies often in the range of 950 – 1050 ^{o}C.

Numerical solutions were developed by using the same ways, the shooting method and the commercial solver bvp4c, as before with the normal shaft kilns. As an example, **Figure 6-4** shows a flowchart of the numerical solution developed by using the commercial solver bvp4c.
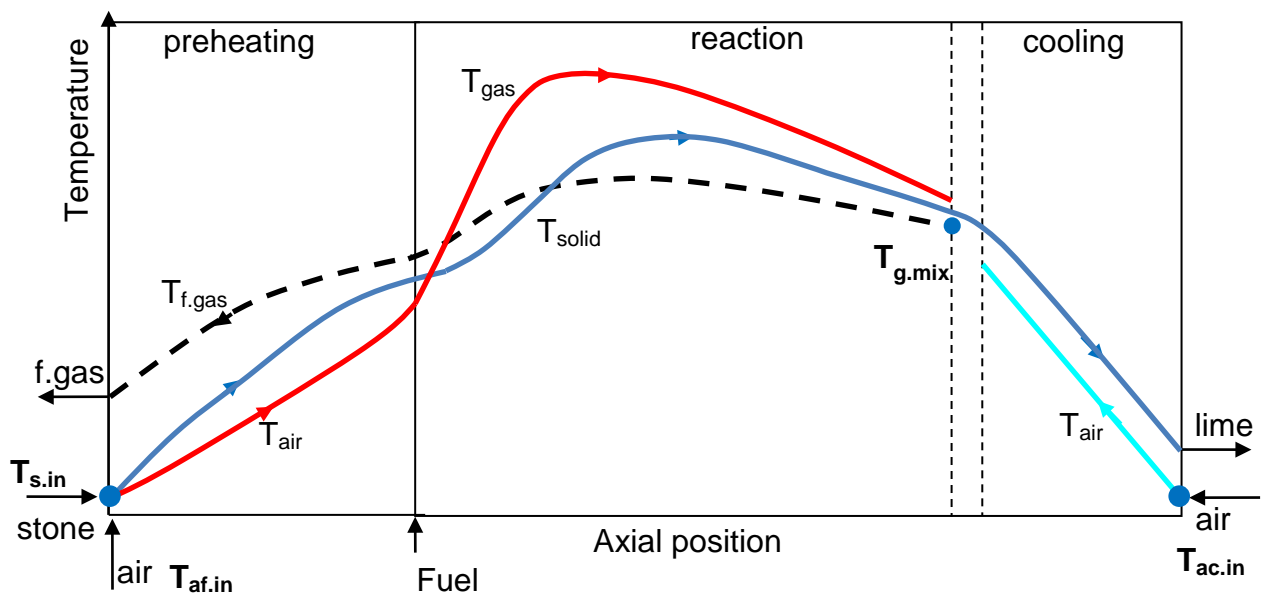

Figure 6-3: Principal temperature profiles in the PFR kilns

```
                        ┌──────────┐
                        │  start   │
                        └──────────┘
                             │
                             ▼
              ╱───────────────────────────╲
              ╱      Input parameters       ╱
             ╱───────────────────────────╱
                             │
                             ▼
          ╱──────────────────────────────────╲
          ╱    Assume gas mix. temp. at        ╱
         ╱      crossover-channel T_g.mix      ╱
        ╱──────────────────────────────────╱
                             │
                             ▼
              ┌──────────────────────────────────┐
              │  Calculation preheating and       │
              │           reaction zone           │
              └──────────────────────────────────┘
                             │
                             ▼
              ┌──────────────────────────────────┐
              │     Calculation cooling zone      │
              └──────────────────────────────────┘
                             │
                             ▼
   ┌──────────────────┐            N      ◇
   │  Modify T_g.mix   │◄──────────────◇ Energy balances ?
   └──────────────────┘                   ◇
                                          │ Y
                                          ▼
                         ╱───────────────────────────╲
                         ╱      Output results         ╱
                        ╱───────────────────────────╱
                                          │
                                          ▼
                                   ┌──────────┐
                                   │   End    │
                                   └──────────┘
```
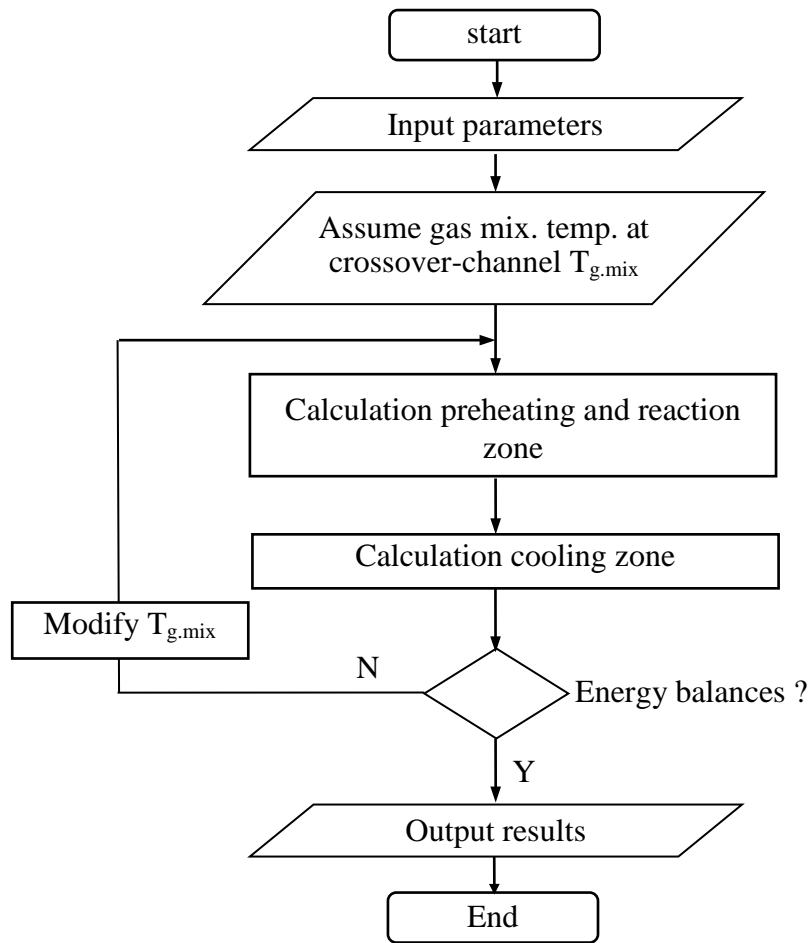
Figure 6-4: Flow chart of numerical solution developed by using the commercial solver bvp4c
      in MATLAB

6.3 Results of simulation

6.3.1 Basic input data

Table 6-1 describes general input variables for simulations. The kiln (one shaft) has a total solid bed height of 17 m. The total specific throughput of two shafts is 44 t/d/m^2 so that each shaft has a throughput of 22 t/d/m^2. The fuel used is the natural gas with the specific energy consumption of 3.45 MJ/kg$_{lime}$ and the excess air number of 1.15. The mean particle size is 60 mm and the limestone contains 96 % of calcium carbonate.

Table 6-1 Basic data for simulation of the PFR kiln

	Input variables	**Units**	**Value**
	Total length of solid bed	m	17
	Length of preheating zone	m	6
Kiln dimension (one shaft)	Length of burning zone	m	6
	Length of crossover-channel	m	0.5
	Length of cooling zone	m	4.5
	Heat consumption (natural gas fuel)	MJ/kg$_{lime}$	3.45
Combustion process		kcal/kg$_{lime}$	825
	Excess air number (combustion air)	-	1.15
	Limestone input flow	t/d/m^2	38
	Lime output flow	t/d/m^2	22
	Combustion air flow	m$^3_{air}$/kg$_{lime}$	1.12
	Lime cooling air flow	m$^3_{air}$/kg$_{lime}$	0.7
Kiln operating process	Lance cooling air flow	m$^3_{air}$/kg$_{lime}$	0.1
	Transport air flow	m$^3_{air}$/kg$_{lime}$	0
	Fuel flow	m^3/kg$_{lime}$	0.1
	Air feed temperature	^{o}C	20
	Limestone feed temperature	^{o}C	20
	Mean particle size	mm	60
Lime and limestone	Average void fraction of solid bed	-	0.38
	CaCO$_3$ content in limestone	% mas	96

6.3.2 Principal temperature and conversion profile

Figure 6-5 shows the principal temperature and conversion profiles in a PFR kiln. The figure is illustrated in the horizontal direction, which is transferred corresponding to the schematic diagram of the PFR shaft shown before. As mentioned before, the mathematical models simulate the mean values of the periodic fluctuations. Therefore, the temperature profiles shown in this figure represent the mean values of the solid, the gas and the flue gas temperatures in the periodic case.

Initially, the limestone is charged into the kiln at the top (0 m) at an ambient temperature of 20°C. The stone is preheated by the flue gas in the non-burning mode with counter-current flow arrangement. After that, in the burning mode, it transfers heat to the combustion air characterized by co-current flow. The temperatures of both the stone and the combustion air increase in this zone. The firing zone begins at 6 m where the fuel is introduced through the lances. It is assumed that the combustion of the mixture of the fuel and the air starts immediately, thus the gas temperature starts increasing rapidly. The stone temperature also increases and it reaches the reaction temperature (820°C) at 6.3 m. The decomposition of the stone begins and its mass fraction starts decreasing. In the region from 6 m to 7 m, the solid temperature is lower than the flue gas temperature but it is still higher than the gas temperature. After that, because of higher combustion rate, the combustion gas temperature increases faster and it exceeds the solid temperature, thus both the combustion gas and the flue gas transfer heat to the solid. The solid temperature keeps increasing until it gets higher than the flue gas temperature at 8 m. As a result, from this position to the end of the firing zone (12 m), the solid gets heat from the combustion gas (in burning mode) and it transfers heat to the flue gas (in non-burning mode). The solid leaves the firing zone with a temperature of about 1010 °C then it enters the cooling zone where it is cooled down by the cooling air until it reaches the lime discharge temperature.

Table 6-2 Results of simulation of the PFR kiln

Outputs	Unit	Values
Flue gas temperature	°C	103
Lime discharge temperature	°C	82
Calcination length	m	5.7
Residual CO_2	%	1.9
Maximum gas temperature	°C	1240
Maximum solid temperature	°C	1068
Total pressure drop	mbar	340
Heat loss by the kiln wall	%	6.1

In addition, other characteristic values of the simulations are summarized in **Table 6-2** in the same manner as before. The temperature of the flue gas is 103 °C and that of the lime discharge is 82 °C. The maximum temperature of the gas is 1240 °C and that of the solid is 1068 °C. The heat loss through the kiln wall is about 6.1 % and the pressure drop is 340 mbar.
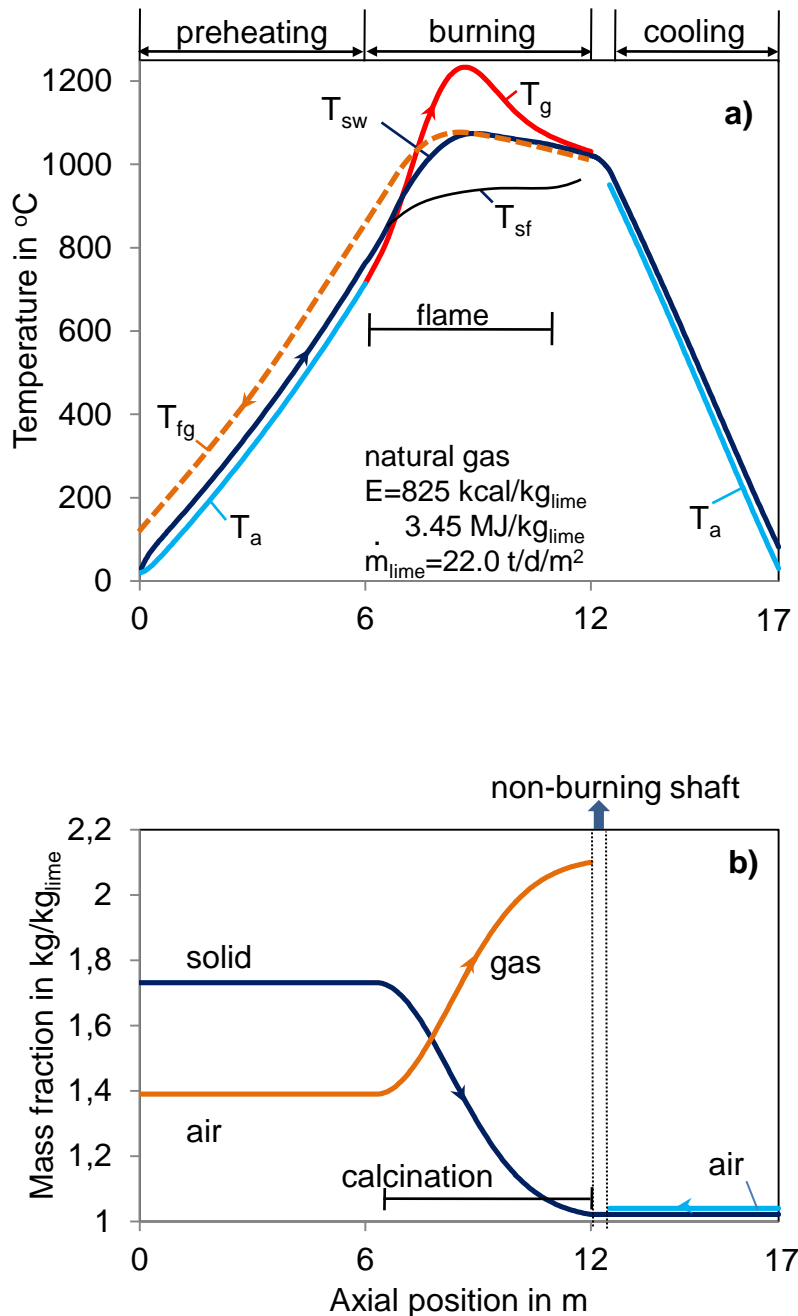
Figure 6-5: Principal temperature and mass fraction profiles in a PFR kiln

An important remark is observed from the Figure 6-5 that the flue gas leaving the burning shaft is heated up in the non-burning shaft by the solid. At the kiln height of about 8 m, the

flue gas temperature exceeds the solid temperature. Therewith the flue gas transfers heat from the end of the burning shaft to the beginning of the combustion zone.

6.3.3 Pressure drop profile

Figure 6-6 shows a principal pressure drop profile along the PFR kiln. It can be seen that the total pressure is about 340 mbar, in which the pressure drop in the burning shaft is about 120 mbar and that of the non-burning shaft is 220 mbar. The pressure drop in the non-burning shaft is significantly greater than that of the burning shaft. This is because the gas flow in the non-burning shaft is much higher. It includes the total gas flow in the burning shaft, the total cooling air flow and the lance cooling air flow.
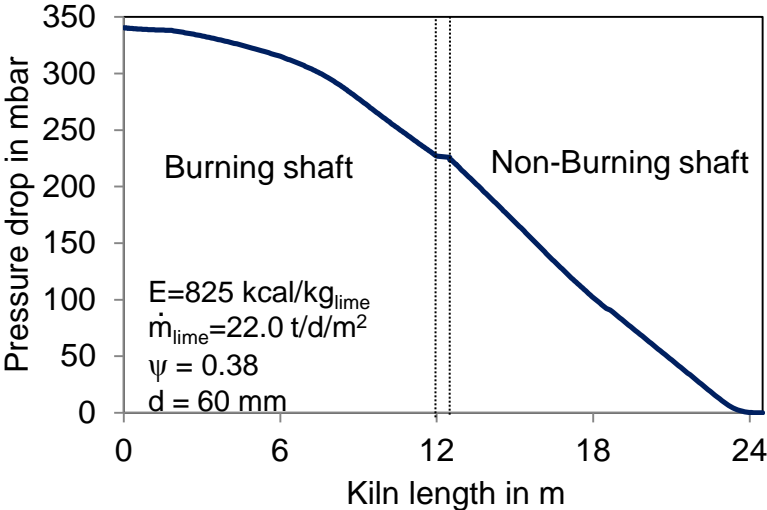

Figure 6-6: Principal pressure drop profile along a PFR shaft kiln

6.4 Influencing parameters

6.4.1 Influence of energy input

Figure 6-7 shows the temperature and the conversion profiles in the burning zone for different energy inputs. As an example, simulations were done for the energy input varied in the range of 810 - 840 kcal/kg$_{lime}$ and other inputs were kept the same as given in Table 6-1.

Table 6-3 Influences of energy input

Energy input	**kcal/kg$_{lime}$**	**810**	**825**	**840**
Flue gas temperature	^{o}C	99	103	111
Lime temperature	^{o}C	76	80	91
Residual CO_2	%	2.6	1.9	1.3
Max. gas temperature	^{o}C	1178	1240	1306
Max.solid temperature	^{o}C	1036	1068	1130
Total pressure drop	mbar	328	340	355

As observed before in the normal shaft kiln, the higher the energy input, the more heat is generated by the combustion, this results in a higher kiln temperature. Hence, the decomposition process becomes faster and requires a shorter zone.

In addition, **Table 6-3** summarizes the characteristic values of the simulation. The flue gas, the lime discharge, the kiln maximum temperatures and the pressure drop increase with the increase of the energy. However, the residual CO_2 decreases with the increase of the energy.
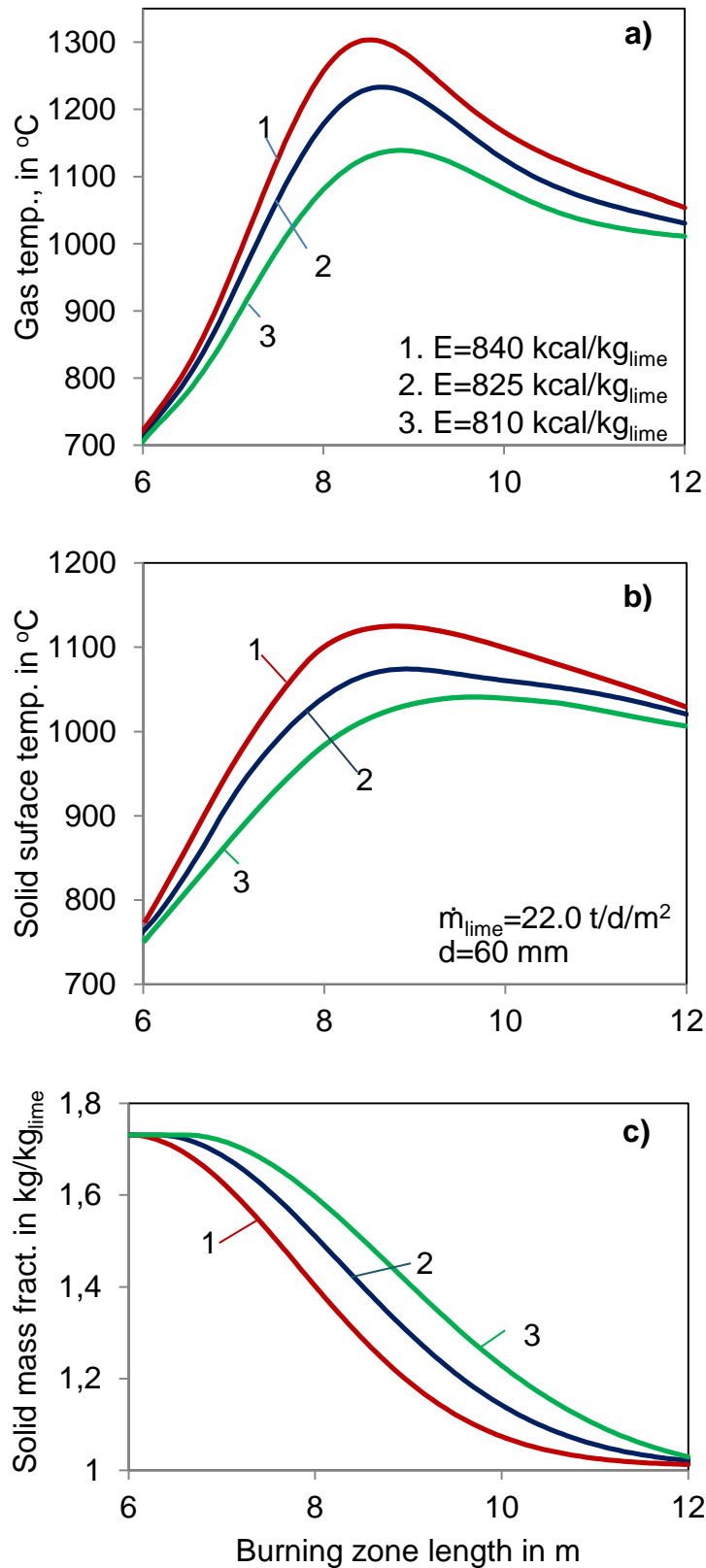
Figure 6-7: Influence of energy input on the temperature and the conversion profiles

6.4.2 Influence of lime throughput

Figure 6-8 and **Table 6-4** show the simulation results in the same manner as before for different kiln throughputs. Simulations were done for the kiln throughput varied in the range of 20.5 – 23.5 $t/d/m^2$ while other inputs were kept the same as given in Table 6-1. Similar to the normal shaft kiln, a lower kiln throughput leads to a longer residence time and causes a higher kiln temperature. This results in a faster calcination rate and a shorter calcination zone. In addition, in Table 6-4, it is observed again that the residual CO_2 and the pressure drop increases considerably with an increase of the kiln throughput. However, the kiln maximum temperature decreases significantly.

Table 6-4 Influences of lime throughput

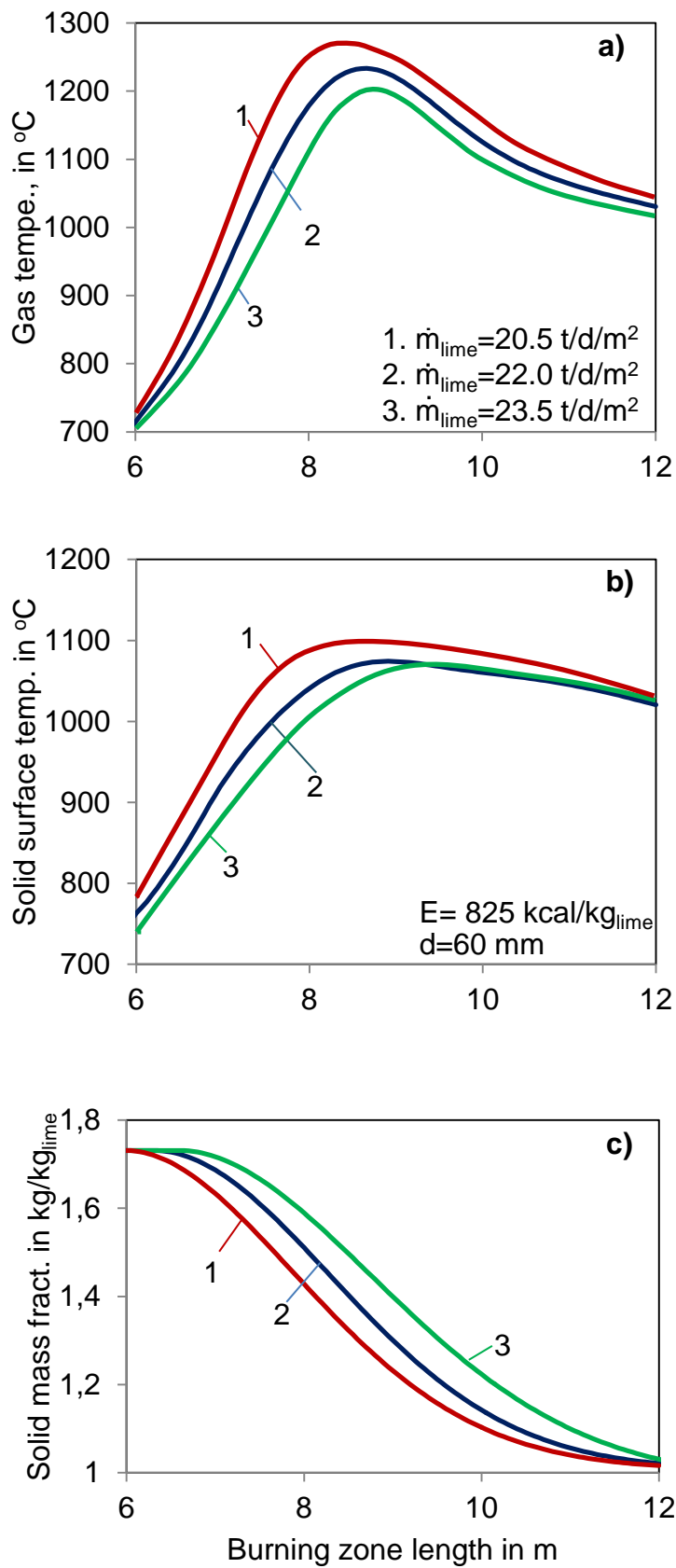| Lime throughput	$t/d/m^2$	20.5	22.0	23.5
Flue gas temperature	^oC	98	103	115
Lime temperature	^oC	76	80	90
Residual CO_2	%	1.5	1.9	2.4
Max. gas temperature	^oC	1273	1240	1208
Max.solid temperature	^oC	1108	1068	1032
Total pressure drop	mbar	312	340	368

Figure 6-8: Influence of kiln throughput on the temperature and the conversion profiles

6.4.3   Influence of particle size

The effects of the particle sizes on the process are illustrated in **Figure 6-9** and **Table 6-5**. As seen before in the normal shaft kilns, the smaller the particle size, the faster the calcination rate, the shorter the calcination zone and the lower the residual CO_2. However, a decrease of the particle size results in significant increases of the kiln temperature and the pressure drop.

Table 6-5 Influences of particle size

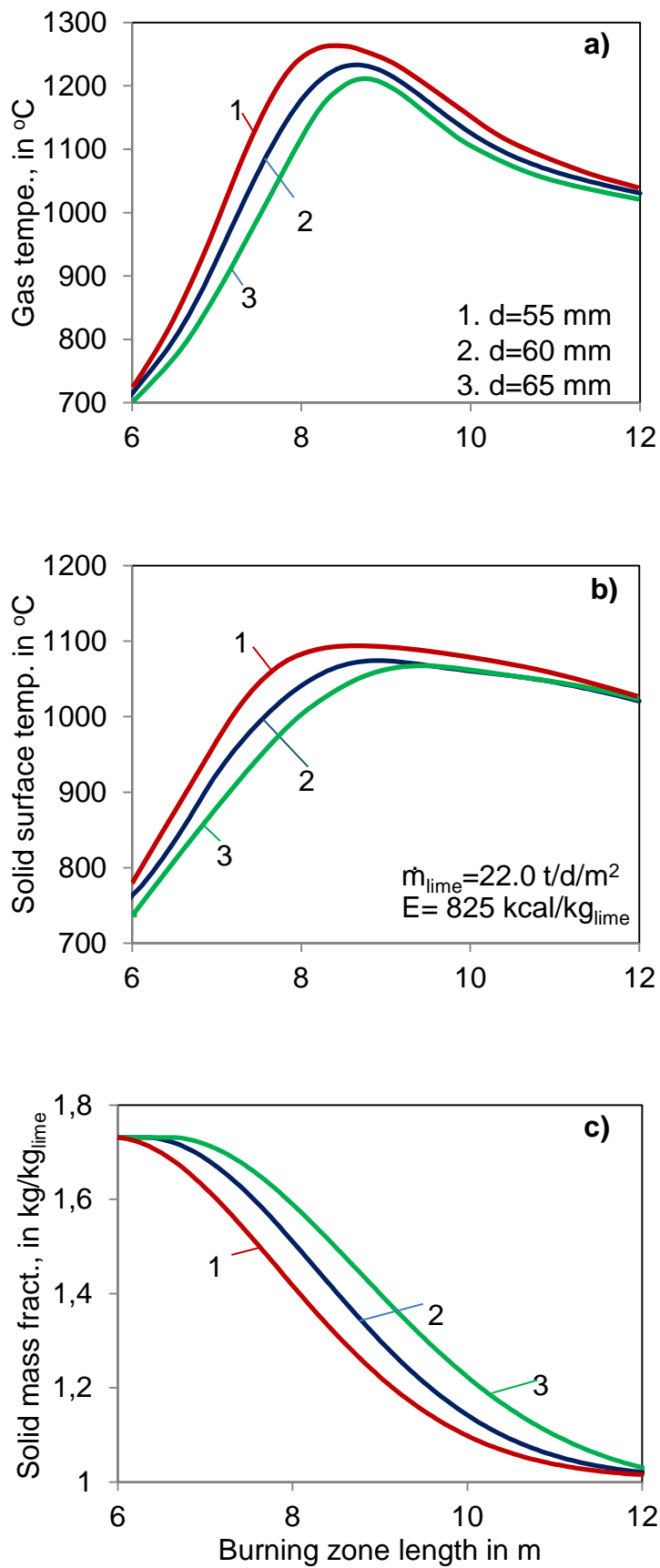| Particle size	mm	55	60	65
Flue gas temperature	^{o}C	99	103	114
Lime temperature	^{o}C	78	80	88
Residual CO_2	%	1.6	1.9	2.3
Max. gas temperature	^{o}C	1268	1240	1206
Max.solid temperature	^{o}C	1099	1068	1030
Total pressure drop	mbar	373	340	316

Figure 6-9: Influence of particle size on the temperature and the conversion profiles

6.4.4 Influence of limestone origin

As mentioned before, limestones of different origins differ in their properties such as the reaction coefficient and the thermal conductivity. As the first example, two types of limestones with different thermal conductivity were selected for simulations. The simulation results are shown in **Figure 6-10** and **Table 6-6**.

Table 6-6 Influences of thermal conductivity

Limestone		No.1 (λ=0.6 W/m/K)	No.2 (λ=0.8 W/m/K)
Flue gas temperature	^{o}C	115	99
Lime temperature	^{o}C	93	78
Residual CO_2	%	2.3	1.5
Max. gas temperature	^{o}C	1218	1226
Max. solid surface temp.	^{o}C	1092	1081
Average solid core temp.	^{o}C	870	890
Total pressure drop	mbar	334	338

In Figure 6-10, the surface and the core temperatures of the solid particles are plotted together to compare. The limestone No.2 with a higher thermal conductivity decomposes faster, needs a shorter calcination zone and results in a lower residual CO_2. The limestone with a higher thermal conductivity needs a lower temperature difference between the surface and the core as driving force for the decomposition process. Therefore, this causes a higher core temperature and a lower surface temperature, while the average temperature of the lime layer will stay roughly the same.

Figure 6-11 and **Table 6-7** show the simulation results for limestones with different reaction coefficients. According to Cheng et al. [56, 57], the reaction coefficient varies in the range from 0.004 to 0.012 m/s within a factor of 3. As an example, simulations were done by using the lowest and the highest values of the reaction coefficient. It can be seen that a higher reaction coefficient leads to a faster decomposition rate and a shorter calcination zone, thus it results in a lower residual CO_2. In addition, a larger reaction coefficient needs a lower decomposition pressure as driving force and thus a lower reaction front temperature. Besides, a larger reaction coefficient leads to a lower average temperature of the lime layer. This is not the case with the thermal conductivity since the average temperature of the lime layer stays roughly the same.
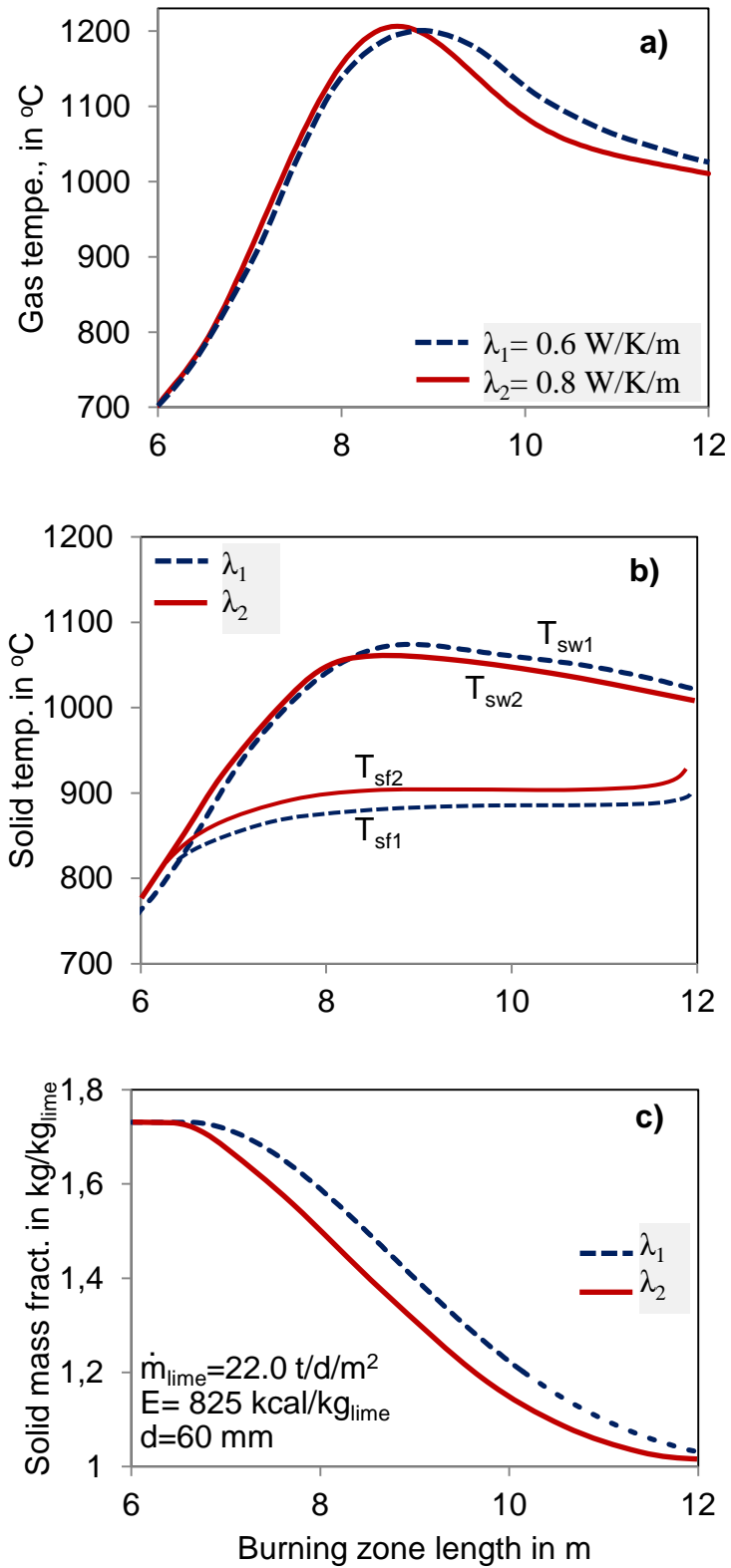
Figure 6-10: Influence of thermal conductivity on the temperature and conversion profiles
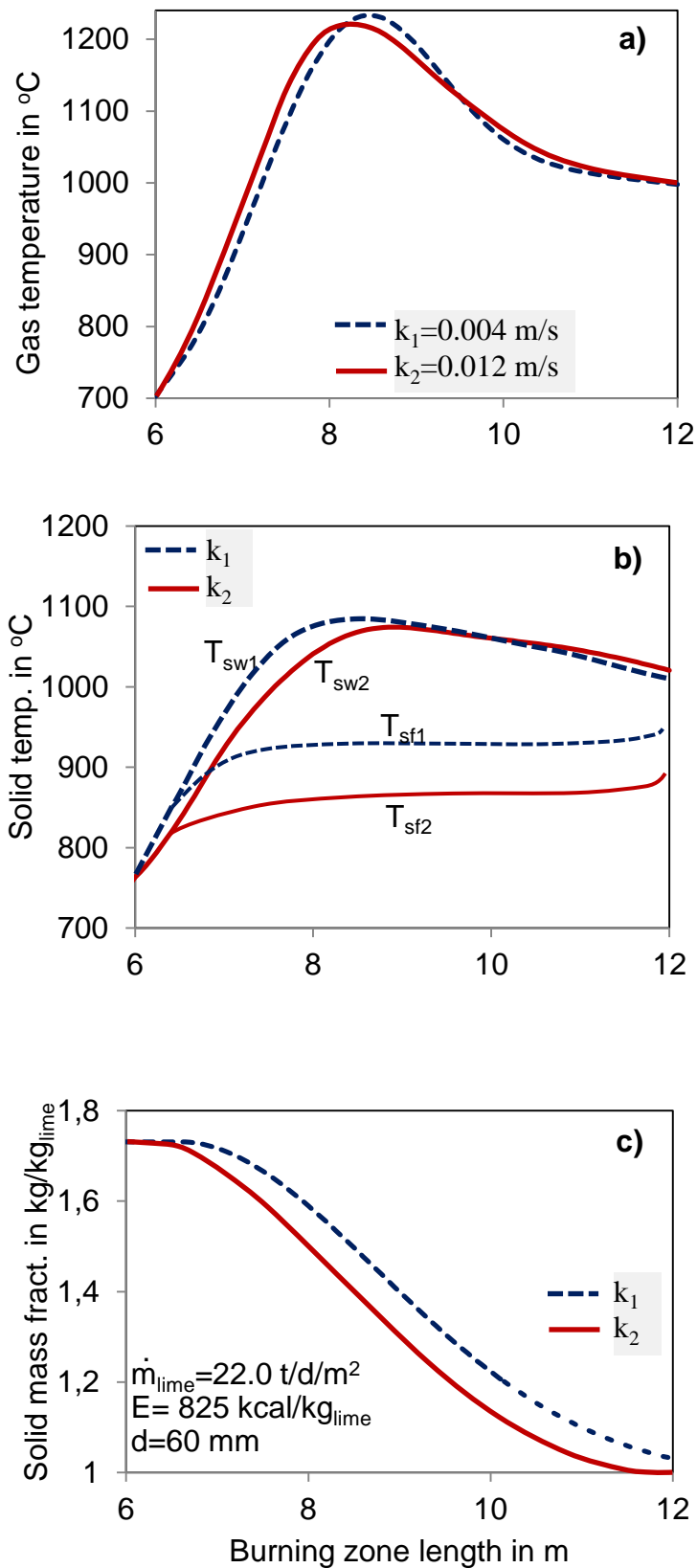
Figure 6-11: Influence of reaction coefficient on the temperature and conversion profiles

Table 6-7 Influences of the reaction coefficient

Limestone		No.3 (k=0.004 m/s)	No.4 (k=0.012 m/s)
Flue gas temperature	^{o}C	118	86
Lime discharge temp.	^{o}C	100	70
Residual CO_2	%	3.0	0.3
Max. gas temperature	^{o}C	1224	1231
Max. solid surface temp	^{o}C	1088	1078
Average solid core tempe	^{o}C	920	840
Total pressure drop	mbar	332	343

6.4.5 Influence of excess air number

Figure 6-12 and **Table 6-8** reveal the simulation results for different excess air numbers. Simulations were done for the excess air numbers varied in the range from 1.05 to 1.2 while other inputs were kept the same as before. Similar to the normal shaft kilns, it can be seen again that an increase of the excess air number results in a lower kiln temperature, but it leads to a higher residual CO_2 and a higher pressure drop.

Table 6-8 Influences of excess air number

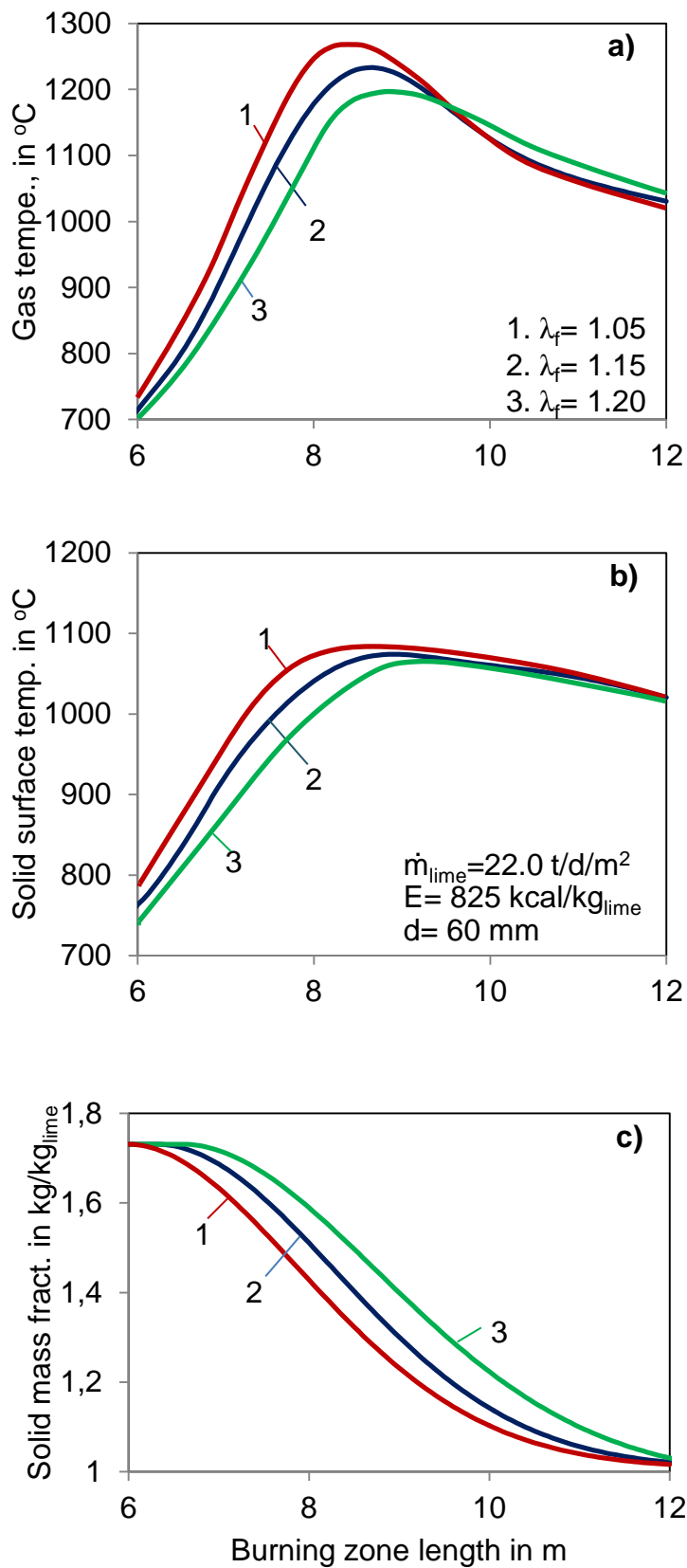| Eff. excess air number	-	1.05	1.15	1.20
Flue gas temperature	^{o}C	100	103	109
Lime temperature	^{o}C	78	82	84
Residual CO_2	%	1.6	1.9	2.2
Max. gas temperature	^{o}C	1273	1240	1210
Max.solid temperature	^{o}C	1098	1068	1036
Total pressure drop	mbar	320	340	351

Figure 6-12: Influence of excess air number on temperature and the conversion profiles

6.4.6 Influence of fuel combustion behavior

Figure 6-13 and **Table 6-9** illustrate the simulation results of the effects of the fuel combustion behavior or the flame length on the kiln process. As discussed before in the normal kilns, a shorter flame results in a significantly higher peak of the gas and the solid temperature. If the flame is very short, the residual CO_2 increases considerably.

Table 6-9 Influences of fuel combustion behavior

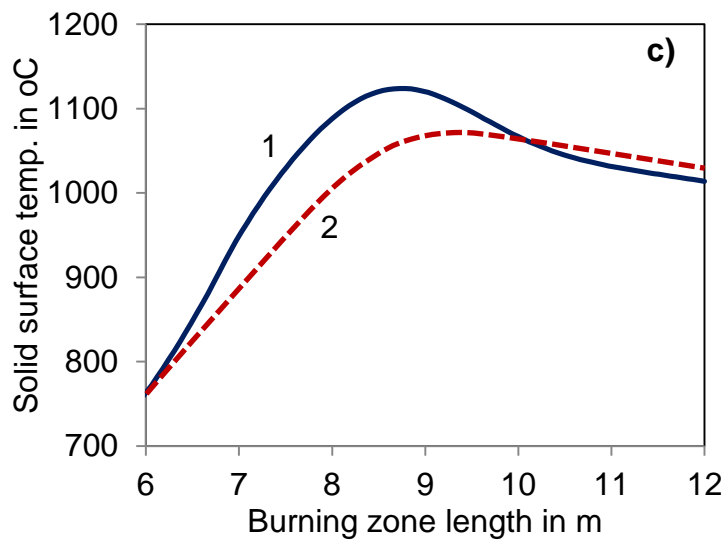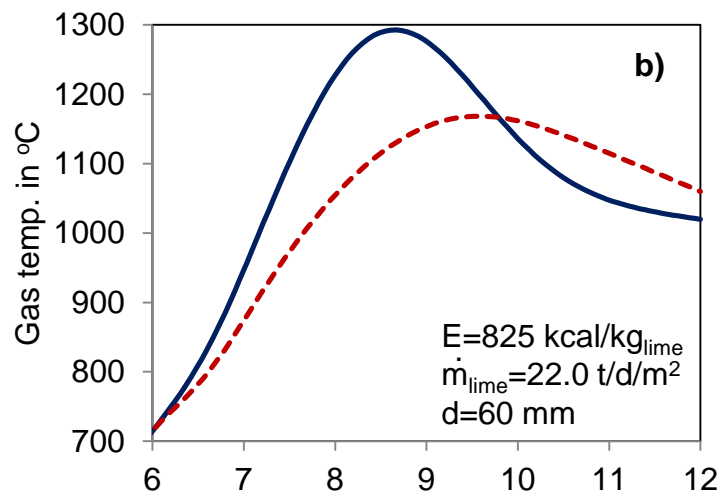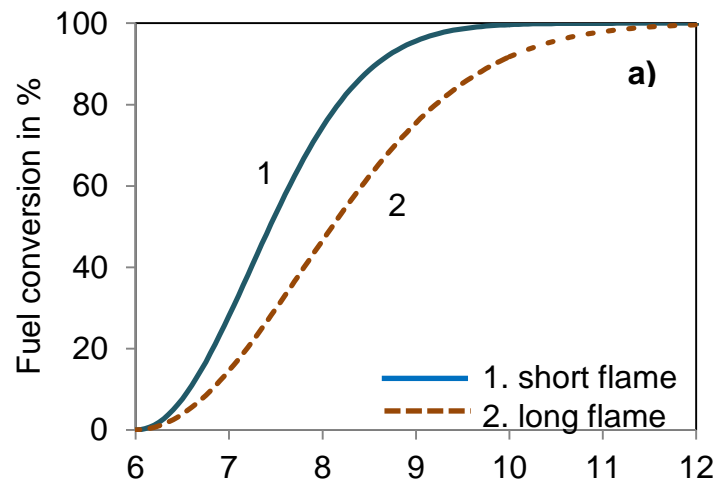| **Flame length**	**m**	**4.5**	**6**
Flue gas temperature	^{o}C	104	101
Lime temperature	^{o}C	83	80
Residual CO_2	%	2.0	1.8
Max. gas temperature	^{o}C	1290	1180
Max.solid temperature	^{o}C	1118	1041
Total pressure drop	mbar	343	338

Figure 6-13: Influences of fuel combustion behavior on the temperature profiles

6.5 Influence of kiln dimension

Finally, the influence of the lengths of the preheating, the firing and the cooling zones on the process is investigated. As an example, **Figure 6-14** shows the simulations results for the first case with different preheating zone lengths of 6 m and 4 m. It can be seen that a shorter preheating zone results in a lower kiln temperature, but it leads to a higher residual CO_2, **Table 6-10**. In this simulation, by shortening the preheating zone by 2 m, the residual CO_2 increases from 1.9 % to 2.3 %. In the second simulation, the firing zone is extended from 6 m to 8 m. This extension of the firing zone results in a decrease of the residual CO_2 from 2.3 % to 1.8 %. However, it also leads to considerable increases of the kiln maximum temperatures and the pressure drop.

Table 6-10 Influences of the kiln length

Case		Ref.	1	2
Preheating zone length	m	6	4	4
Firing zone length	m	6	6	8
Flue gas temperature	^{o}C	103	110	100
Lime temperature	^{o}C	82	91	76
Residual CO_2	%	1.9	2.3	1.8
Max. gas temperature	^{o}C	1240	1138	1206
Max.solid temperature	^{o}C	1068	1020	1046
Total pressure drop	mbar	340	286	333

Figure 6-15 illustrates the simulation results for different cooling zone lengths. Simulations were done in two cases for the cooling zone lengths of 4 m and 5 m. To see how the cooling length affects the cooling process, it is assumed in both cases that the lime enters the cooling zone with the same temperature of 1000°C. A shorter cooling zone results in a faster cooling lime process, however it leads to a higher lime discharge temperature, **Table 6-11**. In this simulation, by shortening the cooling zone by 1 m, the lime discharge temperature increases almost 12 ^{o}C. The lime discharge temperature can be lowered by introducing more cooling air. For example, in Table 6-11 it shows that the lime discharge temperature decreases 14 ^{o}C by increasing the cooling air from 0.7 to 0.72 m^3_{air}/kg$_{lime}$.

Table 6-11 Influences of the cooling zone length

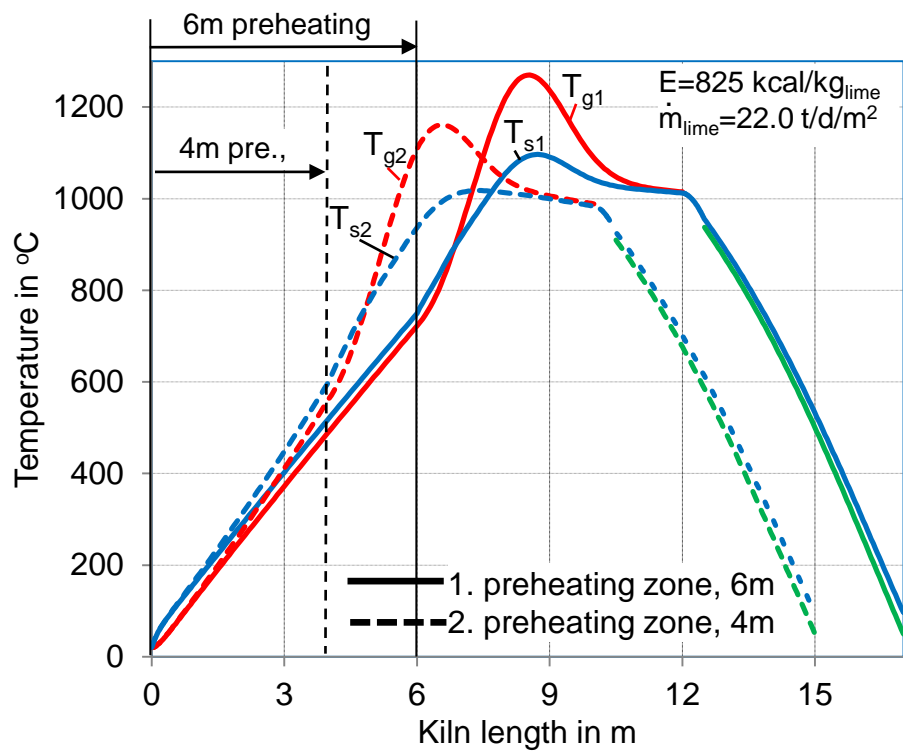| Cooling zone length	m	5	4	4
Cooling air factor	m^3_{air}/kg_{lime}	**0.7**	**0.7**	**0.72**
$T_{lime.in}$	^oC	1000	1000	1000
$T_{air.in}$	^oC	20	20	20
$T_{lime.out}$	^oC	80	92	78

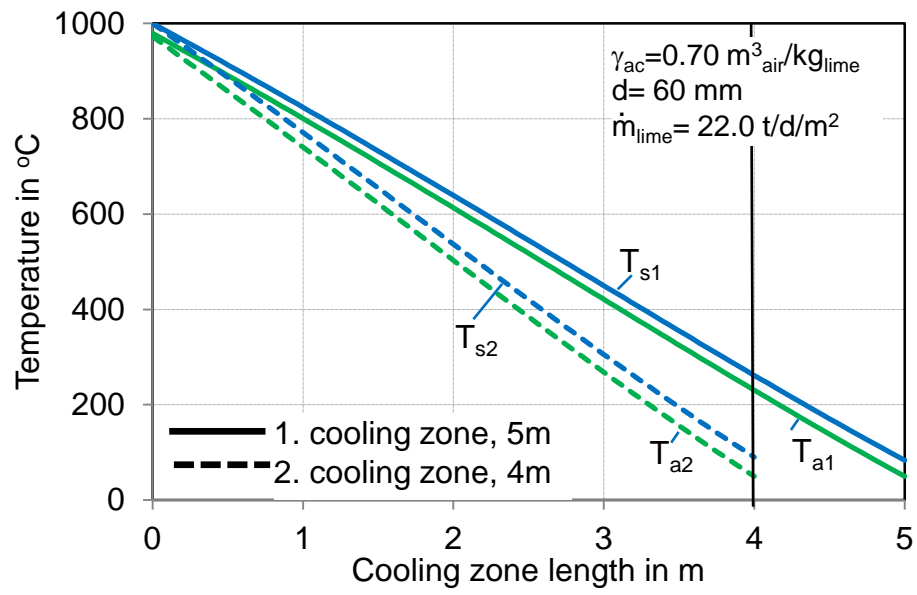Figure 6-14: Influence of the length of preheating zone on the temperature profiles

Figure 6-15: Influence of the length of cooling zone on the temperature profiles

7 Measurement and validation of temperature profile

7.1 Normal shaft kilns

Two normal shaft kilns were selected for the measurement. **Figure 7-1** shows a schematic diagram of the chosen normal shaft kiln A. The kiln has a total solid bed height of 12 m, in which the height from the top to the burner level is about 7.5 m. The level 0 m is defined as an average value of the filling level of stones at the kiln top. The kiln has a throughput of 200 t/d. Thermocouples (type K, Ni-Cr/Ni) with a length of 30 m, a diameter of 6 mm and a maximum permissible temperature of 1370 $^{\circ}$C, were inserted from the top. During the measurement the thermocouple moved downward together with the stones. The values of the temperature were recorded electronically every 10 - 15 sec. The length of the thermocouple inserted into the solid bed at the top was also recorded. Prior to the experiment the kiln had been operating for several weeks with the same throughput so that the steady-state condition was ensured during the experiment.
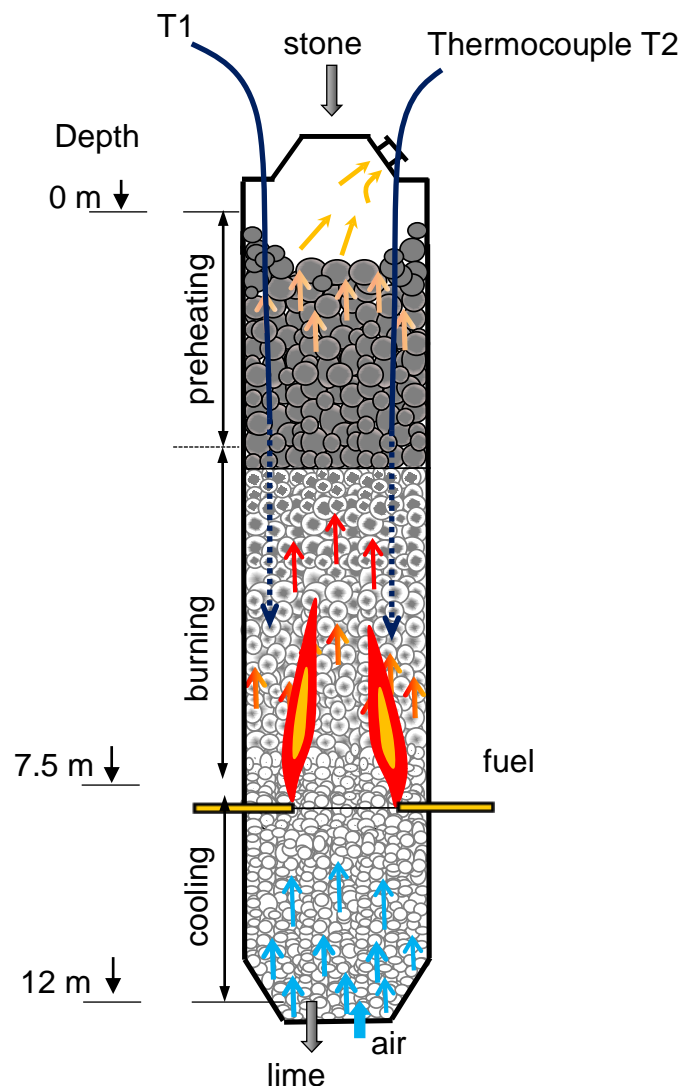

Figure 7-1: Arrangements of measuring temperatures in normal shaft kiln

Figure 7-2: Kilns chosen for measuring temperatures

Figure 7-3: Inserting thermocouples during measurements

Figure 7-4 shows the measured temperatures in the normal shaft kiln A, in which two thermocouples T1 and T2 were inserted. The measured values are plotted in dependence on the depth of the solid bed, in which the coordinate 0 m represents the top of the solid bed. An assumption is that the thermocouples are supposed to move vertically with the solid bed, thus their position is considered the same as the solid bed depth. It can be seen that from the kiln top to about 4 m, both profiles reveal a similar behavior. However, after 4 m the two profiles are significantly different. The thermocouple T1 shows an increase of temperature while the thermocouple T2 remains at a relative constant temperature (830 ^{o}C) in a long range.
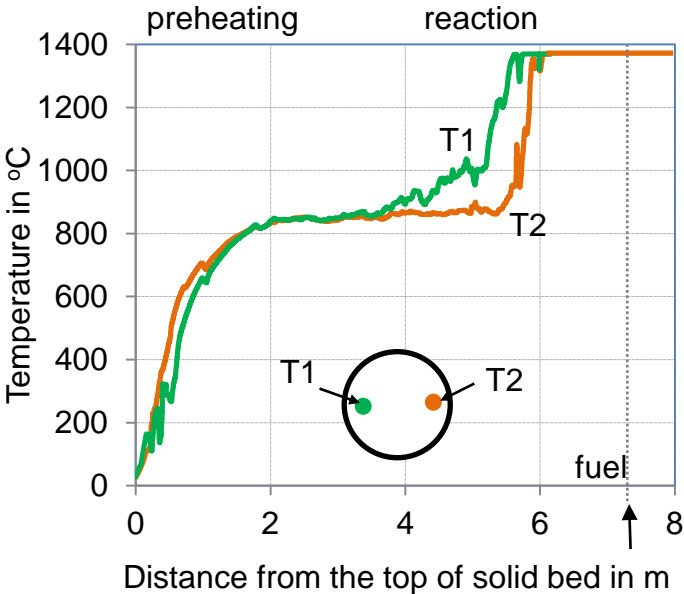

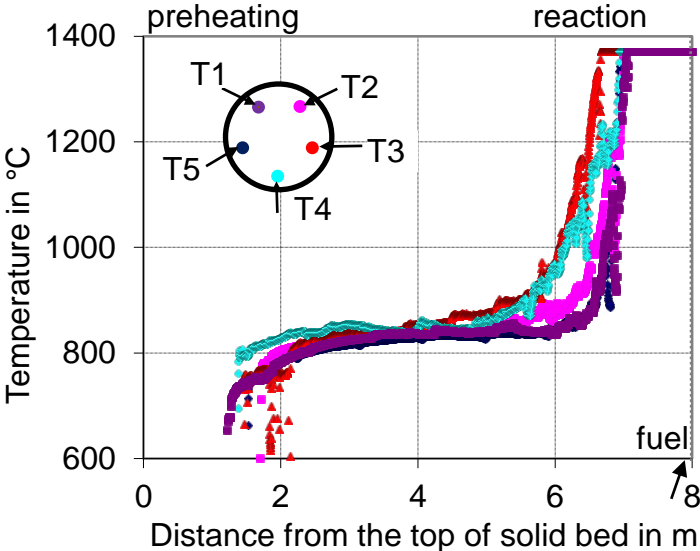Figure 7-4: Measured temperatures in the normal shaft kiln A

Figure 7-5: Measured temperatures in the normal shaft kiln B

The maximum temperature difference between the two profiles is almost 400 ^{o}C at about 5.5 m. There can be multiple reasons causing this difference: a) the condition in the normal shaft

kiln cross-section is not homogeneous; b) the actual positions of two thermocouples are not the same as shown in the figure; c) the thermocouple T1 moves directly to a burner while the thermocouple T2 is in between the burners. The maximum permissible temperature (1370 ^{o}C) of the thermocouples is reached at about 6 m, and then the two thermocouples fail before the fuel injection at about 7.5 m, thus the completed profiles could not be obtained.

Figure 7-5 shows the measured temperatures in the normal shaft kiln B, which has a throughput of 180 t/d of lime. In this measurement, five thermocouples (T1 – T5) with a length of 20 m and a diameter of 3 mm were used. Due to some technical problems, the temperatures were recorded only after the thermocouples moved almost 1.5 m from the top of solid bed. It can be seen again that the five thermocouples show different behavior, especially after 6 m. The maximum temperature difference is also almost 400 ^{o}C. As mentioned before, this can be a result of inhomogeneous conditions in the cross-section of the kiln. Furthermore, the figure demonstrates again that all thermocouples fail after reaching the temperatures of 1370 ^{o}C. As a consequence, the temperatures in the burning zone, which are much higher than the permissible temperature of thermocouples type K, can not be measured. To measure the temperatures in the burning zone of the normal shaft kilns, special thermocouples such as Pt-Rh/Pt are required. However they are too expensive because of the long length (20 – 30 m) making simulations necessary.

Mathematical model is used to simulate the temperature profiles in the normal shaft kiln kilns chosen for the measurements. **Figure 7-6** shows the simulated profiles in the normal shaft kiln A, in which the results are compared with the temperatures measured by thermocouple T1 (Figure 7-4). A remark here is that the solid (surface) temperatures predicted by the model are close to the measured temperature. This can be expected due to two reasons: a) in a high temperature range, the heat transfer by radiation from the stones to the thermocouples is stronger than that by convection from the gas to the thermocouples; b) the thermocouples may be fixed or contacted with the stones during the measurement. As a result, the thermocouples measured mainly the solid surface temperature. In addition, it can be seen from the simulated profiles that the difference between the gas / flue gas and the solid temperatures is significant. The simulated profiles show a significant temperature difference between the gas and the solid. The maximum temperatures predicted by the model are about 1600 ^{o}C. The peak temperatures are in the regions near the burners. Unfortunately, it is not possible to compare the values and positions of the peak temperatures with the experiment. To compare positions of the peak temperature, measurements of the outer shell temperature were carried out and the results are presented in the following.

Figure 7-7 shows the outer shell temperature profiles in the normal shaft kiln A. Temperatures at four different positions in circumferences were measured by an Infrared thermometer. It can be seen that shell temperatures have a maximum value of about 165 ^{o}C. The maximum values distribute at a position of about 6.0 m. A remark here is that this position is in the range of the maximum temperatures predicted by the model and shown before in Figure 7-6.
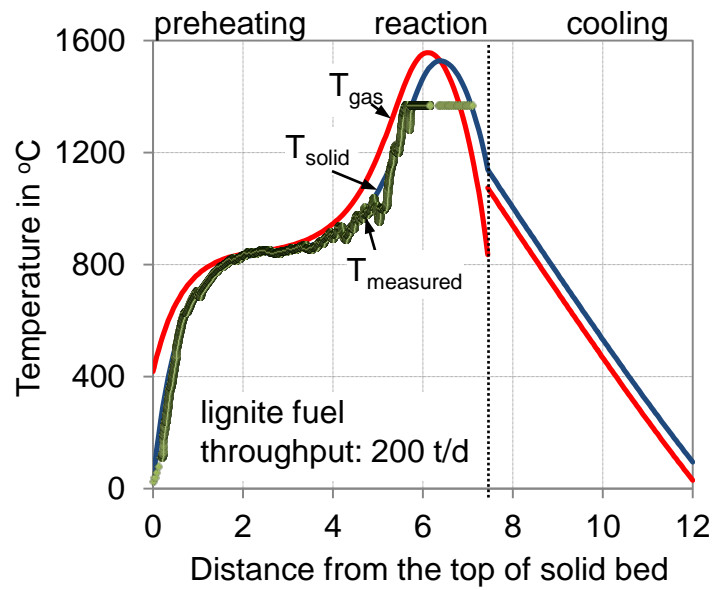
Figure 7-6: Measured & simulated temperatures in the RCE-kiln A

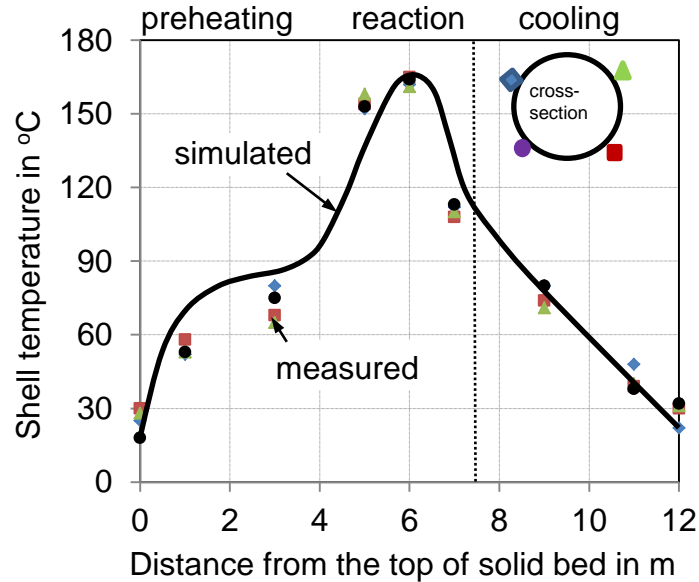Figure 7-7: Outer shell temperatures in the normal shaft kiln A

Figure 7-8 shows the simulated temperature profiles in the normal shaft kiln B. The results are compared with the temperature profiles measured by the two thermocouples T3 and T4 (Figure 7-5). It can be seen again that the measured temperatures are similar to the lime surface temperature calculated by the model. The maximum temperatures are about 1500 ^{o}C

and they distribute near the burners. Unfortunately, there is no measured shell temperature profile, thus the position of the peak temperatures inside the kiln is not possible to validate.
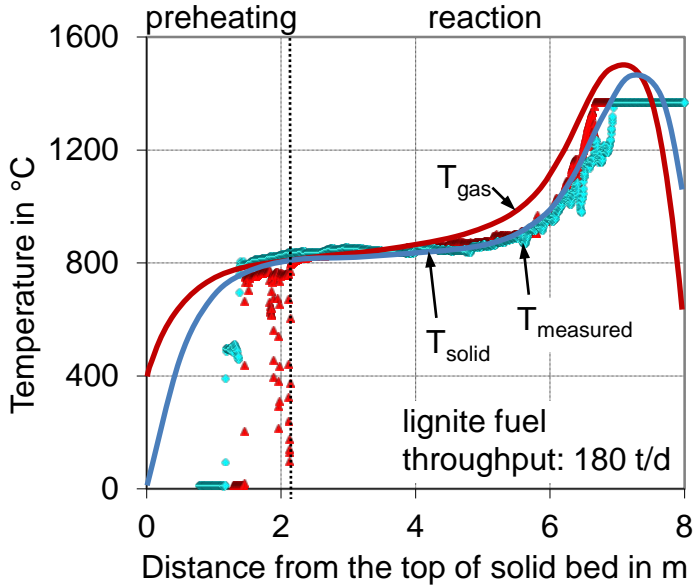

Figure 7-8: Measured & simulated temperatures in the normal shaft kiln B

7.2 PFR kilns

The procedure for measuring the temperature profiles in the PFR kiln is similar to that of the normal shaft kilns kiln. The kiln has a total solid bed height of 18 m, in which the height from the top to the cross-over channel is 14 m. The kiln has a total throughput of 370 t/d. In each shaft (S1, S2) of the kiln, a thermocouple type K, which has the same specification as mentioned before (used for normal shaft kiln A) was inserted from the top.

Figure 7-9 shows the temperatures measured in two shafts S1 and S2 of the PFR kiln. It can be seen that at the beginning of the preheating zone both profiles fluctuate with changes of about 50 - 100 ^{o}C, then the changes become higher. Temperatures can even be up to 300 ^{o}C in the burning zone. This is due to the fact that two shafts are operated in two distinct modes, burning and non-burning with a periodic time of about 14 min for each cycle. From 0 m to 4 m the two profiles show similar behaviors. However, after 4 m there is a significant temperature difference between the two profiles. The thermocouple in shaft S1 seems to have a delay and the temperatures measured in shaft S1 are lower than that of shaft S2. For example, at about 6 m the temperature difference between the two shafts is almost 300 ^{o}C. There can be a number of reasons causing this difference. Firstly, the thermocouple in shaft S1 did not move vertically together with the stones, it may be shifted in the solid bed; thus its position is not as deep as the solid bed depth shown in the figure. Secondly, the thermocouple in shaft S2 may be directly below the burners (outlet of lances) while the thermocouple in shaft S1 is between the lances. Thirdly, it can be also that the length of lances is different since it is known that this length is shortened randomly with time. Finally, the last reason can be that the fuel supply through the lances is not homogeneous in the cross section of the PFR-kiln. Due to some technical problems, the measurement was stopped when one thermocouple arrived at the cross-over channel (14 m). Therefore, the temperature profiles in the cooling zone were not measured. However, these profiles are not important for the validation of the simulation.

As mentioned before, the thermocouple in shaft S1 could be shifted in the solid bed during the measurement. Therefore, its length shown before in Figure 7-9 is shortened, for example by 2 m. **Figure 7-10** shows the new modified temperature profile in shaft S1, in which the temperature profile in shaft S2 is also plotted. It can be seen that the two profiles are more similar. However, a temperature difference of about 100 ^{o}C is still observed between the two shafts, particularly in the burning zone. This difference can be caused by two reasons. Firstly, the operating conditions between the two shafts are different; however this seems to be improbable. Secondly, the cross-section has an inhomogeneous temperature distribution because of imperfect fuel distribution for example.
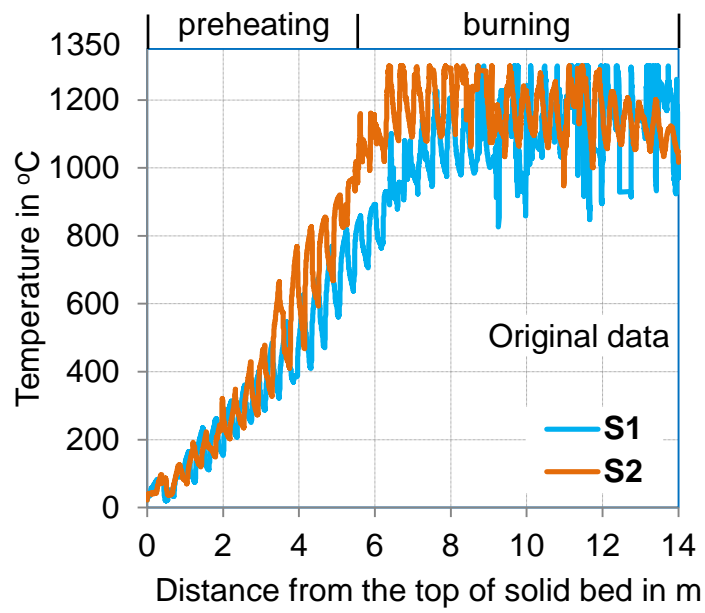
Figure 7-9: Measured temperatures in the PFR kiln: Original data
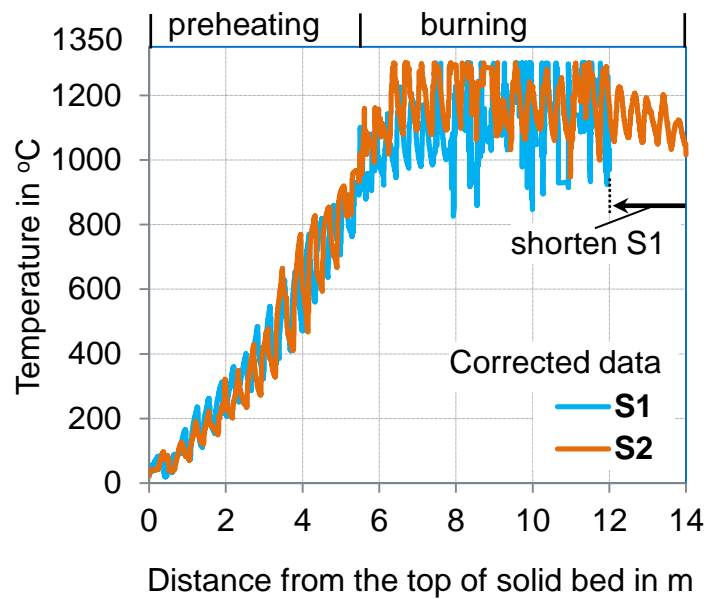

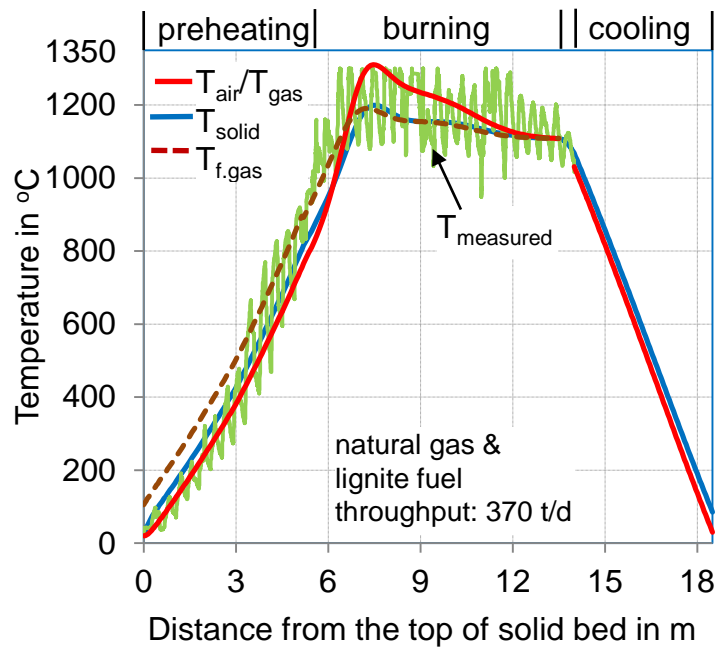Figure 7-10: Measured temperatures in the PFR kiln: Corrected data

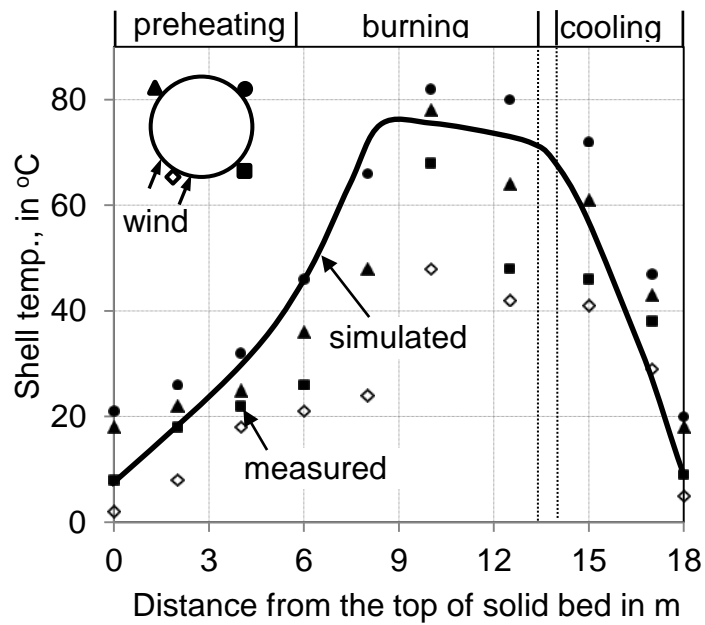Figure 7-11: Measured & simulated temperatures in the PFR kiln

Figure 7-12: Outer shell temperatures in the PFR kiln

The mathematical model is used to simulate the temperature profiles in the PFR kiln. **Figure 7-11** shows the simulated profiles, which are compared with the temperatures measured in shaft S2. As mentioned before, the model is used to calculate the mean values of the periodic fluctuations. Therefore, in Figure 7-11, the calculated profiles represent the mean temperature values of the gas, the flue gas and the solid (limestone / lime). It can be seen that the simulated values lie in the range of the measurement. It can be seen that the solid (surface) temperatures predicted by the model are close to the average values of the measurement. The reason is explained as before with the normal shaft kilns. In addition, it can be seen from the simulated profiles that the difference between the gas / flue gas and the solid temperatures is significant, particularly in the burning zone. The difference can be up to 100 ^{o}C at the beginning of this zone then it decreases reaching the end of this zone. As discussed before, it is not possible to observe this temperature difference by the measurement.

Figure 7-12 shows the outer shell temperatures along the PFR-kiln axis. It can be seen that the temperatures measured in a circumference are significantly different because they are affected by the wind direction. The temperatures measured on the side with the stagnation points of the wind direction are lower than that of the other sides because at the stagnation points the convective heat transfer coefficient is highest. Furthermore, it can be seen that the simulated profile lies in the range of the measured values. This profile shows a similar behavior to that of the simulated temperatures shown before in Figure 7-11.

8   Conclusions and outlook

Conclusions

One-dimensional mathematical models have been developed to simulate the lime burning process in the normal shaft kilns and the PFR kilns. The following significant outputs were determined:

- The solid core and surface temperatures of the lime / limestone particles

- The gas temperature, including the flue gas temperature

- The lime conversion degree or the residual CO_2 in lime

- The heat loss by the kiln wall

- The pressure drop along the kiln axis

The models were used to investigate the parameters, which affect significantly the kiln process. The following essential information has been obtained:

- The increase of the energy input leads to the decrease of the residual CO_2, but it causes the increase of the kiln temperatures as well as the pressure drop

- The decrease of the kiln throughput results in the decrease of the residual CO_2 and the pressure drop; however, the kiln temperatures increase

- The smaller the particle size, the faster the burning process and the lower the residual CO_2. However, a small particle size leads to a significant increase of the pressure drop

- A higher excess air number results in a lower kiln temperature, but it leads to a higher residual CO_2 and a higher pressure drop

- Limestone with a low thermal conductivity or a low reaction coefficient causes a low calcination rate and requires a long calcination zone. Additionally, a lower reaction coefficient also results in a higher average temperature of the lime.

- The shorter the flame length, the higher the kiln maximum temperatures, but a short flame may cause a considerable increase of the residual CO_2.

- The increase of the kiln length leads to the decrease of the residual CO_2, but it also causes the increases of the kiln temperature and the pressure drop

110

The simulation results can be directly used for the purpose of designing and regulating the shaft kilns. As an example, the following describes several possibilities for regulating kiln processes.

a) If the desire is to reduce the residual CO_2, it can be done in different ways:

- Increase the energy consumption
- Decrease the kiln throughput
- Extend the height of solid bed (increase the solid residence time)

b) If the desire is to increase the kiln throughput while the residual CO_2 must be fixed, the two following possibilities can be done:

- Increase the energy consumption
- Extend the height of solid bed

c) If the desire is to lower the kiln temperatures, especially the lime temperature, it can be implemented by:

- Decreasing the energy consumption
- Increasing the excess air number
- Increasing the kiln throughput or decreasing the solid bed height

The simulation results were validated by the experiments with measuring temperatures in industrial kilns. The results of experiments and those of simulations are in good agreement. In addition, the simulation results demonstrate that the maximum temperatures of solid particles in the PFR kilns are significantly lower than that in the normal shaft kilns. In the PFR kilns, they vary in the range of $1000 - 1100\ ^oC$ while in the normal shaft kilns they are in the range of $1400 - 1500\ ^oC$. Therefore, for producing soft-burnt lime, the PFR kilns are suitable whereas the normal shaft kilns are suitable for the production of hard-burnt lime.

Outlooks

- Observations from experiments have shown that the condition at one cross-section along the kiln axis is inhomogeneous while it is assumed in the mathematical models (1D) of the present work as homogeneous. Further work should focus on this issue by developing 2D or 3D simulations.

- The mathematical models deal with only the spheres of the same size. Future works should be extended to particle size distribution and actual particle shapes.

- The fuel combustion is treated in a simple way with a given burning profile. It should be described as a function, which depends on the oxygen concentration, the excess air number, the types of fuel etc.

- With the PFR kilns, the mathematical models deal with the mean values of the periodic fluctuations. The actual periodic behaviors should be considered in future work.

Appendix

The BVP Solver

The function bvp4c solves two-point boundary value problems for ordinary differential equations (ODEs). It integrates a system of first-order ordinary differential equations,

$$y' = f(x, y)$$

on the interval [a b] subject to general two-point boundary conditions,

$$bc(y(a), y(b)) = 0$$

It can also accommodate other types of boundary value problems, such as those that have any of the following:

• Unknown parameters

• Singularities in the solutions

• Multipoint conditions.

In this case, the number of boundary conditions must be sufficient to determine the solution and the unknown parameters.

bvp4c produces a solution that is continuous on [a b] and has a continuous first derivative there. bvp4c is a finite difference code that implements the 3-stage Lobatto IIIa formula. This is a collocation formula and the collocation polynomial provides a C^1-continuous solution that is fourth-order accurate uniformly in the interval of integration. Mesh selection and error control are based on the residual of the continuous solution. The collocation technique uses a mesh of points to divide the interval of integration into subintervals. The solver determines a numerical solution by solving a global system of algebraic equations resulting from the boundary conditions, and the collocation conditions imposed on all the subintervals. The solver then estimates the error of the numerical solution on each subinterval. If the solution does not satisfy the tolerance criteria, the solver adapts the mesh and repeats the process. The user must provide the points of the initial mesh as well as an initial approximation of the solution at the mesh points.

References

[1]   Oates, J. A. H.. Lime and Limestone, Wiley- VCH, Weinheim, 1998.

[2]   Hills, A.W.D.: The mechanism of the thermal decomposition of calcium carbonate, Chemical Engineering Science, Vol. 23, pp. 297–320, 1968.

[3]   Hisieh, C. L.: Evaluating the energy performance of a lime kiln, Tappi Journal, Vol. 66, pp. 77- 79, 1983.

[4]   Zuideveld, P. L., Berg, P. J.: Design of lime shaft kiln, Chemical Engineering Science Vol. 26, pp. 875-883, 1970.

[5]   Schwertmann, T.: Thermodynamic aspects of the counterflow lime burning process (Part 1), Cement Lime Gypsum, Vol. 57, pp. 48-58, 2004.

[6]   Schwertmann, T.: Thermodynamic aspects of the counterflow lime burning process (Part 2), Cement Lime Gypsum Vol. 57, pp. 64-67, 2004.

[7]   Piringer, H.: Fuel gases with low calorific value for firing PFR lime shaft kilns, Cement Lime Gypsum, Vol. 56, pp. 66 - 72, 2003.

[8]   Lucian, P.: Lime production - The vertical process, Pit and Quarry Journal, Vol. 81, pp. 34 – 38, 1998.

[9]   Lang, G., Bao, C., Gao, S., Logan, R.L., Li, Y.: Study on the energy-saving technology of Chinese shaft calciners, The Minerals, Metals & Materials Society, Wiley- VCH 2011.

[10] Sagapov, V. Sh., Burkin, M. V.: Theoretical modeling of simultaneous processes of coke burning and limestone decomposition in a furnace, Combustion Explosion Shock, Vol.44, No.1, pp. 55-63, 2008.

[11] YI-Zheng-ming, ZHOU Jie-min, CHEN Hong-rong.: Numerical simulation of thermal process and energy saving of lime furnace, Journal of Central South University of Technology, Vol. 12, pp. 295-299, 2005.

[12] Senegacnik, A., Oman, J., Brane, S.: Analysis calcination parameter and temperature profile in an annular shaft kiln. Part 1: Theoretical survey, Applied Thermal Engineering, Vol. 27, pp. 1467-1472, 2007.

[13] Senegacnik, A., Oman, J., Brane, S.: Analysis calcination parameter and temperature profile in an annular shaft kiln. Part 2: Results of test, Applied Thermal Engineering, Vol. 27, pp. 1473-1482, 2007.

[14] Drenhaus, T.B., Simsek, E., Scherer, V.: A couple fluid dynamic-discrete element simulation of heat and mass transfer in a lime shaft kiln, Chemical Engineering Science Vol. 65, pp. 2821-2834, 2010.

[15] Canadian Minerals Yearbook for Lime, 1998.

[16] U.S. Geological Survey, Minerals Yearbook, 1999.

[17] U.S. Geological Survey, Mineral Commodity Summaries, http://minerals.usgs.gov/minerals/pubs/commodity/lime, February 2000.

[18] U.S. Geological Survey, Mineral Commodity Summaries, http://minerals.usgs.gov/minerals/pubs/commodity/lime, February 2009.

[19] U.S. Geological Survey, Mineral Commodity Summaries, http://minerals.usgs.gov/minerals/pubs/commodity/lime, February 2010.

[20] European Commission: Reference Document on Best Available Techniques in the Cement and Lime Manufacturing Industries, March 2010.

[21] Jenkins, B.: What are shaft kilns for lime manufacturers, IFRF online combustion handbook, ISSN 1607-9116, 2003.

[22] Ebertsch, G., Plickert, S.: German contribution to the BREF-Review, Part I: Lime manufacturing industry, 2006.

[23] Characteristics of some types of shaft kilns, http://www.ineris.fr.org/aida, 2007.

[24] Lime market research in Russia and Central Federal District, http://www.infomine.ru, 2007.

[25] Jeschar, R.: Heat transfer in pelletizing with mixed feed, Archiv für das Eisenhüttenwesen, 35, H.6, 1964.

[26] Jeschar, R., Specht, E., Alt, R.: Grundlagen der Wärmeübertragung. Viola-Jeschar-Verlag, Goslar,1990.

[27] Bes, A.: Dynamic Process simulation of limestone calcination in normal shaft kilns, Dissertation, Otto-von-Guericke University Magdeburg, 2006.

[28] Mills, A. F., Anthony, F., Basic heat and mass transfer, Prentice Hall, 1999.

[29] Specht, E.: Kinetik der Abbaureaktionen, Cuvillier Verlag, Göttingen, 1993.

[30] Furnas, C. C.: Flow of gases through beds of broken solids, Bull. 307, U.S. Bureau of Mines, 1929.

[31] Tsotsas, E.: VDI Wärmeatlas, Wärmeleitung und dispersion in durchströmten Schütungen, 9. Auflage, 2002.

[32] Giese, M.: Stromüng in porösen Medien unter Berücksichtigung efficktiver Viskositäten, Dissertation, TU Müchen, 1998.

[33] Ergun, S.: Fluid flow through packed columns, Chemical Engineering Process, Vol.48, pp. 89-94, 1952.

[34] Brauer, M.: Grundlagen der Einphasen- und Mehrphasenströmungen, Sauerländer Verlag, Goslar, 1990.

[35] Cheng, C.: Thermal processes simulation of reactive particles on moving grate, Dissertation, Otto-von-Guericke University Magdeburg, 2007.

[36] Shwertmann, T.: Untersuchung des Optimierungspotentials des Ringschachtofens zum Brennen von carbonatischem Gestein, Dissertation, Otto-von-Guericke University Magdeburg, 2007.

[37] Szekely, J., Evans , J.W, Sohn, H.Y.: Gas-Solid-Reactions, Academic press, New York, 1976.

[38] Kainer, H., Specht, E., Jeschar, R.: Die Porendifussions-, Reactions- und Wärmeleitkoeffizienten verschiedener Kalksteine und ihr Einfluss auf die Zersetzungszeit, Cement Lime Gypsum, Vol. 39, pp. 214-219, 1986.

[39] Silva, M., Specht, E., Schmidt, J.. Thermophysical properties of the limestone as a function of origin (Part 2), Calcination enthalpy and equilibrium temperature, Cement Lime Gypsum 6, pp. 51-57, 2010.

[40] Bes, A., Specht, E., Kehse G.: Influence of the type of fuel on the energy consumption in lime burning, Cement Lime Gypsum, Vol.60, pp. 84-93, 2007.

[41] Chai, L., Navrotsky, A.: Thermochemistry of carbonate-pyroxene equilibrium, Contribution to Mineralogy and Petrology, Vol.114, pp. 139-147, 1993.

[42] Specht, E.: Combustion Technology, handout for Master of Safety, Quality and Environment, Otto-von-Guericke University Magdeburg.

[43] Collarini: Innovative design of high capacity twin shaft regenerative lime kilns, Cement International Journal, Vol.7(3), pp. 38 – 42, 2009.

[44] Piringer, H., Werner, W.: Process optimization on Maerz lime kilns, Cement Lime Gypsum, Vol. 58, pp. 41-58, 2005.

[45] Verma, C. L.: Simulation of lime shaft kilns using mathematical modeling, Cement Lime Gypsum, Vol.12, pp. 576-582, 1990.

[46] Verma, C. L., Dave, N.G., Saraf, S.K.: Performance estimation vis-à-vis design of mixed-feed lime shaft kiln, Cement Lime Gypsum, Vol.9, pp 471-477, 1988.

[47] Unaspekov, B. A., Strekalova, L. V.: A model study of the performance of a Kazogneupor shaft kiln, Journal of Refractories and Industrial Ceramic, Vol. 48, No. 7-8, pp. 275-276, 2002.

[48] Sagapov, V. Sh., Burkin, M. V., A. V. Voromin, A. A. Shatov.: Calculation of limestone burning in coke-fired kiln, Theoretical Fundamental of Chemical Engineering, Vol. 38, No.4, pp. 441-447, 2004.

[49] Marias, F., Bruyeres, B.: Modelling of a biomass fired furnace for production of lime, Chemical Engineering Science, Vol. 64, pp. 3417-3426, 2009.

[50] Sheng-xiang, D., Qing-song, X., Zhie-min, Z.: A lime shaft kiln diagnostic expert system based on holographic monitoring and real-time simulation, Expert system with applications, Vol. 38, pp. 15400-15408, 2011.

[51] Hai Do, D., Specht, E.: Dynamic modeling of lime burning process in normal shaft kiln, Proceeding of Chemical Engineering Conference, CHEMECA2010, Adelaide Australia 2010, pp.3468-3478.

[52] Hai Do, D., Specht, E.: Numerical simulation of heat and mass transfer of limestone decomposition in normal shaft kiln, Proceeding of Thermal Engineering Joint Conference, ASME/JSME 8th USA 2011, pp. T10060 – T10060-10.

[53] Martins, M.A., Oliveira, L.S., Franca, A.S.: Modeling and simulation of limestone calcination in rotary kilns (part 2: industrial rotary kiln), Cement Lime Gypsum, Vol. 55, pp. 74–83, 2002.

[54] Senegacnik, A., Oman, J., Brane, S.: Influence of temperature profile in an annular shaft kiln on calcination, International Journal of Microstructure and Materials Properties, Vol. 1, No. 2, pp. 785-792, 2006.

[55] Manseung, L., Sihyung, L.: A mathematical model of calcination of limestone in rotary kiln, Journal of Steel Research, Vol. 70, pp. 15 - 21, 1999.

[56] Cheng, C., Specht, E.: Reaction coefficient in decomposition of lumpy limestone of different origin, Thermochimica acta, Vol. 449, pp. 8–15, 2006.

[57] Cheng, C., Specht, E., Kehse. G.: Influences of the origin and material properties of limestone on its decomposition behavior in shaft kilns, Cement Lime-Gypsum, Vol.60, pp. 51–61, 2007.

[58] Hai Do, D., Specht, E.: Determination of thermal conductivity, reaction coefficient and pore diffusivity in decomposition of limestone of different origin, Proceeding of the world congress on engineering and computer science, USA 2011, Vol. 2, pp.617-622.

[59] Bes, A., Specht, E., Kehse G.: Calculation of the cooling zone length and lime discharge temperature of lime shaft kilns, Cement Lime Gypsum, Vol. 60, pp. 63-73, 2007.

[60] HaiDo, D., Specht, E., Kehse, G., Ferri, V., Christiansen, T., L., Bresciani, P.: Simulation of lime calcination in PFR kiln – Influence of energy input and kiln throughput, Cement Lime Gypsum, Vol.12, pp.52- 64, 2011.

[61] HaiDo, D., Specht, E., Kehse, G., Ferri, V., Christiansen, T., L., Bresciani, P.: Simulation of lime calcination in PFR kiln – Influence of source and size of limestone, Cement Lime Gypsum, Vol.4, pp.56- 65, 2012.

[62] Commandre, J.M., Salvado, S., Nzihou, A.: Reactivity of laboratory and industrial limes, Chemical Engineering Research and Design, Vol. 85, pp. 473-480, 2007.

[63] Kamperl, J., Maeck, J.: Precipitation of calcium carbonate from hydrated lime of variable reactivity, granulation and optical properties, International Journal of Mineral Process, Vol. 93, pp. 84-88, 2009.

Curriculum Vitae

<u>Personal data</u>

Name:	Duc Hai Do
Date of Birth:	March 15, 1979
Place of Birth:	Vinh Phuc, VietNam
Marital status:	Married
Nationality:	VietNam

<u>Education</u>

1994-1997	High school
	Vinh Yen High School, Vinh Phuc, VietNam
1997-2002	Bachelor of Chemical Engineering
	Major: Petrochemical – Organic Technology
	Hanoi University of Technology, Hanoi, VietNam
2006-2007	Master of Science
	Major: Quality, Safety and Environment (QSE)
	Otto von Guericke University Magdeburg
2007-2012	Ph.D student
	Otto von Guericke University Magdeburg

<u>Work experience</u>

Dec. 2002-Aug.2006	Process engineer, Chief operator
	Dinh Co LPG and Refinery factory, PetroVietnam Gas Co.,
	101 Le Loi Str., Vung Tau, VietNam
Nov. 2007-Jun.2012	Scientific employee
	Otto von Guericke University Magdeburg

<u>Awards</u>

2002	The first prize in "Students' Scientific Research" Award
	Ministry of Education and Training, VietNam
2002	Award for students with excellent graduation
	Hanoi University of Technology, VietNam
2006	Full DAAD scholarship for Master program
	Otto von Guericke University Magdeburg